The Noise of a Boundary Layer Flowing Over Discrete Roughness Elements

Matthew Byron Rasnick

Thesis submitted to the faculty of the Virginia Polytechnic Institute
and State University in partial fulfillment of the requirements for the degree of
Master of Science in Aerospace Engineering

William J. Devenport
Stewart Glegg
Roger L. Simpson

May 23, 2010
Blacksburg, Virginia

Keywords: wall jet, roughness noise, rough wall turbulent boundary layer, unsteady drag spectrum

The Noise of a Boundary Layer Flowing Over Discrete Roughness Elements

Matthew Byron Rasnick

ABSTRACT

This study focuses on measuring and normalizing the roughness noise of multiple roughness types across numerous layouts and flow speeds. Using the Virginia Tech Anechoic Wall Jet Facility, far field noise was recording for the flow of a turbulent wall jet boundary layer over cubes, hemispheres, and gravel, with element heights in the range of 14.3 - 55.2% of the boundary layer thickness. The sound radiated from the various layouts showed that the elements acted as independent sources when separated by three element diameters center-to-center or more. When the elements were placed shoulder to shoulder, interaction between the elements and shielding of the higher velocity flow lowered the noise per element produced. The far field roughness noise was then normalized using the theory of Glegg et al. (2007), which assumes a dipole efficiency factor. Comparisons were made between the theoretical drag spectrum model proposed by Glegg et al. (1987) and a modified version of this model made using the empirical data gathered. Overall, the theory of Glegg et al. (2007) succeeds greatly in collapsing the data into its non-dimensional drag spectra, but the original model spectrum did not fit well. The modified spectrum showed much greater fit with the data at all layouts and speeds. The collapse of the data using the theory of Glegg et al. (2007) confirms that roughness noise is dipole in nature.

Acknowledgements

I would like to first and foremost thank my family for their support throughout my educational career. They have been very encouraging in all of my endeavors and always supportive of all my pursuits. I couldn’t ask for a better set of parents or sister.

Also deserving my thanks are Dr. Stewart Glegg of FAU and Dr. Roger Simpson of Virginia Tech for providing insights into my research and work and for participating on my thesis committee.

Much appreciation is given to Dr. William Devenport, my advisor, committee chair, and mentor, for his guidance and leadership. Throughout both my class and research work, as both an undergraduate and a graduate student, I have matured greatly as both a student and a person under him. He was able to help me make sense of many of the difficulties I faced, and always offered an open door and mind to my thoughts and questions.

I would also like to thank my coworkers and friends. Dr. Aurelien Borgoltz, Erin Crede, Nathan Alexander, Ben Worrall, Ryan Catlett, Jon Forest, Rachel Van Buren, and Julien Fenouil have all helped with both measurements, analysis, and keeping me occupied in my down time.

A special thanks goes to Dr. Ki-Han Kim and ONR grant N0014-08-1-0934 that made this research possible.

Thank you all,

Matthew Rasnick

Contents

1 Introduction 1

- 1.1 Purpose 1
- 1.2 Literature Review 1
- 1.3 Goals 4

2 Apparatus and Instrumentation 6

- 2.1 Virginia Tech Anechoic Wall Jet Tunnel Facility 6
- 2.2 Far Field Microphone Set Up 10
  - 2.2.1 Microphones 10
  - 2.2.2 Microphone Stands 10
  - 2.2.3 Microphone Traverse 11
  - 2.2.4 Scalloping Correction 12
- 2.3 Hot Wire 15
  - 2.3.1 Probe and Bridge 15
  - 2.3.2 Calibration 15
  - 2.3.3 Traverse 17
  - 2.3.4 Measurement 19
- 2.4 Roughness 20
  - 2.4.1 Gravel Arrays 20
  - 2.4.2 Cubic Arrays 25
  - 2.4.3 Hemispheric Array 27

3 Analysis and Discussion 28

- 3.1 Wall Jet Characteristics with Acoustic Enclosure 28
- 3.2 Background Noise Levels 30
- 3.3 Far Field Noise 34
  - 3.3.1 6mm Gravel 34
  - 3.3.2 9mm Gravel 41
  - 3.3.3 3mm Cubes 47
  - 3.3.4 Comparison of Similar Layouts for Different Size Roughness Elements 53
  - 3.3.5 3mm Hemispheres 55
  - 3.3.6 Comparison of Hemispherical and Cubic Roughness Noise 56

3.3.7 Comparison to Alexander (2009) Small Element Roughness 57
3.4 Glegg *et al.* (2007) Normalization 59
3.4.1 Formulation.. 59
3.4.2 6mm Gravel Roughness.. 61
3.4.3 9mm Gravel Roughness.. 61
3.4.4 3mm Cubic Roughness 62
3.4.5 3mm Hemispherical Roughness 66
3.4.6 Unsteady Drag Percentage of Mean Drag 66
3.4.7 Effect of Speed on Collapse... 67
3.4.8 Effect of Shape on Collapse... 68
3.4.9 Modification of Glegg et al. (1987) Model.. 69
4 Conclusion... 75
References.. 77

List of Figures

Figure 2-1 - Virginia Tech Anechoic Wall Jet Tunnel and Facility 6
Figure 2-2 - Nozzle and shelf... 7
Figure 2-3 Plate Coordinate System 8
Figure 2-4 - Sentra Pressure Transducer.. 8
Figure 2-5 - 1/2" B&K model 4190 microphone 10
Figure 2-6 - Original microphone stands 10
Figure 2-7 – Microphone traverse system 11
Figure 2-8 - Microphone traverse system, showing acoustic treatment and microphone stands . 12
Figure 2-9 - Acoustically treated microphone mount 12
Figure 2-10 - Far field acoustic data taken with original, untreated microphone stands............. 13
Figure 2-11 - Plot showing the difference in measured far field acoustic noise from both the original, untreated microphone stand, and the new, treated stand 14
Figure 2-12 - Corrected far field acoustic data using equation 0 14
Figure 2-13 – Auspex AHWU-100 single wire probe 15
Figure 2-14 - Auspex AHWU-100 single wire probe.. 15
Figure 2-15 - Hot Wire Calibrator 16
Figure 2-16 - Calibrator fan 16
Figure 2-17 - Omega DP80 Series Thermocouple.. 17
Figure 2-18 - Hot Wire Traverse 17
Figure 2-19 - Hot Wire Traverse, close up of vertical axis 18
Figure 2-20 - Probe mounting arm... 18
Figure 2-21 - Cathetometer... 19
Figure 2-22 - Top Fin Premium Quality Aquarium Gravel... 20
Figure 2-23 - Plastic screen for sorting gravel.. 21
Figure 2-24 - Mylar backing sheet.. 21
Figure 2-25 – 6 and 9mm gravel elements... 22
Figure 2-26 - Rocks glued to Mylar backing... 22
Figure 2-27 - Rock arrays 23
Figure 2-28 - Example fetch spacing... 23
Figure 2-29 – Full fetch layout, 6mm gravel, scale in centimeters.. 24
Figure 2-30 - Full fetch layout, 9mm gravel, scale in centimeters 24
Figure 2-31 – 3mm Cubic element 25
Figure 2-32 - Cubic array.. 26
Figure 2-33 - Cubic arrays 26
Figure 2-34 - Hemispherical roughness patch 27
Figure 3-1 - Plate Coordinate System... 28
Figure 3-2 - Single hot wire profile showing the normalized mean velocity profiles at various speeds and locations on the smooth plate 28

Figure 3-3 - Single hot wire profile showing the normalized turbulence profiles at various speeds and locations on the smooth plate 29
Figure 3-4 – 0.254mm Mylar Substrate, for use with 6 and 9mm gravel 31
Figure 3-5 – 0.13mm Mylar Substrate, for use with 3mm cubes 32
Figure 3-6 – Kevlar Substrate, for use with 3mm hemispheres 32
Figure 3-7 - Clean plate vs. substrate with increasing speed from 20 to 60 m/s by 10 m/s increments 33
Figure 3-8 (a-e) - Far field sound spectra for the 6mm gravel including facility background noise. See top left figure for legend. 36
Figure 3-9 (a-e) - Far field sound spectra for the 6mm gravel with facility background noise subtracted, leaving only roughness noise. See top left figure for legend. 37
Figure 3-10 (a-f)- Far field sound spectra for the 6mm gravel with facility background noise subtracted, leaving only roughness noise. See top left figure for legend. Note, no data is present in (a), it is shown merely for completeness. 38
Figure 3-11 (a-e)– Far field sound spectra for the 9mm gravel including facility background noise. See top left figure for legend. 42
Figure 3-12 (a-e)- Far field sound spectra for the 9mm gravel with facility background noise subtracted, leaving only roughness noise. See top left figure for legend. 44
Figure 3-13 (a-f)- Far field sound spectra for the 9mm gravel with facility background noise subtracted, leaving only roughness noise. See top left figure for legend. 46
Figure 3-14 (a-e)- Far field sound spectra for the 3mm cubes including facility background noise. See top left figure for legend. 48
Figure 3-15 (a-e)- Far field sound spectra for the 3mm cubes with facility background noise subtracted, leaving only roughness noise. See top left figure for legend. 49
Figure 3-16 (a-h)- Far field sound spectra for the 3mm cubes with facility background noise subtracted, leaving only roughness noise. See top left figure for legend. 53
Figure 3-17 (a-c) – Far field sound spectra for the 3mm cube, 6mm and 9mm gravel 2x3 arrays at 40, 50, and 60m/s, respectively. 54
Figure 3-18 - Far field sound spectra for the 3mm hemisphere 6x7 array including facility background noise. 55
Figure 3-19 - Far field sound spectra for the 3mm hemisphere with facility background noise subtracted, leaving only roughness noise. 56
Figure 3-20 - Far field sound spectra for the 3mm cubic and 3mm Hemispherical 6x7 arrays. .. 57
Figure 3-21 - Far field subtracted comparison of 20, 40, and 80 grit sandpaper fetches vs the 6x7 3mm cubic and hemisphere arrays and the 11x21 6 and 9mm gravel arrays 58
Figure 3-22 - Far field subtracted comparison of 20, 40, and 80 grit sandpaper fetches vs the full fetches of 6 and 9mm gravel 58
Figure 3-23 (a-e) - Normalized drag spectra of 6mm gravel arrays with listed dB adjustments.. 63
Figure 3-24 (a-e) - Normalized drag spectra of 9mm gravel arrays with listed dB adjustments.. 64
Figure 3-25(a-e) - Normalized drag spectra of 3mm cubic arrays with listed dB adjustments 65

Figure 3-26 - Normalized drag spectra of 3mm hemisphere array with listed dB adjustments ... 66
Figure 3-27 (a-d) – Normalized drag spectra of 11x21 element arrays of 6 and 9mm gravel and 6x7 element arrays of 3mm cubes and hemispheres 67
Figure 3-28 - Subtracted spectra of 6x7 element layouts of 3mm cubes and hemispheres along and 11x21 element layouts of 6 and 9mm gravel. 69
Figure 3-29 – Normalized drag spectra of 6x7 element layouts of 3mm cubes and hemispheres along and 11x21 element layouts of 6 and 9mm gravel. 69
Figure 3-30 - Normalized roughness noise of 6x7 element layouts of 3mm cubes and hemispheres along and 11x21 element layouts of 6 and 9mm gravel with modified drag spectrum to best fit data 71
Figure 3-31 (a and b)– Effects of modifying A and n in the Glegg *et al.* (1987) drag spectra model 71
Figure 3-32 (a-d) – Normalized roughness noise for the 3mm cubes, 3mm hemispheres, 6mm and 9mm gravel showing the modified drag spectra 72
Figure 3-33 (a-d) - Normalized drag spectra of 11x21 element arrays of 6 and 9mm gravel and 6x7 element arrays of 3mm cubes and hemispheres showing the modified drag spectrum 73

1 Introduction

1.1 Purpose

Historically, roughness noise has been very difficult to measure due to the low signal to noise ratio, even in ideal settings. When compared to the noise generated by edges or jets, it can be very difficult to make a distinction between the surface noise and background levels. It is even up for debate the mechanisms that produce this noise and whether it is of dipole or quadrupole nature. This paper's goal is to show that noise generated from elements only a fraction of the boundary layer thickness do in fact generate a measureable increase in noise over that of the background flow. Another purpose is to build on previous measurements such as Grissom *et al.* 2007 and Alexander 2009 using the Virginia Tech Anechoic Wall Jet Facility.

1.2 Literature Review

Although roughness noise has been studied since the 1960's, there has yet to be a consensus as to the formation and propagation of the noise generated by roughness elements on an otherwise smooth surface. From Curle (1955) and Lighthill (1952), we see that dipoles and quadrupoles radiate sound as U^6 and U^8, respectively, where U is velocity. Studies applicable to this paper began with Skudrzyk & Haddle (1960). Using a rotating cylinder covered in both large (60 grit) and small (180 grit) element sandpaper in a water tank, they measured radiated sound using hydrophones. The rotating cylinder allowed for a thicker boundary layer to be formed. The paper built on previous studies showing that roughness had no effect on drag until the roughness elements were large enough to pierce the laminar sublayer. Their hydrophones used by Skudrzyk & Haddle were 2.5" and 5" in diameter, and were flush mounted carefully to the wall of the water tunnel. The rotating cylinder was made as smooth as possible so as to not contaminate the background levels. From their measurements, they concluded that as velocity increased, radiated noise levels increased with U^6, $U^{10.3}$, and U^{12} for smooth, 180 grit, and 60 grit cases, respectively.

Continuing to Chanaud (1969), sound levels were measured from a roughened rotating disk in an acoustically treated room. He found that roughness doesn't contribute to low frequencies noise, below ~3500 Hz in his experiment. Shear stress dipoles were hypothesized to be a large contributing factor to sound generation, with the main source of noise production being the roughness elements themselves.

Howe (1979) argues that the viscous shear dipole doesn't serve to generate noise, it merely propagates it. He concludes that at low Mach numbers, viscosity actually serves to diminish rather than enhance boundary layer noise radiation and that surface stress fluctuations can be ignored in estimating the radiation angles away from grazing. His theory states that aerodynamic sources are merely Lighthill quadrupoles distributed over an ideal reflection surface.

In 1980, Cole measured the sound generated by boundary layer turbulence using a smooth surface covered in both 40 and 80 grit blankets. Using a large parabolic microphone system, he measured sound levels from the roughened blankets that were up to 3 dB higher than the smooth plate, and attempted to fit the data with both dipole and quadrupole scaling laws. Cole found that the radiation power spectra for the roughened blankets obey both of the laws, but is closer to being a quadrupole. He suggests that perhaps it is a mixture of the two.

Hersh (1983) used a 4' long circular pipe that was roughened to take measurements of far field sound in a semi-anechoic room. Work was done to eliminate the possibility that the pipe lip dipole or pipe shell excitation was not a factor in generating the sound attributed to the roughness noise. Hersh placed a ½" B&K condenser microphone 50" from the pipe exit on the centerline of the pipe. Hersh's measurements were made from 150-400 ft/sec, and consisted of smooth wall measurements along with 40, 120, 150, and 180 sand grain sizes distributed over the last foot of the pipe. It was shown that the smooth pipe data scales well with the quadrupole U^8 scalings, where the roughened pipe exhibits U^6, or dipole, scaling. Also, by holding the exhaust speed constant at 174 ft/sec and varying the roughness, the intensity of the high frequency sound was shown to increase with grain size.

Howe (1984) used hemispherical elements on a plane wall to model Hersh's experiment, and found that the sound produced by a unit area of the wall varies with U^6, confirming Hersh's data from before. He hypothesized that the Reynolds stresses close to the wall interact with the elements to produce the far field sound. In 1988, he updated his model to include diffractive components of the near fields of the surface roughness elements. He was not able to use Hersh's data fully due to not knowing the roughness factor, but still managed to find agreement when comparing the shape of the data.

Liu, Dowling, and Shin (2006) compared various empirical models for the wall pressure wavenumber spectrum and applied them to the prediction of those due to far field roughness noise for an airframe. Models used were Corcos, Efimtsov, Smol'yakov and Tkachenko, Ffowcs Williams, and Chase. All models used the wavenumber-frequency spectrum $P_s(\kappa,\omega)$ in terms of friction velocity u_τ, boundary layer thickness δ, and eddy convection velocity U_c. The experiment placed a 0.64m x 0.64m region of hemispherical beads at the exit of a 0-31.0m/s open jet wind tunnel. Using four ½" condenser microphones arranged in a 0.16m x 0.16m square, measurements were taken 0.6m from the surface. They showed an increase in noise from 1-2.5kHz that can be attributed to the rough fetch, showing a 10dB increase at some points. The data was also less scattered than the smooth background noise, showing a statistically steady sound source. Comparison with the models shows some agreement, but the peak in the experimental data was at lower frequencies and decays quicker than the theory. It was concluded that larger roughness height and increasing density play a key role in the increase in the overall sound pressure levels generated by the roughness fetch.

Further investigation in Liu *et al.* (2007) used roughened plates in the same set up with a larger array of microphones. Measurements confirmed the dipole nature of roughness noise, and further confirmed previous measurements. The streamwise gradients of the source strengths were underestimated by up to 3dB, showing that although the new measurements were reassuring, work for an improved theoretical prediction is still left to be done.

Glegg *et al.* (2007) analyzed two mechanisms for sound generation by a boundary layer. He concludes that Howe's (1984) concept of hydrodynamic pressure fluctuations within the boundary layer interacting with the roughness elements to become scattered as acoustic waves was correct. His new theory states that acoustic waves are scattered as a dipole aligned with the surface due to the roughness elements acting as a drag element producing different scaling laws. He shows that Howe was correct when he formulated that scattering noise dominated shear stress dipoles for elements whose height extends into the log region of the boundary layer, but determined that the frequency scaling is determined not by the roughness height, but by the correlation lengthscale of the roughness elements.

Anderson *et al.* (2007) measured sound radiation in an open jet tunnel from 32" x 16" rough surfaces made of different sized gravels at various spacings. Using a 63 element far field phased array, the integration of the beamforming maps should increased roughness noise with roughness height and element density, much the same as Liu, Dowling, and Shin (2006). Scalings based on speed showed that at the forward part of the fetches, where the boundary layer transitions from smooth to rough surfaces, the sound pressure levels scale on U^6 or U^7. Downstream, where the surface is completely rough, the total sound pressure scales as $\sim U^8$. This implies that the sound radiated changes from dipole-like at the front of the fetch to quadrupole downstream.

Taking all of the history of roughness noise measurements into account, the Virginia Tech Anechoic Wall Jet Facility was designed and built solely for the purpose of measuring roughness noise. Built in 2005, the facility has been used for multiple measurements, including the ones presented in this paper. In 2007, Grissom took measurements of multiple roughnesses with roughness heights ranging from 0.068mm to 0.118mm. His speed range was 7-22m/s at the beginning of the rough surface. His results were then scaled using Cole (1980), Howe (1988), Farabee and Geib (1991), and Glegg *et al.* (2007) with limited success. He showed the source likely radiates most effectively in the streamwise direction. When comparing scaling based on dipole or quadrupole scaling laws, it was seen that the dipole scaling were effective at high frequencies for either set of variables where the quadrupole scalings were effective only for the outer variables.

In 2008, Yang and Wang did a flow field simulation using LES of a single and pair of hemispherical roughness elements in a turbulent boundary layer. They based their simulations on the Curle-Powell integral solution to Lighthill's equation, and validated it against experiments. They found that the sound radiation was dominated by unsteady drag dipoles and their image in the wall, with the spanwise dipole being controlling over the streamwise. They also found that the pressure contribution to the drag dipole is far stronger than the viscous effects, and that having an upstream wake will significantly enhance sound radiation in the streamwise direction at higher frequencies.

Alexander (2009) measured stochastic rough surfaces of varying grit sand paper, along with 1mm and 3mm hemispherical surfaces and a 2D near-sinusoidal rib surface in the Virginia Tech Anechoic Wall Jet Facility. Along with taking measurements, efforts were made to progress the development of the facility, lower background noise of the measurements, and to design and build components to allow for more repeatable measurements. Along with examining the relationship between near and far field pressure fluctuations, he applied the theories of Cole (1980), Howe (1988), Farabee & Geib (1991), Glegg *et al.* (2007), and also the new theory of Glegg & Devenport's (2009) for far field noise generated by stochastic and deterministic surfaces. He found that none of the scaling could effectively collapse the entire frequency range with the varying edge velocity and roughness size. He found that the roughness noise source is very likely dipole in nature due to the ω^2 scaling in all the normalizations made with the Glegg & Devenport (2009) normalization on the surface pressure wavenumber spectrum and the roughness geometry.

Limited preliminary work dealing with data found in this paper was previous published in *Boundary Layer Noise from Discrete Roughness Elements*, Alexander, Rasnick, Catlett, and Devenport (2009). In this, an overview of the theoretical description of sound from discrete elements was formulated from Glegg *et al.* (2007). The following is a continuation of this effort, using larger roughness elements arranged in both a rectilinear grid and stochastic sheets, along with a theoretical description that explains more deeply the processes used in the above formulation.

While previous work of Alexander (2009) shows that the far field noise created by flow over a small scale rough surface, such as sandpaper, is related to the surface pressure spectrum, which can be thought of as homogeneous, the flow over large scale elements is qualitatively different. The pressure field of the large scale roughness is not uniform, and can show large variations around individual elements. Alexander (2009) describes his results using the theory of Glegg and Devenport (2009). The large element roughness, described by the theory of Glegg (2007), has yet to be clearly defined by experiment. Revealing the form of this sound, and showing the fundamental differences to that of the small scale roughness noise, and applying Glegg (2007)'s theory is the fundamental justification for the following work.

1.3 Goals

This project has been a continuation to Alexander (2009). Measurements of the far-field roughness noise of deterministic roughnesses including 6 and 9mm gravel, 3mm cubic elements and 6mm diameter hemispheres, and stochastic surfaces of the 6 and 9mm gravel were taken. In addition to measurements taken, a focus on facility and instrument development was an ongoing process resulting in lower noise contamination and improved data. The objectives of this paper are:

- To reveal the form and levels of the sound radiated from discrete roughness elements when the elements are a significant fraction of the boundary layer thickness.
- To expose the differences in spectral shape of roughness noise from these large scale elements and that of the homogeneous wall pressure spectra sandpaper roughnesses.
- To reveal the interaction, or lack thereof, between adjacent elements and the influence these interactions have on the sound
- To determine the unsteady drag on roughness elements by measured far field roughness noise

- Compare the relation of element size and spacing to far field roughness noise

2 Apparatus and Instrumentation

2.1 Virginia Tech Anechoic Wall Jet Tunnel Facility

The Virginia Tech Anechoic Wall Jet Tunnel Facility was used in all data being presented. It has been used and improved by Grissom (2007), Smith (2008), and Alexander (2009). Shown below is a physical layout of the facility and anechoic chamber.

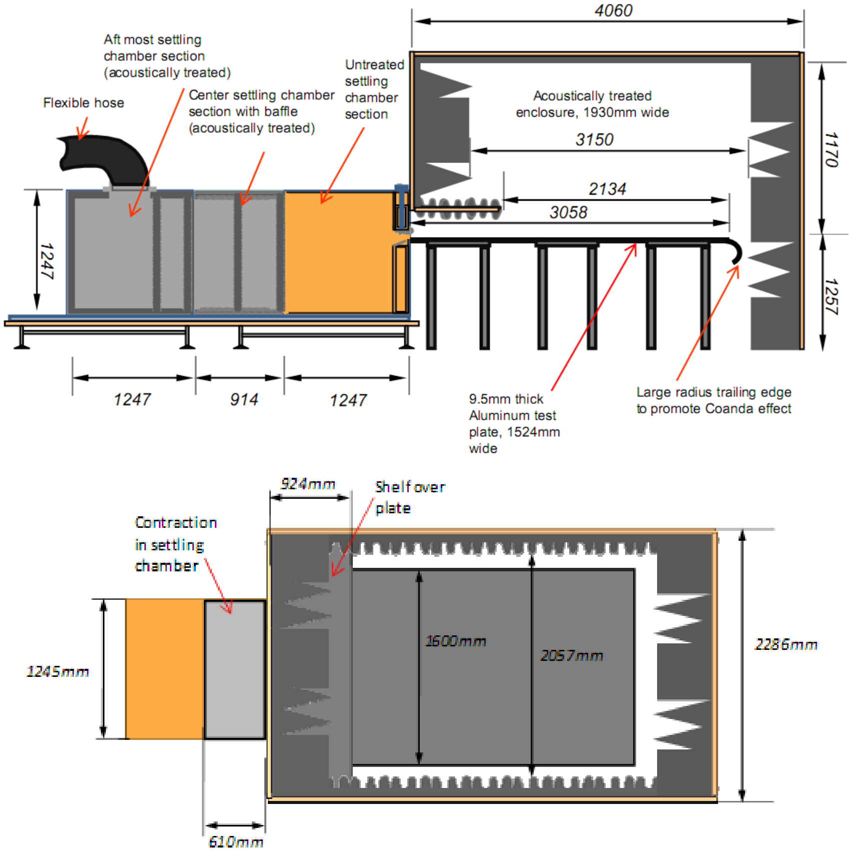

Figure 2-1 - Virginia Tech Anechoic Wall Jet Tunnel and Facility

Not shown is the centrifugal blower attached by the flexible rubber hose shown in the top diagram. A Cincinnati Fan model HP-8D20 variable speed centrifugal fan blows through a flexible rubber hose into the settling chamber. The settling chamber has multiple baffles which have been acoustically treated to prevent fan noise from entering the acoustic enclosure and contaminating measurements.

From the settling chamber, air enters the acoustic chamber through a height adjustable nozzle, shown below. Two hand screws allow the top nozzle's height to be adjusted, allowing for a change in jet height and maximum speeds attainable. For all measurements, the nozzle height was set at 12.4mm, as measured with gauge blocks placed in the corners of the nozzle, and remained in this position to lessen the uncertainty between measurements. The top nozzle is made with two pieces of PVC, milled and joined in the middle with a thin layer of clay to seal any gap. While the centerline of the nozzle is slightly lower at this joint, by 1.2mm, the velocity uncertainty downstream was only 2% of the maximum local velocity.

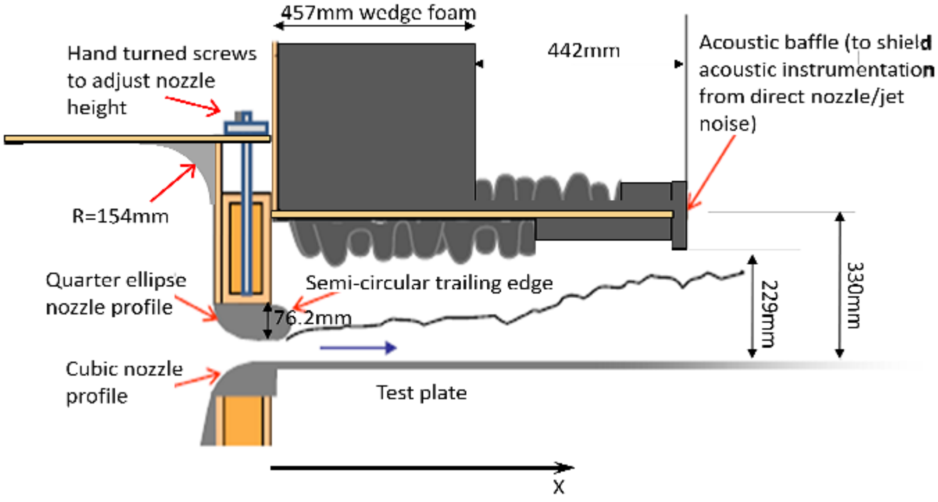

Figure 2-2 - Nozzle and shelf

The fixed lower nozzle and contraction were designed in a single smooth curve using Fang *et al.*'s (2001) formula as shown in Equation 1. h_1 is the contraction height, h_2 is the height from a reference plane, X_m is the distance to the matched point, x is the distance from the exit, and L is the length of the contraction. For this nozzle, h_1 = 681mm, h_2 = 0mm, X_m = 254mm, and L = 610mm.

$$y = (h_1 - h_2)\left[1 - \left(\frac{1}{X_m^2}\right)\left(\frac{x}{L}\right)^3\right] + h_2$$

Equation 1 – Lower nozzle equation

The upper part of nozzle is made of two 90^0 turns, tangential to the ceiling of the settling chamber and the outer 76.2mm semi-circular nozzle. A nozzle based on Fang's formula could not be constructed due to the need for an adjustable nozzle height.

The nozzle produces a flow across the 1600mm wide, 3058mm long aluminum plate. As the nozzle is only 1206mm wide, the plate is amply large to cause no effects of flow over the sides, see Grissom (2007) and Alexander (2009). Also, the end of the plate has a semi-circular half cylinder attached with a radius of 210mm which acts to promote a Coanda effect, minimizing edge noise from the back of the plate. The center of the plate at the nozzle exit acts as the origin for all positioning measurements, as shown below in Figure 2-3.

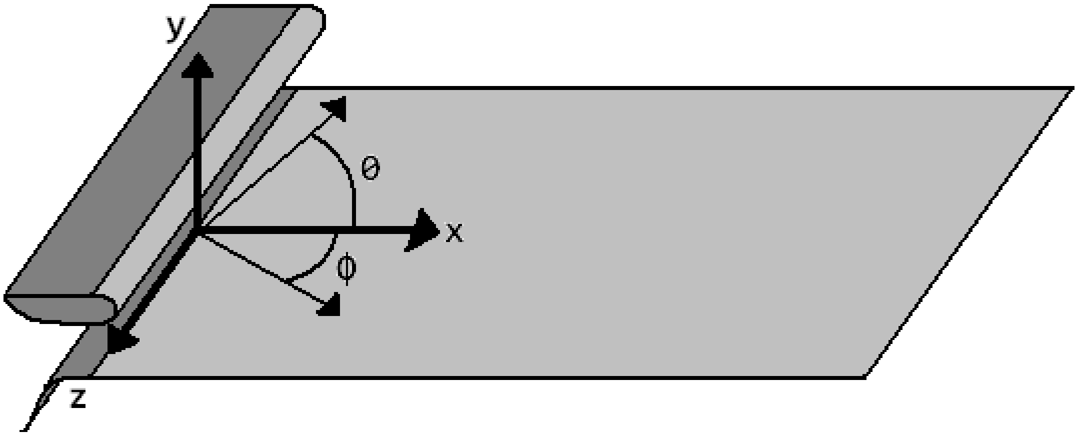

Figure 2-3 Plate Coordinate System

The settling chambers static pressure is measured by a Sentra Model 239 pressure transducer. The difference between this and the ambient pressure in the lab is used to measure flow speed at the nozzle exit.

Figure 2-4 - Sentra Pressure Transducer

Flow temperature is measured with a thermocouple placed where the flow exits the nozzle. The speed is controlled via a VS Utilities program that controls the fan speed. The fan speed/tunnel speed is recorded as a comparison to previous measurements.

The acoustic chamber itself is 1930x4060x2427mm, with added internal baffling. It is made of 25.4mm thick MDF covered with 89mm thick egg crate foam, along with 457mm wedges on the nozzle and exit wall. The chamber is on wheels, so positioning is made repeatable with marks on the floor. The bottom of the chamber has a gap of 152mm, making it open to the lab atmosphere.

Built into the chamber is a shelf that extends 924mm from the nozzle and covers the full width of the chamber. This shelf is treated acoustically with 89mm egg crate foam, and effectively hides the jet noise from microphones positioned above the plate. The bottom of the shelf is 229mm above the plate, well outside of the wall jet flow even at low speeds. The result is that microphones placed above this shelf do not measure sound due to the mixing layer or jet, only the radiated noise from the plate and roughness are measured.

The flow characteristics without the acoustic enclosure are well defined by Grissom *et al.* (2007) and Smith (2008), and shown to be self similar 1850mm from the nozzle in the center 800mm of the plate. Much of the work done by Smith (2008) shows that the flow behaves in a standard wall jet manner, and the mean-velocity profiles can be scaled on the mean velocity, U_e, and the height above peak velocity where the mean velocity is half of the maximum value, $y_{1/2}$. Using the scaling of Narasimha *et al.* (1973) and Wygnanski *et al.* (1992) for U_e and $y_{1/2}$ (the height of the mixing layer half height where $U = ½U_m$), Alexander (2009) has shown the following using

$$\frac{U_e}{U_o} = 4.97 Re_j^{n+1} Re_{x-x_0}^{n}$$

$$y_{\frac{1}{2}} = 0.0259 Re_j^{m-2} Re_{x-x_0}^{m}$$

Equations 2 and 3 – Narasimha and Wygnanski scalings

where n is -0.512 for Equation 2, and m is 0.914 in Equation 3. U_e is the maximum boundary layer velocity, U_o is the nozzle exit velocity, Re_j is the Reynolds number of the jet from the nozzle ($U_o b/\nu$), and Re_{x-xo} is the Reynolds number based on a location, ($U_o(x-x_o)/\nu$), with the origin at zero and x is measure from the nozzle exit.

Knowing $y_{1/2}$, the boundary layer thickness, δ, the displacement thickness, δ*, and the momentum thickness, θ, found as follows using Equations 4, 5, and 6 as taken from Alexander's (2009) fit.

$$\delta^* = 0.0746\delta$$
$$\theta = 0.0549\delta$$
$$y_{\frac{1}{2}} = 7.11\delta$$

Equations 4, 5, and 6 – Boundary layer parameters

The above relationships were established from measurements made with the acoustic enclosure in place. In the present work, another set of hot wire boundary layer measurements was made with the enclosure in place. The resulting profiles, which showed differences from that of the previous measurements, were analyzed by Alexander and Devenport (Private Communication), and are shown in the Results section of this thesis.

2.2 Far Field Microphone Set Up

2.2.1 *Microphones*

Far-field measurements were taken using B&K model 4190 ½-inch free-field microphones, shown below in Figure 2-5.

Figure 2-5 - 1/2" B&K model 4190 microphone

These microphones have a flat response up to 20kHz, and were calibrated with a B&K model 4228 pistonphone. A B&K Nexus 2690 model amplifier was used, and the signals were filtered between 250Hz and 20kHz. The data was taken with an Agilent E1432 16-bit digitizer, taking 1000 records of 2048 samples at a sampling rate of 51200Hz.

2.2.2 *Microphone Stands*

Originally, microphones were placed in a large metal stand, shown below, that was much larger than the microphones themselves. The stand was placed on the shelf of the acoustic chamber, and pointed toward the center of the roughness patch. As the stands were not firmly attached to the shelf and the microphone holders were difficult to position, it proved to be complicated to make minute adjustments in position and aiming. This difficulty resulted in a loss of repeatability of the microphone placement and measurements.

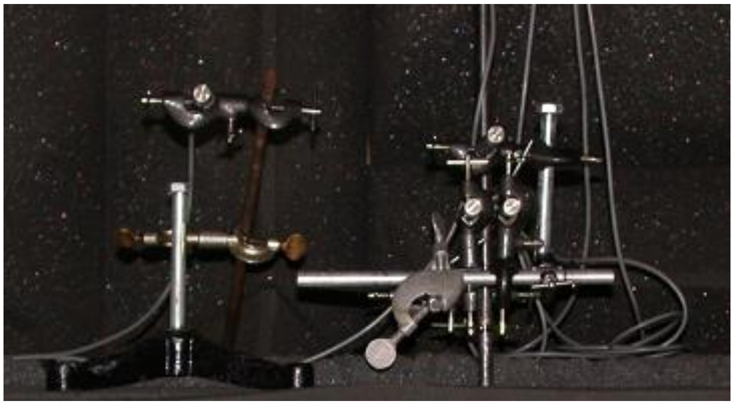

Figure 2-6 - Original microphone stands

A problem associated with the original microphone stand was that spectra measured using it tended to be scalloped. Sound waves, after traveling past the microphone face, could be reflected by the large stand and picked up again by the microphone, producing a constructive/destructive interference wave pattern. Steps were taken to minimize this effect, with the solution being to build a more acoustically transparent microphone mount. This effect, along with its correction, is discussed below in Section 2.2.4.

2.2.3 *Microphone Traverse*

A versatile traverse was designed and built that could better position microphones and not reflect sound waves back to the microphone face. Shown in Figures 2-7 and Figure 2-8 the traverse is mounted to side rails under the flow plate, allowing for positioning in the x direction. The design also allowed for the y position to be altered by raising and lowering the top cross beams. The z position could be altered by sliding the microphone stand from side to side. The stand allowed for further freedom of movement, as the microphone angle to the plate could be altered. A second traverse was made that attached solidly to the shelf. This stand allows for movement in the y and z directions, along with the microphone stand being able to rotate and change pitch angle. The microphone was positioned at a distance 1029mm downstream of the nozzle, 473mm above the spanwise centerline of the plate. The effectiveness of the new traverse will be discussing in Section 3.1.1.

The microphones themselves were mounted to the traverse using acoustically treated microphone stands. They were made using a 6mm threaded rod attached to a low profile 16mm plastic microphone mount and were covered in acoustic foam, as shown in Figure 2-9.

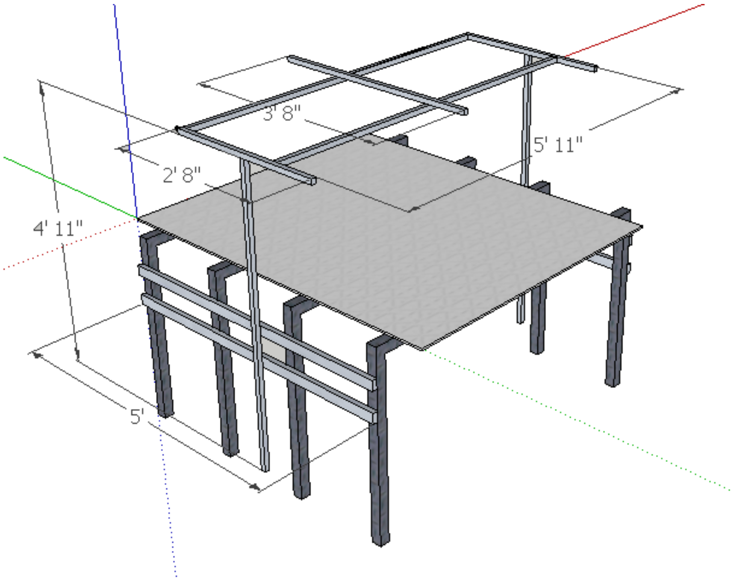

Figure 2-7 – Microphone traverse system

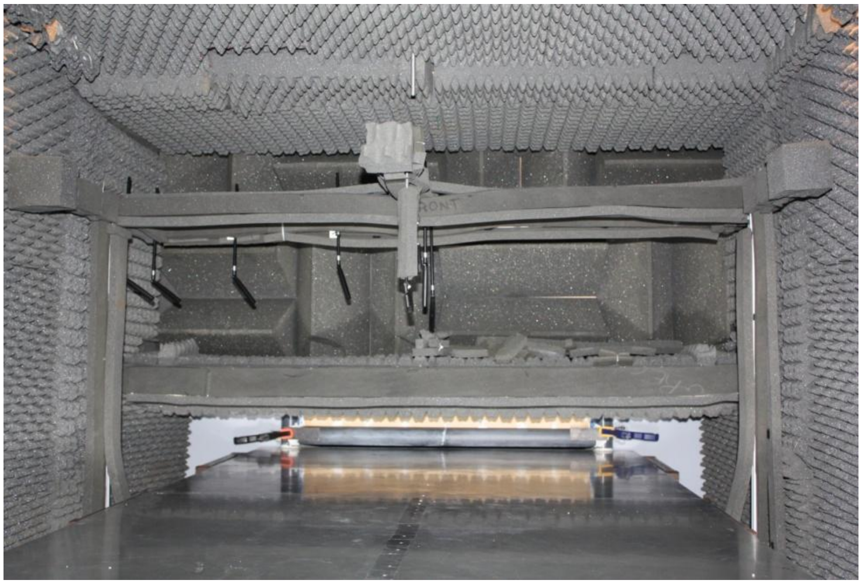

Figure 2-8 - Microphone traverse system, showing acoustic treatment and microphone stands

Figure 2-9 - Acoustically treated microphone mount

2.2.4 *Scalloping Correction*

The above mentioned issue of scalloping due to acoustically untreated microphone stands was corrected by using the new traverse, along with updated microphone mounts treated with acoustic foam as shown in Figure Figure 2-9. Figure 2-10 shows this scalloping. There are large oscillations in the data above 3000 Hz. These oscillations are present, to some degree, in all the data. It is easy to imagine how a reflected wave pattern off of the face of the microphone stands could introduce a constructive/destructive pattern in the data measured by the microphone.

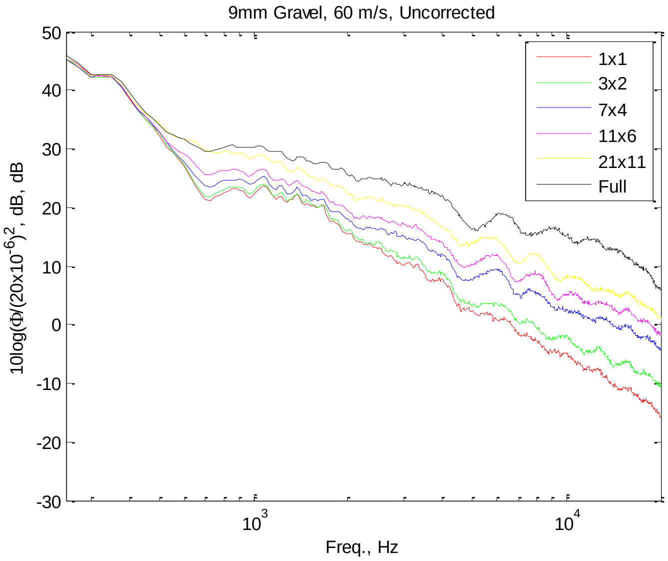

Figure 2-10 - Far field acoustic data taken with original, untreated microphone stands

Shown below, in Figure 2-11, far field acoustic data as taken by the earlier microphone stand are shown in comparison to the new, treated stand. The unscalloped data, not subjected to the same reflecting acoustic waves, exhibits the same trend as the scalloped data, reinforcing that the scalloping was caused by a reflection of sound waves by the microphone stands and not a true effect of the roughness noise. By assuming that the scallops are a function solely of the microphone stand reflections and not of velocity or fetch size, then by using the correlation found with the scalloped and unscalloped measurements at 60 m/s, all of the data can be corrected.

Equation 7 finds the difference in the treated and untreated dB levels of the measured far field roughness noise, and adds it to the measured scalloped data. The outcome of this correction to all the data is shown above in Figure 2-12. The correction works very well for all of the larger roughnesses, with only the 1x1 and 3x2 cases showing scalloping. The correction appears to perform best when a high level of signal to noise is available, and begins to break down as the levels approach the background noise of the tunnel. While only the 60 m/s case is shown here, further results will be analyzed in Section 3 for all other speeds and layouts.

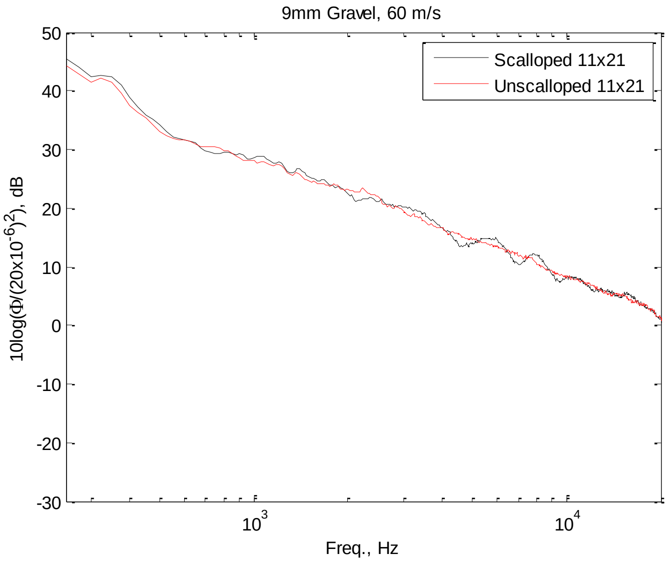

Figure 2-11 - Plot showing the difference in measured far field acoustic noise from both the original, untreated microphone stand, and the new, treated stand

$$SPL_{corrected} = SPL_{scalloped} + 10\log\left(\frac{\phi_{smooth,60\frac{m}{s}}}{(20*10^{-6})^2}\right) - 10\log\left(\frac{\phi_{scalloped,60\frac{m}{s}}}{(20*10^{-6})^2}\right)$$

Equation 7 – Scalloping correction

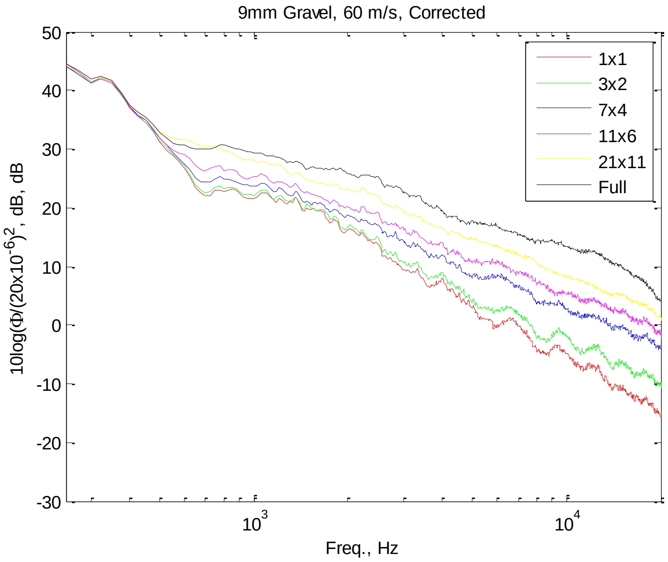

Figure 2-12 - Corrected far field acoustic data using equation 0

2.3 Hot Wire

Hot wire anemometry was used to measure mean and fluctuating flow velocities. By knowing the voltage required to maintain the resistance of a very thin wire under known flow conditions, it is possible to place the wire in unknown flow conditions and, using the relation of voltage required to velocity, interpolate the velocity of the unknown flow. A single wire probe was used to measure the mean velocity and turbulence intensities for vertical profiles above the clean plate at various locations.

2.3.1 *Probe and Bridge*

A straight type single wire Auspex AHWU-100 probe was used with a Tungsten 5μm diameter wire between two prongs separated by 1.2mm, as shown in Figure 2-13 and Figure 2-14.

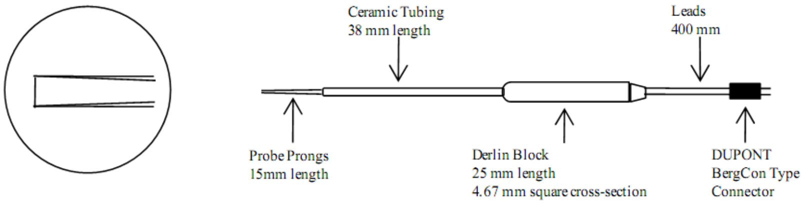

Figure 2-13 – Auspex AHWU-100 single wire probe

Figure 2-14 - Auspex AHWU-100 single wire probe

The probes were balanced and controlled with a Dantec 90C10 Streamline bridge system, capable of measuring mean velocity, turbulence intensity, and spectra. The amplifier has input noise of 1.8nV/√Hz and drift of 0.5μV/^{0}C, with resistor measurement accuracy of 0.1%+/-0.01Ω. The signal conditioner has an input noise of 35nV/√Hz, and a drift of 20μV/^{0}C, which is automatically eliminated by the offset adjust. All of the offsets have <1mV resolution. Probes were balanced to give a frequency response of greater than 20kHz.

2.3.2 *Calibration*

Before taking measurements with the hot wire system, a velocity/voltage calibration file must be taken. The calibration is made by mounting the single hot wire probe into the calibrator; see Figure 2-15 The calibrator is powered by a 5Hp, 13 Amp, Balder R3613T electric motor driving a centrifugal fan, feeding air into the 6" diameter cylindrical settling chamber and out the nozzle, shown in Figure 2-16.

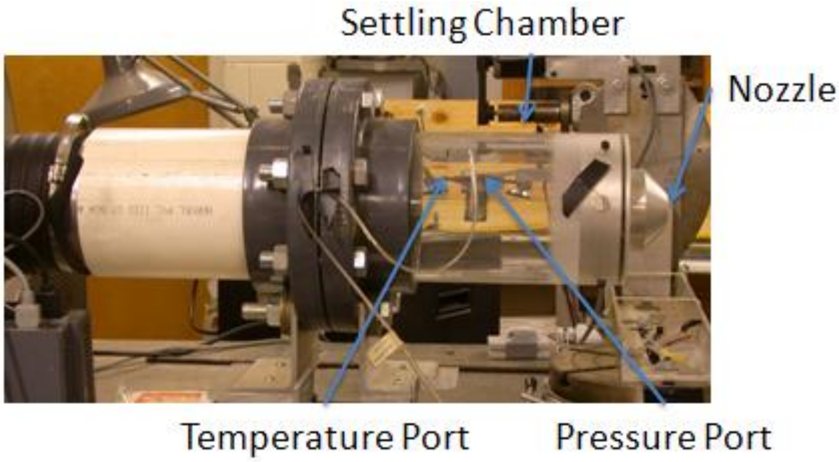

Figure 2-15 - Hot Wire Calibrator

Figure 2-16 - Calibrator fan

The calibrator settling chamber has small holes to measure the static pressure and temperature so that exit velocity from the nozzle is known. With the probe just inside the 1" diameter nozzle exit, the settling chamber pressure, and hence the velocity, can be increased incrementally over the entire speed range that will be encountered in the measurement. Using Agilent VEE programs written in-house that applies King's law, see Equation 8, a calibration file is made for the wire to be used when taking measurements.

$$E^2 = A + BU_{eff}^{0.45}$$

Equation 8 – King's law

In King's law, E is the voltage across the wire, U_{eff} is the flow velocity, A and B are constants that depend on the wire and bridge, and the exponent of 0.45 is assumed common for hot-wire probes. Using an Omega DP80 Series thermocouple, the calibration temperature was measured for each point. While taking measurements, the temperature was also recorded and held to within 5^0 F by running the climate control system in the lab. Temperature corrections were made using the method of Bearman (1971).

Figure 2-17 - Omega DP80 Series Thermocouple

2.3.3 *Traverse*

After calibration, the probe was placed in a traverse designed and built at Virginia Tech, see Figure Figure 2-18. The traverse is mounted with clamps to the aluminum plate at various x positions. Only the vertical y axis is controllable, so the x and z positions are set with the clamps attached the traverse to the plate. The traverse uses a Computmotor S57-83-MO motor, and is controlled with a PDX-13 indexer through the same Agilent VEE program used to take data. The screw has an antibacklash nut to prevent hysteresis from moving in either direction.

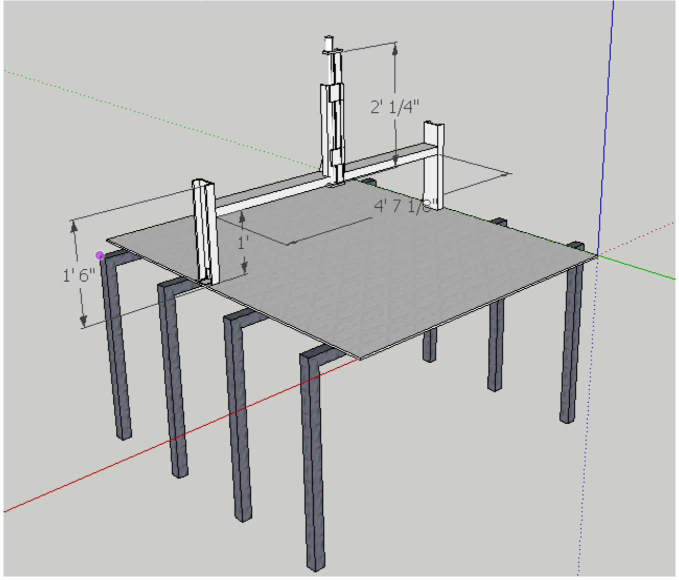

Figure 2-18 - Hot Wire Traverse

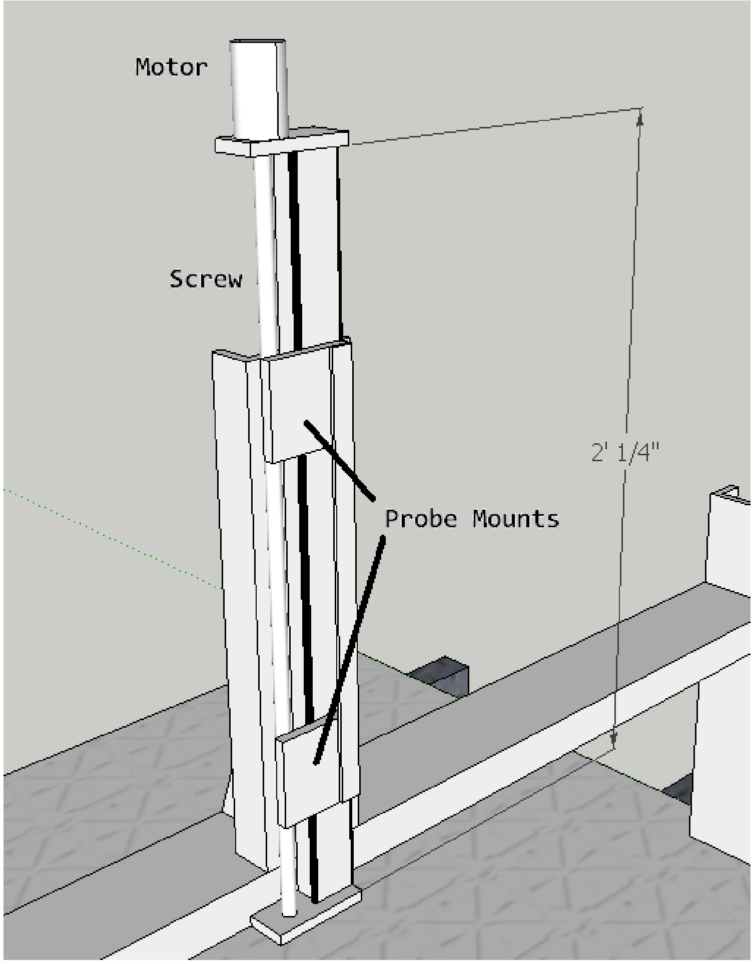

Figure 2-19 - Hot Wire Traverse, close up of vertical axis

The probe is attached to a mounting arm, see Figure 2-20, that is fixed to the traverse y axis with set screws. The arm allows movement in the x and theta direction, and is also locked in place with set screws. The freedom of movement in x and theta allow the probe to be far upstream of the influence of the traverse and mounting arm.

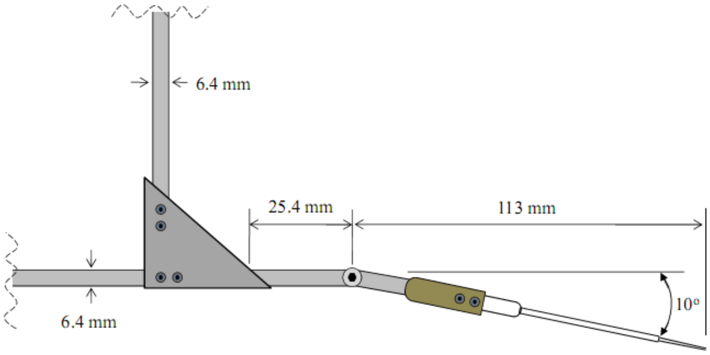

Figure 2-20 - Probe mounting arm

2.3.4 *Measurement*

The Agilent VEE data acquisition program automatically corrects for temperature variations in the flow according to Bearman (1971). The traverse height is set using a cathetometer, shown below. Since the plate is surrounded by the acoustic chamber, the cathetometer was set behind the plate and a gauge block of known height was set next to the probe. The probe was positioned to be even with the top of the block.

Figure 2-21 - Cathetometer

The traverse, starting from the top and working into the boundary layer to delay any possible probe breaks to the end of the run, starts at y = 254mm, and takes forty-six steps down to 0.135mm from the plate to be well within the boundary layer. The steps at the top height are large, as high resolution is not needed. As the probe gets closer to the maximum velocity height and boundary layer, the steps proceed logarithmically, with the last inch accounting for over half of the measure points. A final point is measured as a check point, where the probe is taken back to a point already taken to check the probe is still reading the same velocity. At 80% of the points, 20 records are taken of 1024 points at a sampling rate of 800Hz. Every fifth point's sampling scheme was altered so higher resolution spectra data could be calculated, with 50 records of 2048 points at a sampling rate of 51200Hz.

Data was taken for the clean plate, and also behind roughness fetches, forming a cross sectional profile of aerodynamic data immediately behind the surface. The clean plate profiles were then analyzed by Alexander and Devenport (Private Communication), as shown in Alexander, Rasnick, Catlett, and Devenport (2010), and showed a y location uncertainty of 0.7mm.

2.4 Roughness

Various materials were used to make both stochastic and deterministic element roughness patches of differing sizes. 6mm and 9mm gravel were arranged in increasing grid spacings and with a stochastic full coverage fetch, along with 3mm cube and hemispheres used to make multiple grid arrays as shown below.

2.4.1 *Gravel Arrays*

Two types of gravel were selected for the study, smooth smaller gravel, and large rougher gravel. Both gravels were Top Fin brand Premium Aquarium gravel. As the size in the bags varied from small (~2mm diameter) to large (~12mm), a sieve system was used to get a consistent gravel size to be measured.

Figure 2-22 - Top Fin Premium Quality Aquarium Gravel

Using plastic screens, one of which is shown below, it was possible to isolate gravels by size. One screen had holes that were 4mm per side, another was 8mm. This allowed for sorting of gravel which was approximately 6mm diameter of the smooth stone, and 9mm large stones. A sample of 20 gravel pieces was taken from each full array and measured. The average dimension is listed above, with a standard deviation on both of 1.2mm.

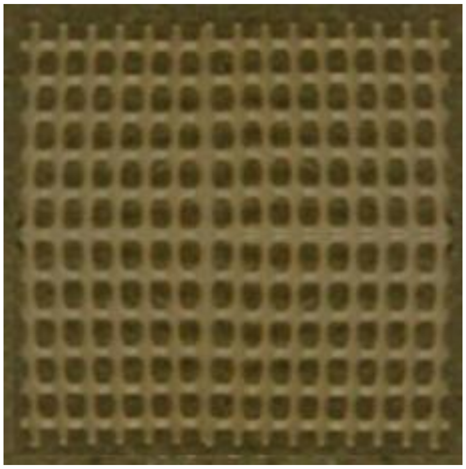

Figure 2-23 - Plastic screen for sorting gravel

Fetches were built from a single gravel element up to an 11x21 fetch measuring 30.5x61.0cm and also a full fetch of full coverage. Arrays were made by gluing the rocks onto a sheet of Mylar backing, shown in Figure 2-24.

Figure 2-24 - Mylar backing sheet

The 6 and 9mm gravel elements are shown below in Figure 2-25. Besides the obvious size difference, another differentiation between the 6 and 9mm elements are shape. The 6mm elements are both more rounded and much smoother than the 9mm elements.

Figure 2-25 – 6 and 9mm gravel elements

The rocks were attached with a small dot of hot glue, shown in Figure 2-26, not visible to the flow. The Mylar sheet was attached to the plate with 0.1mm thick double sided tape and all the edges were secured with 0.1mm thick foil tape. Measurements were taken with nothing on the plate, then with the clean sheet of Mylar with no detectable noise increase. Those results are shown in chapter 3. The center to center spacing of the roughness elements is 28mm in all cases.

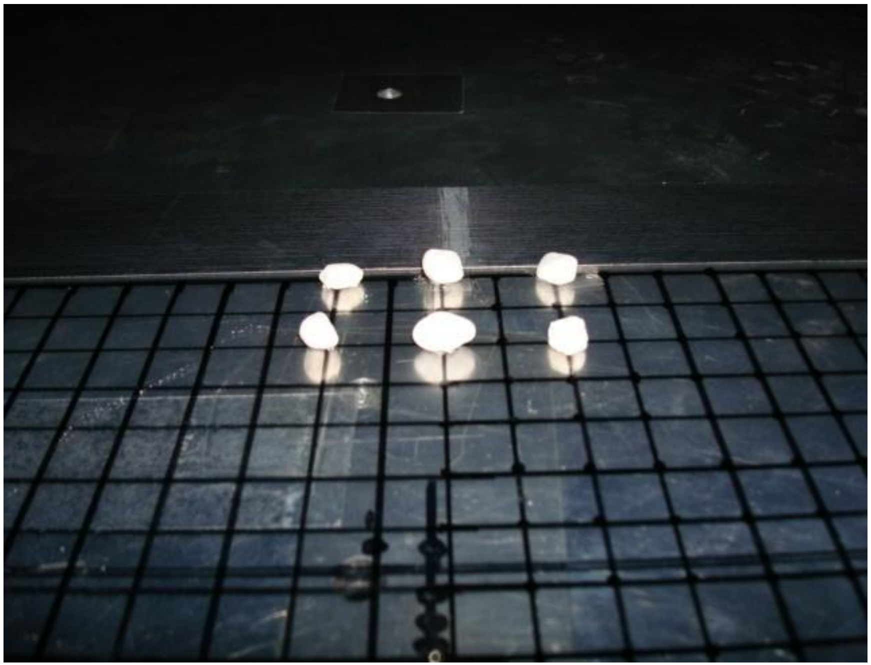

Figure 2-26 - Rocks glued to Mylar backing

Shown in Figure 2-27 is a buildup of the rock fetches, showing the 9mm gravel. Also pictured is the full coverage, made by attached double sided tape to the entire Mylar backing and packing the gravel in as closely as possible. The front middle rock is place 1257mm downstream of the nozzle exit, in the centerline of the plate. Also pictured is a dimensioned photo of the 4x7 array in Figure 2-28, where the spacing is representative of the rest of the fetches, along with a close ups of the full fetch layouts to show coverage in Figure 2-29 and Figure 2-30.

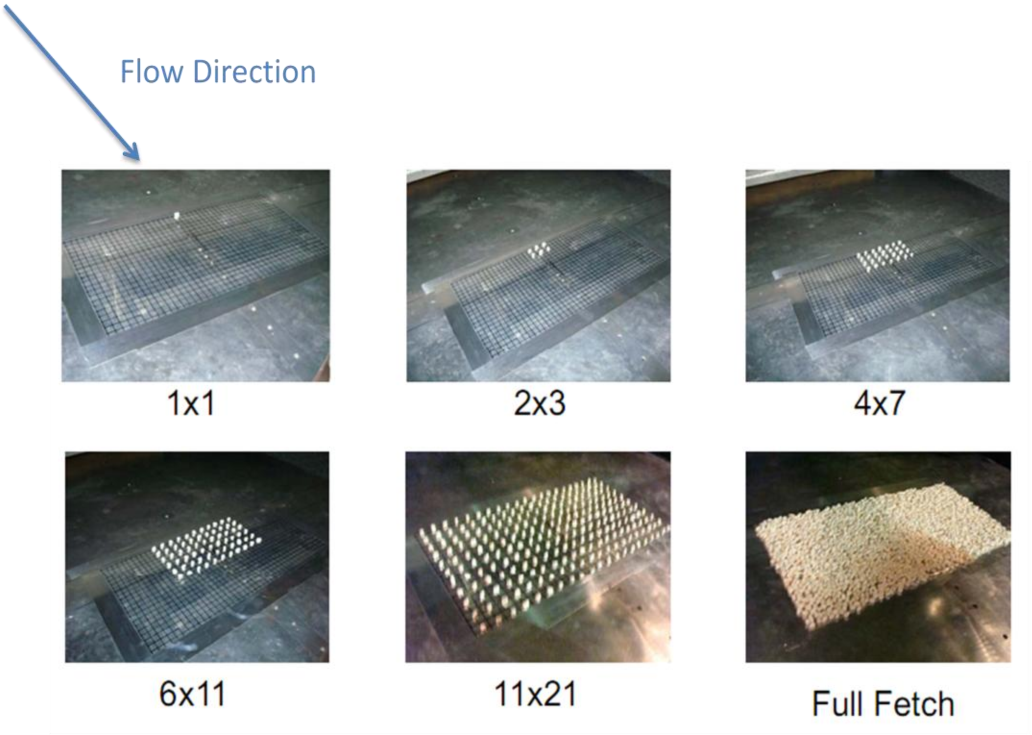

Figure 2-27 - Rock arrays

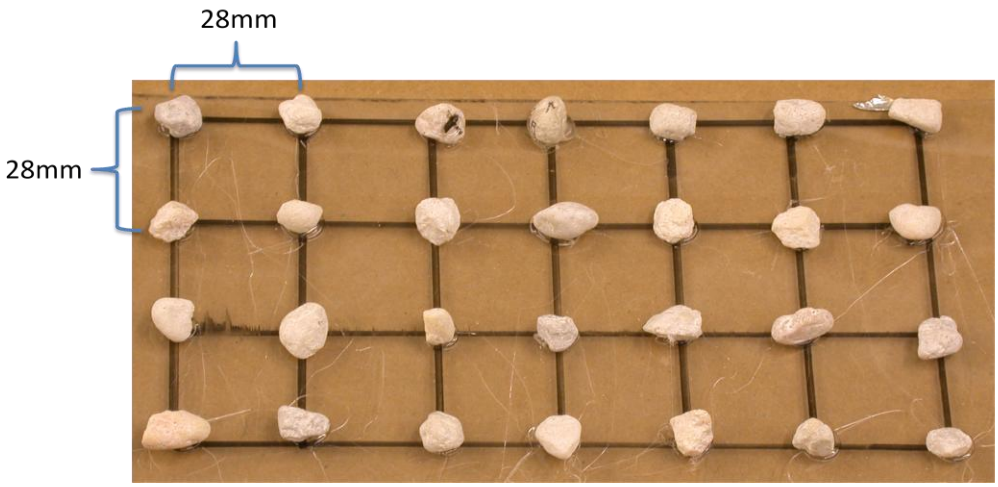

Figure 2-28 - Example fetch spacing

Figure 2-29 – Full fetch layout, 6mm gravel, scale in centimeters

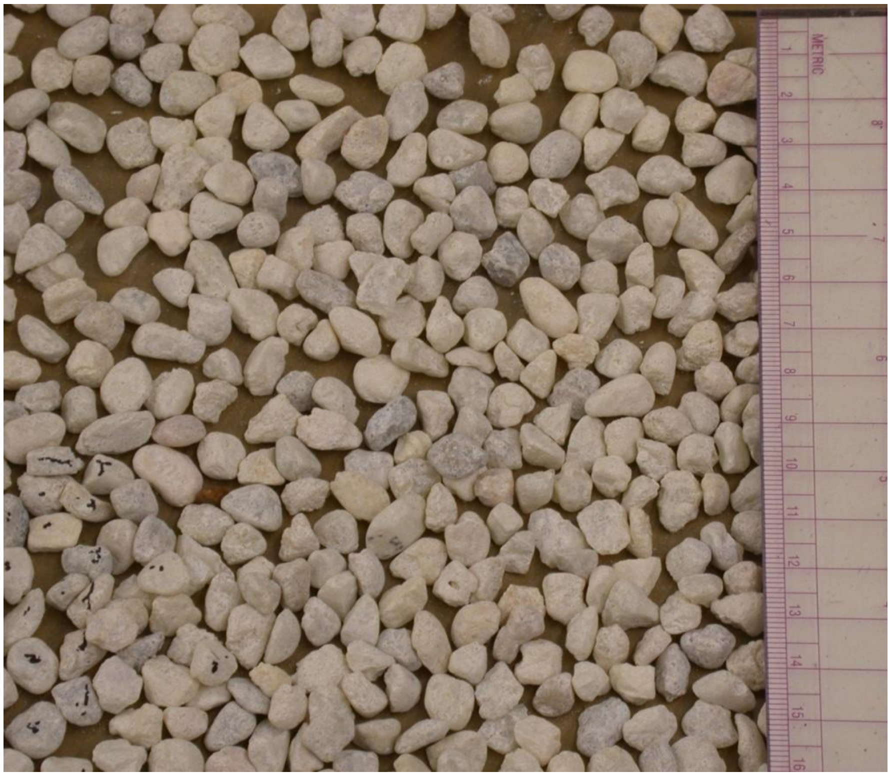

Figure 2-30 - Full fetch layout, 9mm gravel, scale in centimeters

The full fetch made of 6mm gravels averaged 3.2 elements/cm^2 and the fetch of 9mm gravels averaged 1.2 elements/cm^2.

2.4.2 *Cubic Arrays*

In much the same way the rock fetches were built, 8 arrays were made of 3mm cubic elements. The cubes were made from beads, and had a hollow center that was filled with plaster to prevent flow going through the cubes. When attached to the Mylar backing, the covered hole was aligned perpendicular to the flow.

Figure 2-31 – 3mm Cubic element

The elements were attached to the Mylar backing using a small strip of double sided tape and a jig to help with spacing and alignment. Figure 2-32 is a diagram of the 6x7 array of the 3mm cubic elements. Even with the jig, consistent spacing was difficult. The spacing measurements shown below are accurate to within ±0.5mm, and the element faces were accurate to within 5^0 of being perpendicular to the flow. Shown in Figure 2-33, the fetch build up can be seen. The front row of cubes was 1257mm downstream of the nozzle, and the centerline of the fetch was aligned on the centerline of the plate.

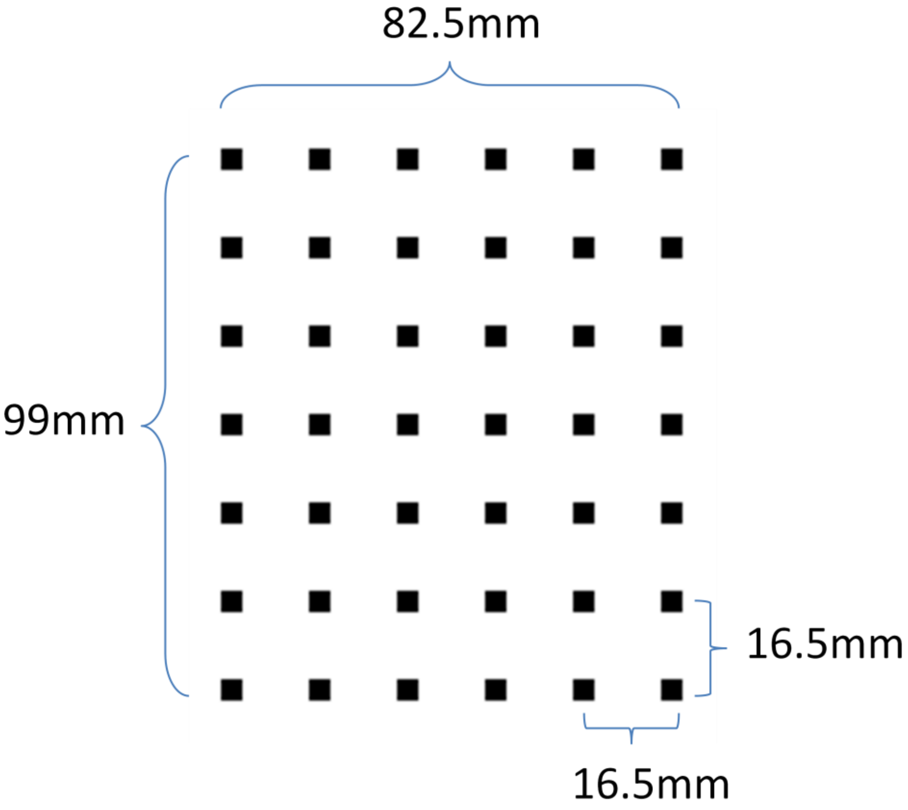

Figure 2-32 - Cubic array

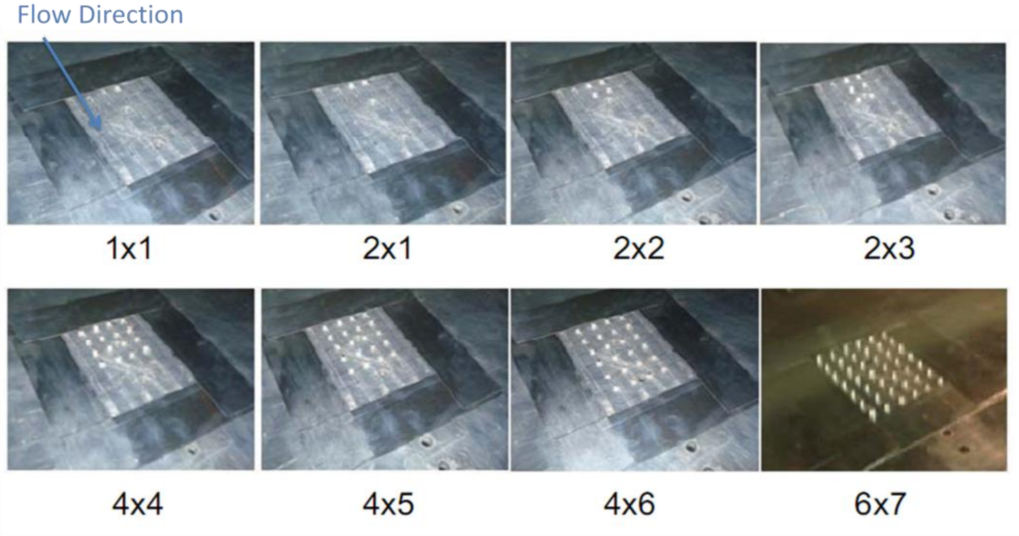

Figure 2-33 - Cubic arrays

2.4.3 *Hemispheric Array*

An array of 3mm radius hemispheres was made with a HDPE mold and epoxy on a Kevlar backing. Data was taken with the same microphone set up as with the cubic elements, with the array front row 1257mm downstream of the nozzle. Shown below is the 6x7 layout.

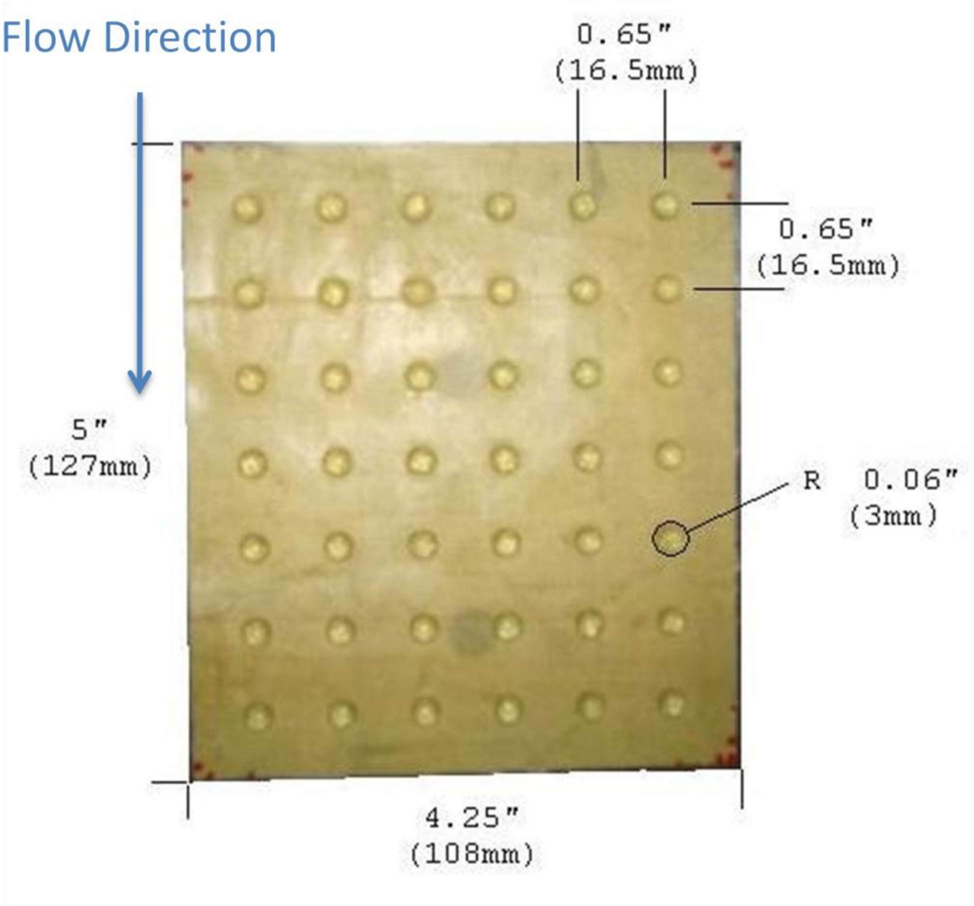

Figure 2-34 - Hemispherical roughness patch

3 Analysis and Discussion

Measurements were made in the Virginia Tech Open Jet Anechoic facility using ½” B&K model 4190 free-field microphone. Data was taken with the nozzle height set at 12.7mm with exit velocities of 20 m/s to 60 m/s. Smooth plate, Mylar sheet, rock, cube, and hemisphere roughnesses were all measured, with the roughnesses starting at 1257mm downstream from the nozzle exit. The microphone placements are described in detail shortly. The coordinate system is the same as defined in Chapter 2, and is shown below for reference.

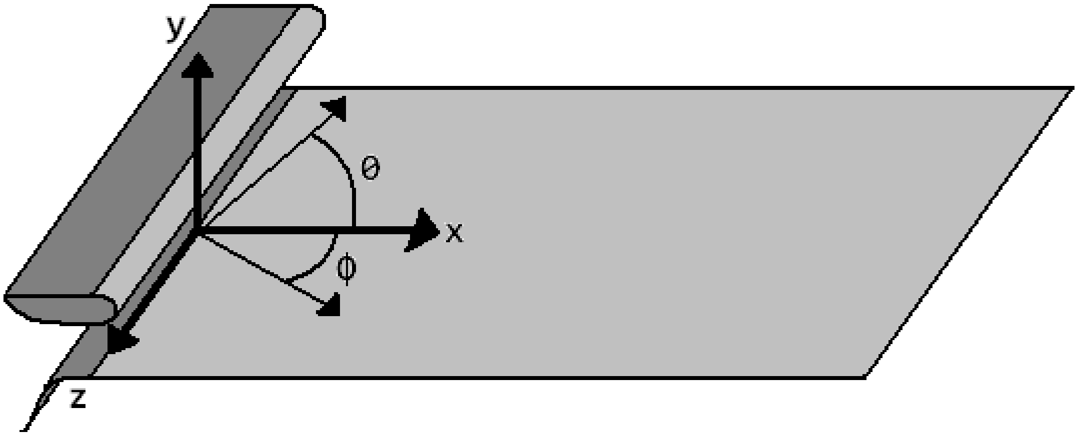

Figure 3-1 - Plate Coordinate System

3.1 Wall Jet Characteristics with Acoustic Enclosure

Single wire hot wire profiles were measured along the centerline of the plate without roughness at 775, 1257, and 1562 from the nozzle exit in the x direction. Figure 3-2 and Figure 3-3 show the normalized mean velocity profiles and turbulence profiles at the aforementioned distance from the nozzle for speeds of 20, 30, 45, and 60m/s.

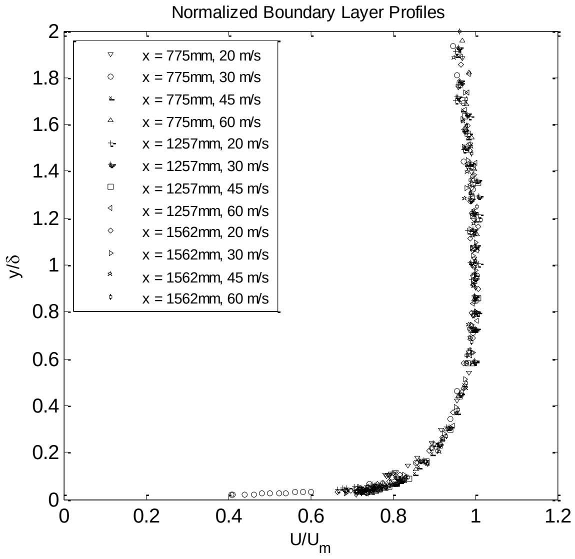

Figure 3-2 - Single hot wire profile showing the normalized mean velocity profiles at various speeds and locations on the smooth plate

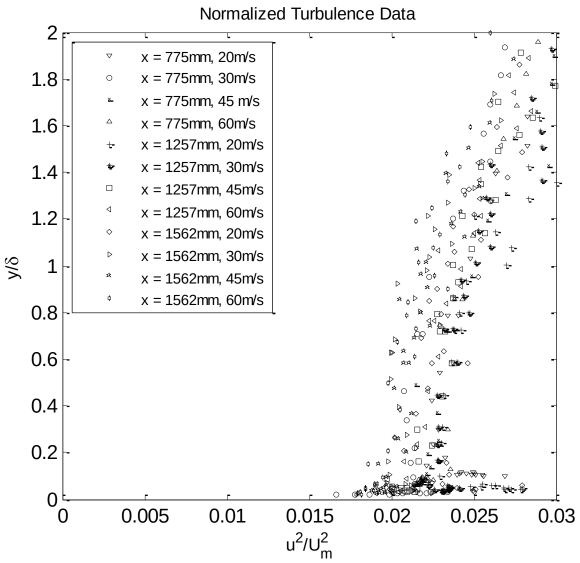

Figure 3-3 - Single hot wire profile showing the normalized turbulence profiles at various speeds and locations on the smooth plate

Each profile at the positions shown in the figures were taken at 20, 30, 45, and 60 m/s. Figure 3-2 shows that the mean velocity profiles are very self similar across all speeds and locations. Figure 3-3, the normalized turbulence profiles, also exhibit a self similarity across all profiles. These results were analyzed by Devenport and Alexander (Private Communication) using the same method as Grissom *et al.* (2007) and Smith (2008). $y_{½}$ was shown to not scale on the boundary layer thickness with the chamber in place, so a new function is introduced. Using the scaling of Narasimha *et al.* (1973) and Wygnanski *et al.* (1992), shown in Equations 9, 11, and 12, the parameters are as follows

$$\frac{U_m}{U_j} = 4.97 Re_j^{n+1} Re_x^n$$

$$\frac{\delta^*}{b} = 0.0156 Re_j^{m-2} Re_x^m$$

$$\frac{y_{\frac{1}{2}}}{b} = 0.0335 Re_j^{p-2} Re_x^p$$

Equations 9, 10, and 11 - Boundary layer parameters with chamber installed

$$\frac{\delta}{\delta^*} = 15.4491$$

$$\frac{\theta}{\delta^*} = 0.74047$$

Equations 12 and 13- Calculated values for chamber installed configuration

where m is 1.0451 and n is -0.512. p is 0.888. Equations 12 and 13 show the updated boundary layer thicknesses based on δ^*.

The focus on the comparison between the flow with and without the enclosure will be on the x=1257mm location. From these measurements, the analysis shows that the edge velocity at the front of the fetch will stay the same with or without the enclosure in place. As mentioned in Section 2.4, the largest element size is 9mm in height. It is shown that with the flow found at the beginning of the roughness, the element will be completely enveloped within the boundary layer.

	Nozzle Speed (m/s)	δ (mm)	δ* (mm)	θ (mm)	Speed at Front of Fetch (m/s)	y1/2 (mm)
Enclosure Off	20	16.7	1.2	0.9	7.5	119.0
	30	15.6	1.2	0.9	11.2	110.9
	40	14.9	1.1	0.8	14.8	105.6
	50	14.3	1.1	0.8	18.4	101.6
	60	13.9	1.0	0.8	21.9	98.5
Enclosure On	20	20.9	1.4	1.0	7.5	129.9
	30	19.1	1.2	0.9	11.2	131.3
	40	17.9	1.2	0.9	14.8	132.4
	50	17.0	1.1	0.8	18.4	133.2
	60	16.3	1.1	0.8	21.9	133.9

Table 3-1 - Flow properties at the front edge of the fetch

While the edge velocity at the front of the fetch was found to be consistent with the enclosure on or off, the flow characteristics do change. The boundary layer grows by 20-25% with the enclosure in place, but shows the same trend in both cases. The $y_{1/2}$ height shows differing trends between the two cases. With the enclosure off, the height decreases substantially with speed, but when the enclosure is on, the height increases slightly with speed. The shelf at the nozzle end of the plate used to block direct jet noise radiation to the microphones is proposed to have a noticeable effect of the upper edge of the flow and the entrainment of stagnant air by the flow around the nozzle. This could be an explanation as to the increase of the $y_{1/2}$ height, however, only the boundary layer and flow localized to these heights are of importance.

3.2 Background Noise Levels

In order to attach the roughness elements, a set of substrates were chosen to be attached to the plate which would then have the elements attached to them. This allowed for quicker transition between measurements and kept the polished aluminum plate as clean as possible. Table 3-2 below shows the three types, their size, and position relative to the coordinate system shown in Figure 3-1

		Dimensions (mm)			Front Middle Location (mm)		
Substrate	Roughness Type	Thickness	Streamwise	Spanwise	x	y	z
Mylar	6 and 9mm Gravel	0.254	305	610	1257	0	0
Mylar	3mm Cubes	0.13	127	108	1257	0	0
Kevlar	3mm Hemispheres	0.19	127	108	1257	0	0

Table 3-2 - Substrate size and positioning

These substrates are shown in Section 2.4, along with dimensioned photographs. Flapping edges or lifting of the substrate would result in a faulty measurement, so care was taken to firmly attach the materials to the plate of the wall jet. Both the 0.13 and 0.254mm thick Mylar substrates were attached with double sided tape under the material, and then all edges were held with 0.1mm thick foil tape to prevent the edges from rising. The Kevlar backing, made by applying a 2 part epoxy to a sheet of Kevlar in a mold, was attached with double sided tape and Scotch brand tape around the edges as the foil tape would not adhere. The following three figures, Figure 3-4 through Figure 3-6, show flow direction and mounting in the wall jet tunnel of all substrates in their measurement positions. Care was taken when applying the tape to the edges to ensure no entrapped air formed bubbles that could affect the smooth surface.

Figure 3-4 – 0.254mm Mylar Substrate, for use with 6 and 9mm gravel

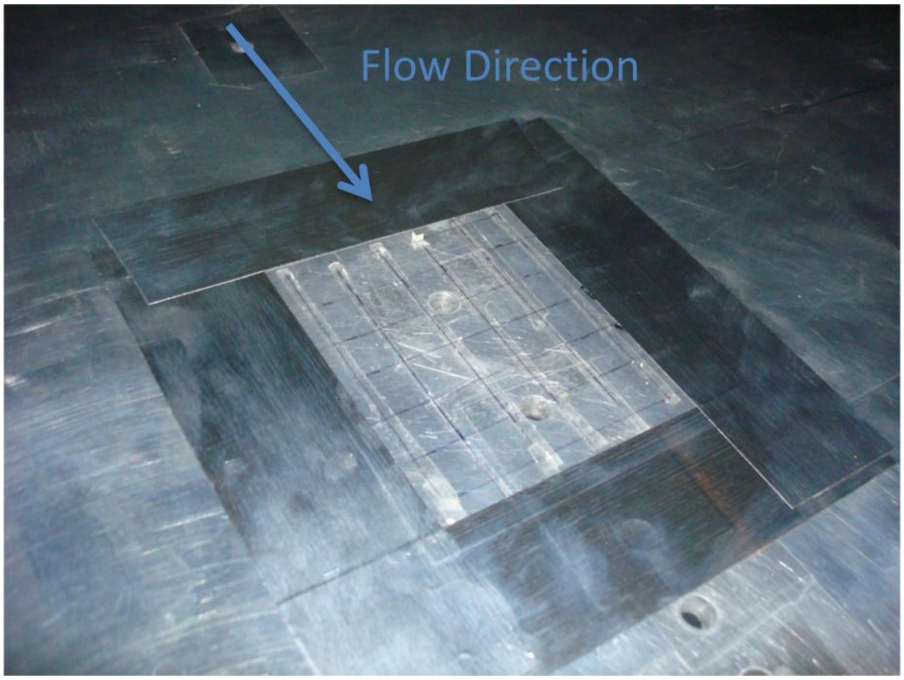

Figure 3-5 – 0.13mm Mylar Substrate, for use with 3mm cubes

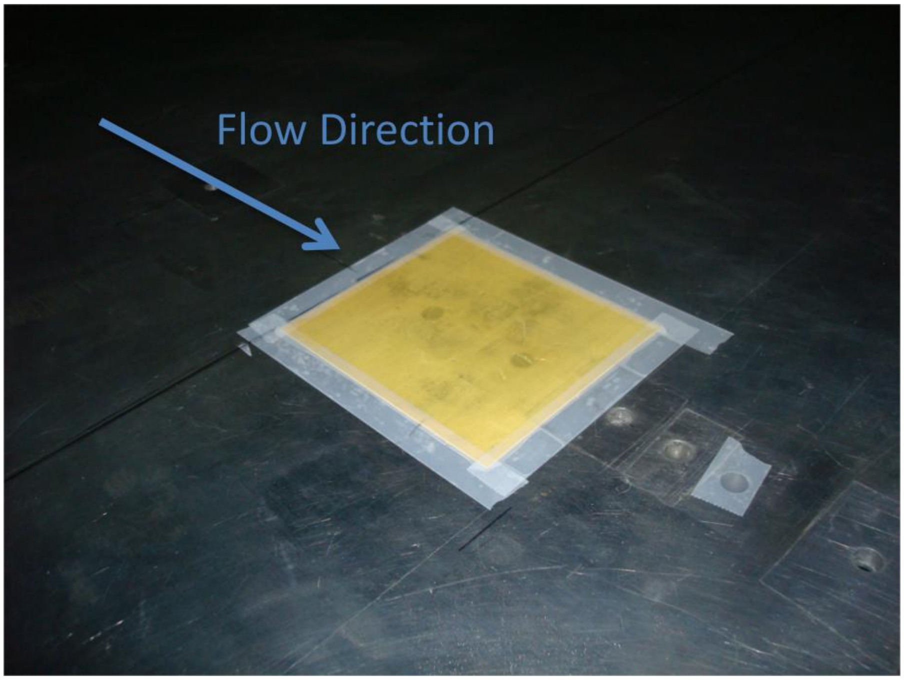

Figure 3-6 – Kevlar Substrate, for use with 3mm hemispheres

In order to check the consistency of background levels in the tunnel, measurements of flow noise from 20 to 60 m/s in increments of 10 m/s was made with the substrates present. No roughness elements were added at this point. This measurement was compared to previous clean plate data as taken by Alexander (2009). The microphones were positioned and aimed as shown below in Table 3-3. See the following Figure 3-7 for the results of the clean plate and substrate sound level measurements.

			Position (mm)			Focal Point (mm)		
Microphone	Measurement	Substrate	x	y	z	x	y	z
A	Alexander (2009)	None	1029	473	0	1403	0	0
B	Gravel (Untreated)	0.254mm Mylar	1016	533	-25	1348	0	0
C	Gravel (Treated)	0.254mm Mylar	1029	473	0	1403	0	0
D	Cubes	0.13mm Mylar	1029	460	0	1321	0	0
E	Hemispheres	0.19mm Kevlar	1029	460	0	1321	0	0

Table 3-3 - Microphone position and focal points for all measurements

Microphone A was used by Alexander in his measurements of both clean plate and sandpaper roughness in 2009. Microphone B was used to measure the first set of gravel roughness, which was shown to produce scalloped data. The acoustically treated microphone mounted on the traverse for the gravel is given as Microphone C. Both Microphones D and E were in the same position, and were acoustically treated and mounted on the traverse for the cubic and hemisphere roughness patches.

For direct comparison of data, the differences in microphone position proved negligible for the frequencies of concern, as will be shown in Figure 3-7. For the normalizations that will be described in Section 3.4, both the distance to the fetches and the angle of the microphone face to the plate will be accounted for.

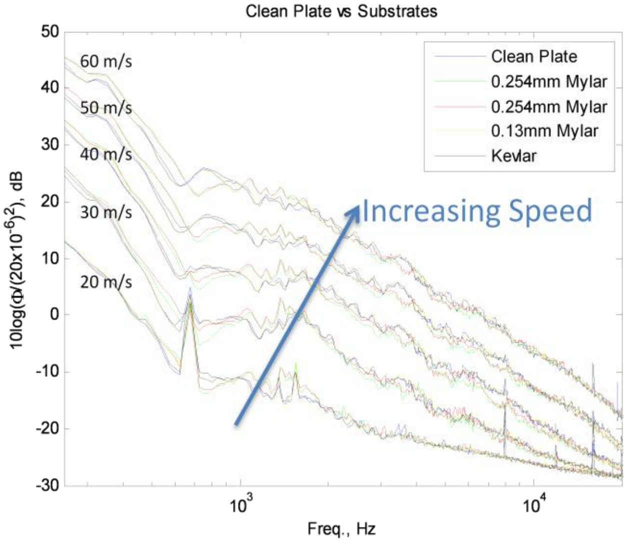

Figure 3-7 - Clean plate vs. substrate with increasing speed from 20 to 60 m/s by 10 m/s increments

Figure 3-7 shows that all the measurements, which were taken with difference microphones and spread over 6 months, exhibit the same general shape. They are plotted in terms of 1 Hz bandwidth SPL relative to $20\text{x}10^{-6}$ Pa. It can be seen that the $1/f$ electrical noise floor of the microphone is reached in the 20 m/s measurement at 2000 Hz, and at ~10000 Hz for the 30 m/s flow. Spikes are present at 8000 Hz and 10500 Hz, which are due to electrical noise. There are some variations in the measured sound levels, especially with the 0.254mm Mylar, at low frequencies. Both of the 0.254mm Mylar measurements were taken with Microphone B, which was affected by the scalloping, resulting in differences of ~1dB in the low frequencies. However, the 0.13mm Mylar and Kevlar are both indistinguishable from the background levels.

By knowing the background sound levels in the tunnel, it is possible to differentiate the noise produced by the roughness over that of the tunnel operating. The noise level of the substrates with roughness, with the substrate only noise subtracted out, is a direct result of the added roughness. To find these levels, Equation 14 is used.

$$SPL_{subtracted} = 10\log\left(\frac{\phi_{rough} - \phi_{clean}}{(20 * 10^{-6})^2}\right)$$

Equation 14 – Subtraction of clean plate from roughness measurement

Data will be presented showing the raw, unsubtracted data, which has been corrected for the scalloping using the method shown in Section 2.2.4, however, the majority of the analysis concerns the subtracted noise levels, focusing on the noise due to the roughness alone.

3.3 Far Field Noise

The following presents results and analysis for the 6 and 9mm gravel, 3mm cubes, and 3mm hemispheres, focusing on the noise from roughness alone. For the 6 and 9mm gravel, the results will be shown with the correction for scalloping applied as shown in Section 2.2.4.

All of the figures shown are plotted on a semi logarithmic scale, with frequency in Hz on the horizontal axis and SPL normalized on 20x10^{-6} on the vertical axis. The frequency range is 250 to 20 kHz, the same as what was band pass filtered when taking the measurement to reduce low frequency noise contamination and aliasing. Each plot has the same vertical and horizontal axis scale for ease of comparison.

3.3.1 *6mm Gravel*

Six layouts of the 9mm gravel were measured at 20 to 60 m/s in increments of 10 m/s. The layouts are described in Section 2.4.1, and are built up from a single element to an 11x21 element grid, and finally a full coverage of the 305x610mm Mylar sheet. In Figure 3-8, the unsubtracted noise levels measured from each layout are shown as arranged by speed.

On the 20 m/s data plot, the 1/*f* electric noise floor of the microphone is reached at 6000 Hz. At the lowest speeds of 20 and 30 m/s, the data appears to become level at the high frequencies, with all the grid layout data crossing the full fetch at 6000 Hz. This is due to the correction from scalloping, so it is not a real effect. This effect will be negated by subtracting out the clean plate data, which will be described shortly. The correction does very well at reducing the scalloping in the rest of the data, as little to no scallops are seen in the 4x7 to Full fetches at any speed.

The results shown in Figure 3-8 (a-e) show that roughness noise from elements as small as 6mm in a ~20mm boundary layer make noise well above that of the background.

At 20m/s, in Figure 3-8 (a), the full fetch is approximately 10dB higher than that of the clean plate at 1000Hz. With increasing speed, all of the layouts produce increased sound levels. At the top speed of 60m/s nozzle exit velocity, the largest 11x21 array produces 20dB of measureable noise increase, while the full fetch produces 26dB over that of the clean plate.

The focus is now shifted to the roughness noise only shown in Figure 3-9 (a-e), using the subtraction shown in Equation 14. Note that the vertical axis has been modified to better show the data, but the same overall range of 80 dB is used.

In this subtracted data, no detectable noise is produced by this single 6mm gravel at any velocities. The 2x3 element array doesn't show any low frequency noise even at the highest speeds. A small hump can be seen between 10000 and 20000 Hz on the full fetch layout, which only increases with speed. This hump shows that there may be an interaction between the closely packed gravel, many of which are touching, that is not present in the 6mm gravel spaced 28mm apart from center to center.

Also, note how the data for the array layouts begins to come together at high frequencies (>10000Hz) for the 30 m/s, but is quite spread by 60 m/s. This could be due to the correction scheme altering the smaller fetches data, where very little signal to noise ratio is present at the lower speeds, and not a true effect of the roughness noise. There is a change in slope that is apparent in the data as the speed is increased. At the lowest speed for the full fetch, the slope is -31 dB/decade, where at 60 m/s the slope is –20.0 dB/decade. This shows that as speed increases, the higher velocity produces more high frequency waves. However, the difference between layouts remains fairly consistent even with the addition of an increasing number of roughness elements.

In order to show better how the addition of roughness elements contributes to the overall far field sound generated by the flow over the roughness, Table 3-4 shows the dB levels for the increasing speeds at 6000, 9000, 12000, 15000, and 18000 Hz.

Much information can be gleaned from the presented sound levels. If one takes the dB difference from one layout to the next, it shows a consistent increase within each speed for all frequencies for the array based layouts. For example, in going from the 6x11 layout at 50 m/s to the 11x21 layout at the same speed for all five shown frequencies results in a consistent ~3.7dB increase. This consistency in dB increases across the frequency range between layouts holds for most of the data. However, the dB differences between the 11x21 layout and the full coverage fetch do not follow this. Looking again at 50 m/s, there is a change of 5.9dB at 6000Hz, but 8.1dB at 12000Hz. Similar variations are seen at other speeds.

One explanation for the array layouts showing consistent dB increases across all frequencies is that the spacing between elements is sufficient for them to act as individual elements and not see any effects from the surrounding elements. The flow returns to an undisturbed condition, so each element radiates the same regardless of position. However, the full fetch shows what is likely to be a shielding of the roughness elements, resulting in less consistent noise as the frequency is varied.

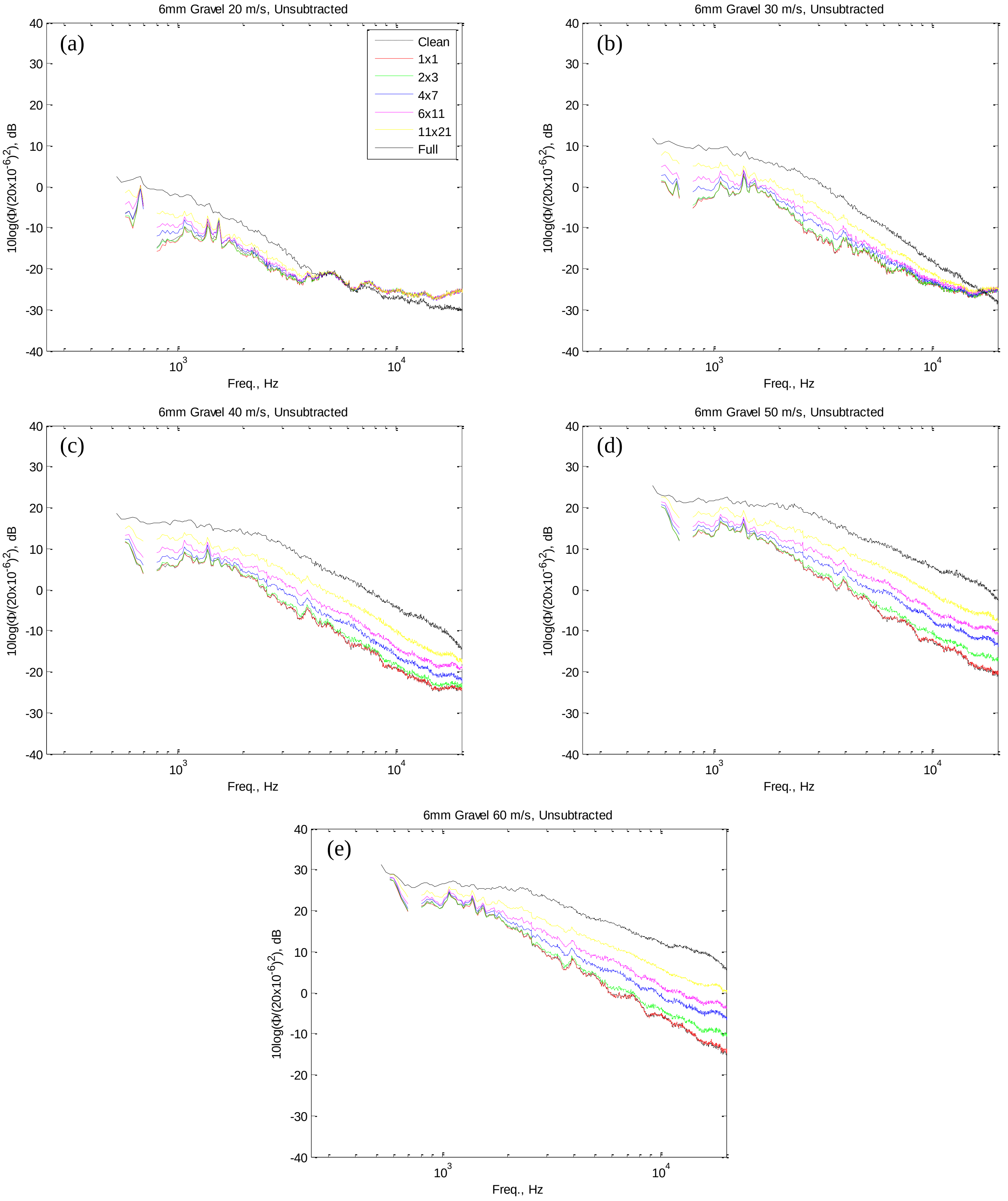

Figure 3-8 (a-e) - Far field sound spectra for the 6mm gravel including facility background noise. See top left figure for legend.

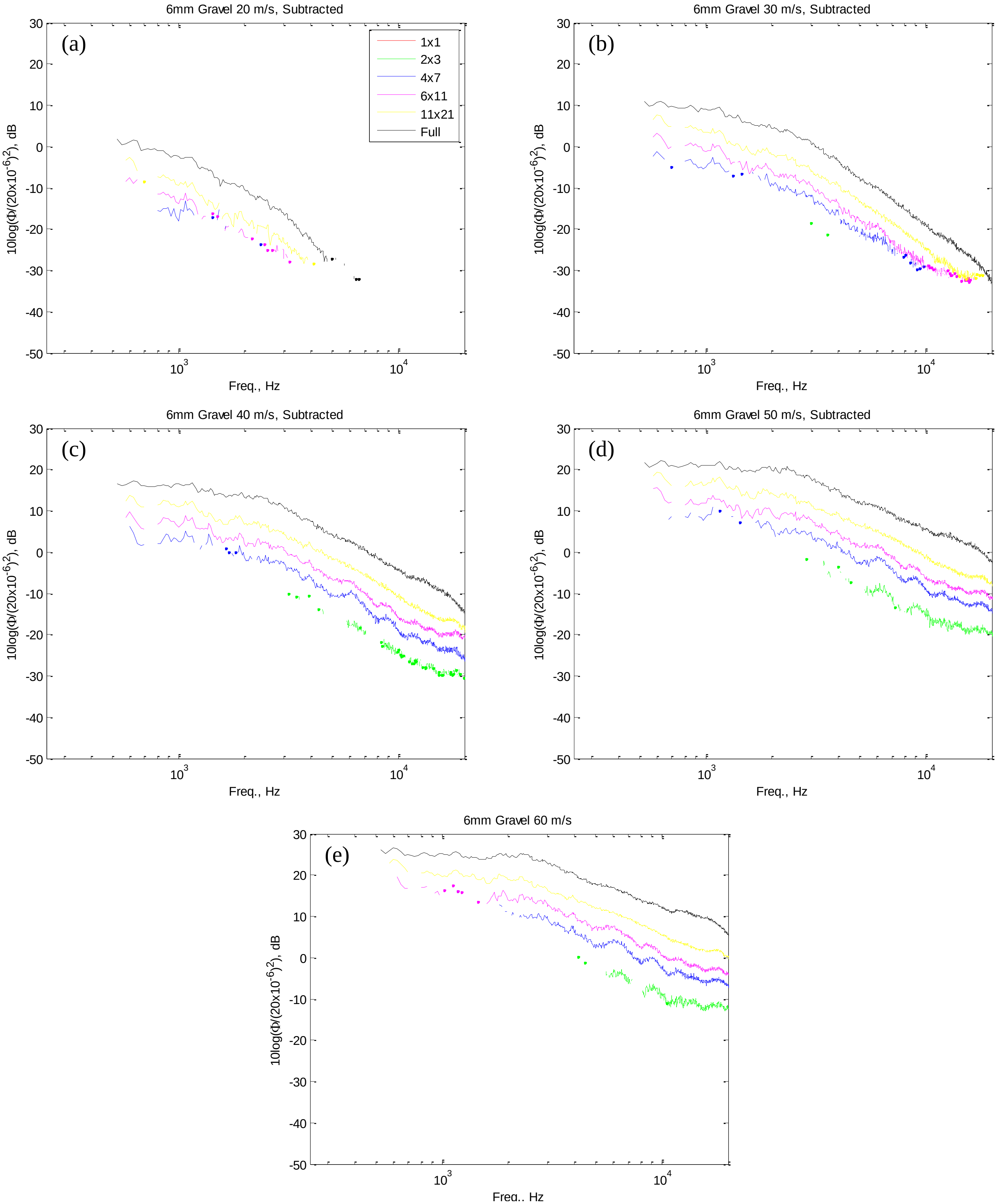

Figure 3-9 (a-e) - Far field sound spectra for the 6mm gravel with facility background noise subtracted, leaving only roughness noise. See top left figure for legend.

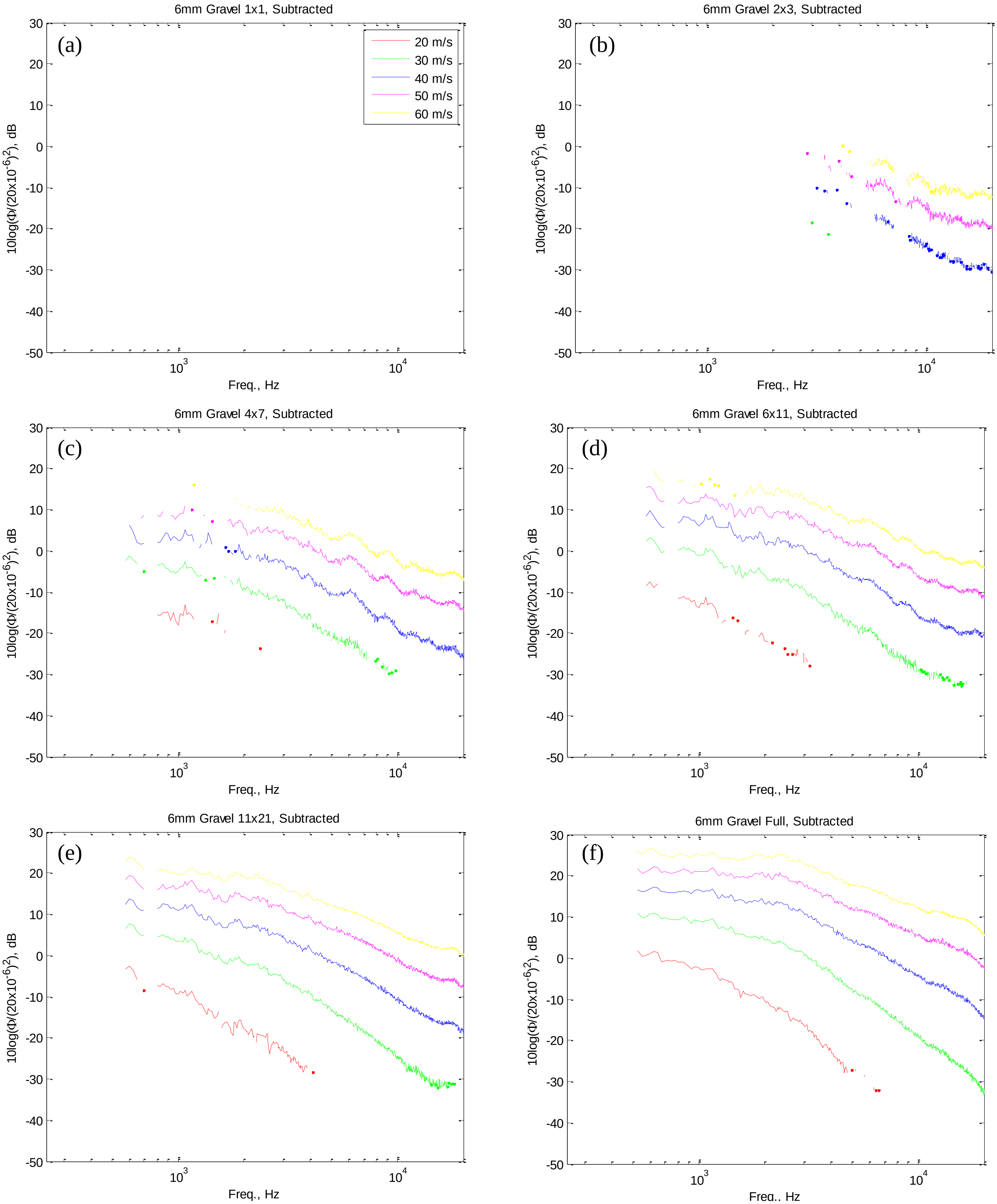

Figure 3-10 (a-f)- Far field sound spectra for the 6mm gravel with facility background noise subtracted, leaving only roughness noise. See top left figure for legend. Note, no data is present in (a), it is shown merely for completeness.

Also worth noting is the average increase in radiated SPL between layouts. Since the dB scale is a log scale, for every doubling of radiated sound, there is a 3dB increase. When increasing the elements from 6 in the 2x3 array to 28 in the 4x7 array, the average dB increase is 6.8. This is a 6.8dB increase for an almost 5 fold increase in the number of elements. From the 4x7 to the 6x11 array, a 2.4x increase in the number of elements, there is an average of a 2.9dB increase. When going from the 6x11 array to 11x21 element array, a 3.5x increase in number of elements, there is an average dB increase of 3.9. So, while the increase in the number of elements and the increase in radiated sound do coincide, there is a much larger increase per element added for the smaller arrays. As the arrays become larger, each added element results in less measured sound. This shows that normalizations cannot be made solely on the number of elements. There appears to be an effect of the distance and angle to the microphone from each element as well. This will be addressed in the normalization section, Section 3.4, later in the paper.

6mm gravel, dB							
Edge of Fetch Velocity (m/s)	Frequency (Hz)	1x1	2x3	4x7	6x11	11x21	Full
11.15	6000			-23.0	-19.4	-15.3	-9.9
	9000			-28.6	-27.6	-23.0	-17.2
	12000				-30.8	-28.1	-21.4
	15000					-31.1	-25.6
	18000						-29.3
14.76	6000		-17.8	-10.0	-6.8	-2.9	2.9
	9000		-22.6	-16.2	-13.0	-9.0	-3.3
	12000			-20.5	-17.4	-13.5	-6.3
	15000			-23.1	-19.8	-15.9	-9.2
	18000		-28.8	-23.8	-19.6	-16.4	-11.5
18.35	6000		-9.4	-1.0	1.5	5.2	11.1
	9000		-7.7	-0.4	3.0	6.7	13.1
	12000		-17.1	-10.3	-7.6	-3.6	4.4
	15000		-19.0	-12.6	-9.6	-5.5	2.1
	18000		-19.0	-12.7	-9.6	-6.0	-0.1
21.93	6000		-3.8	4.3	7.4	11.1	17.0
	9000		-13.3	-6.4	-4.3	0.3	6.5
	12000		-9.4	-3.4	-0.5	3.7	11.3
	15000		-12.3	-5.6	-2.5	1.7	9.6
	18000		-11.5	-5.1	-2.8	1.7	7.8

Table 3-4 - SPL from the 6mm gravel roughness elements, tabulated by speed, frequency, and layout. Blanks are shown when there was no measureable roughness noise above the background levels.

The above Figure 3-9 shows how, for a given speed, altering the layouts and adding more elements increased overall roughness noise. Next will be shown how altering the nozzle exit velocity for a given layout results in Figure 3-10.

The same axis and scales are used for this set of plots as for the earlier subtracted data. For reference to layouts, please see Section 2.4.1.

Notice how, again, the single element produced no measureable sound levels above that of the facility. By plotting in this manner, with the same layout shown and at difference speeds, the change in spectral shape with flow speed is much more apparent. The higher frequency sound level roll off becomes less steep with each increase in speed. Also, it is easier to see how the levels become closer to each other as speed is increased. Notice on the full layout in Figure 3-10 (f), at 3000 Hz, the difference between the 20 and 30 m/s data sets are 17 dB, whereas as the difference between the 40 and 60 m/s set is 10 dB for the same frequency. The compared velocities are proportionally different, so if the slopes were the same, the dB increase would be the same as well. This helps to show how the sound level slope is changing with increasing speed. All of the array data, Figure 3-10 (a-e), shows consistency in their spectral shape. The overall levels increase from -10dB for the 2x3 array at 60m/s and 10kHz, where the 11x21 array is about 15dB higher at 5dB for the same conditions. This being said, the overall shape of the data is very similar for these array type layouts. However, the full fetch, in Figure 3-10 (f), shows a steeper roll off at high frequencies not seen in the array data. This will be discussed further, but it shows a level of interaction between the elements in the full fetch layouts that is not present in the array layouts. To compare the radiated sound levels of the same layouts with varying speed, it is useful to hold the Strouhal number constant between comparison points. The selection of the Strouhal number was solely based on the data available, not for a specific physical purpose. The equation for the Strouhal number is given in Equation 15.

$$St = \frac{fL}{U_e}$$

Equation 15 – Strouhal equation

Where f is the frequency, L is the characteristic length, in this case the roughness height, and U is the flow speed at the front of the fetch. Since the roughness height remains constant for all layouts of the same elements, to maintain the same Strouhal number as velocity is increase, the frequency must increase proportionally. Shown in Table 3-6, the dB levels are shown with the varying layout, speed, and frequencies. Also shown in the far right column is how the dB level increases with a proportional increase in velocity. A doubling of SPL is equal to a 3 dB increase in sound level, so if the data increased as U^1, it would show a 3 dB increase from the 7.5 m/s edge velocity (which is the 20 m/s nozzle exit condition) to the 14.76 m/s edge velocity (or 40 m/s nozzle exit condition). From these proportional increases in speed and the increased dB levels, it can be shown with what exponent the dB scales on velocity, as seen by the U^n column.

Table 3-4 shows how the SPL varies as velocity is increased. Note for the lower frequencies, the increase is less rapid with flow speed. The Strouhal number for these data is 4.8, or about twenty four times the expected bulk vortex shedding frequency. The resulting variation, based on velocity, shows a trend of $\sim U^7 - U^8$, suggesting the radiated noise is from a mixture of dipole and quadrupole sources. The fact that the exponent is closer to 8 allows for the argument to be made that quadrupole sources are slightly stronger for this roughness size than the dipole sources, meaning the noise produced may be due more to turbulence in the near wall than from the roughness elements themselves. However, as will be shown in the following discussion on the normalization of this data, the data was shown to collapse successfully using a dipole model for the produced roughness noise.

6mm gravel, dB							
Edge of Fetch Velocity (m/s)		7.5	11.15	14.76	18.35	21.93	n (dB $\propto U^n$)
Frequency (Hz)		6000	9000	12000	15000	18000	
Layout	1x1						
	2x3			-26.0	-19.2	-11.4	7.55
	4x7		-28.5	-20.6	-12.7	-5.4	7.533333
	6x11		-27.6	-17.5	-9.6	-2.7	7.533333
	11x21		-23.0	-13.6	-5.7	1.8	7.822222
	Full		-17.2	-6.5	2.1	7.9	7.122222

Table 3-5 - Measured SPL of each layout as speed is varied while maintaining constant Strouhal number = 4.8

3.3.2 *9mm Gravel*

The 9mm gravel had the same six layouts as the 6mm gravel. Fetches were built from a single element in the front middle of the 0.254mm Mylar sheet up to an 11x21 grid with 28mm center-to-center spacing, and finally a full coverage of the 305x610mm Mylar sheet. These layouts are shown in Section 2.4.1 as reference. All of the measurements were made from a microphone in position D, which had been acoustically treated, so no scalloping is present in the raw data. Below, the results of the measurements are shown, including facility background noise, in Figure 3-11 (a-e).

As seen in the 6mm gravel data, with increasing speed comes increasing overall sound generated by each different layout, including the background levels. It is seen, again, that the electric noise floor of the microphone is reached at 2000 Hz for the 20 m/s measurements for all layouts in Figure 3-11 (a-e). Notice that at this 20 m/s speed, scalloping is present even in the large fetches. This is not seen in any of the other speeds, and is an artifact of the correction strategy. When no level is measured, i.e. when the microphone has reached its electric noise floor, the scalloping correction will introduce oscillations in the data. Once the speed has reached 30 m/s, however, the noise levels have increased so that the correction can properly reduce the oscillations. Some are still present in the single element and 2x3 layouts where the signal to noise ratio is still low. However, all of the larger fetches have been corrected and appear smooth. Notice also the hump that is forming for the full layout that is not present in the other fetches centered at 10200 Hz. This shows an interaction between the closely spaced full fetch that is not present in the layouts with the 28mm center-to-center spacing.

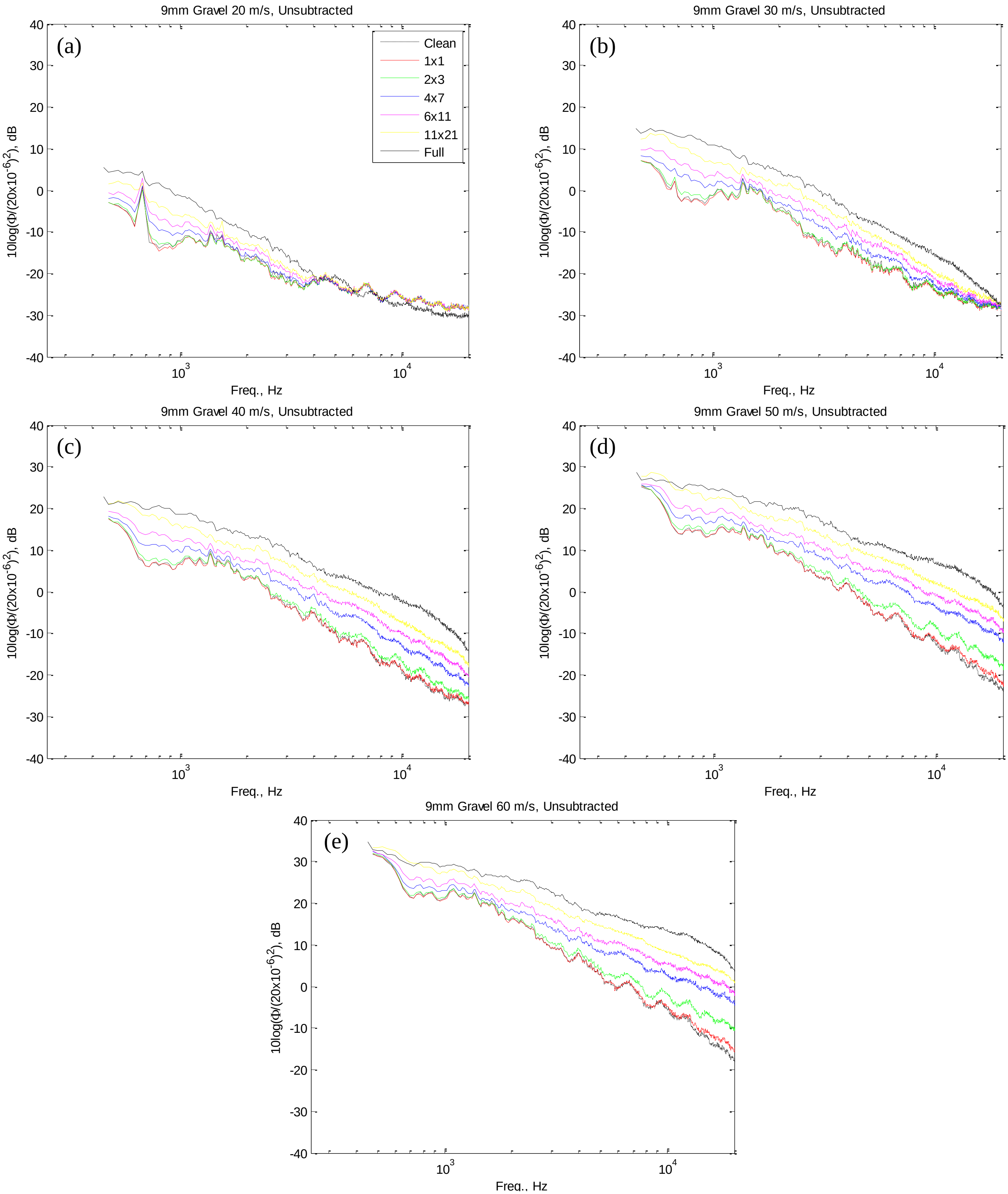

Figure 3-11 (a-e)– Far field sound spectra for the 9mm gravel including facility background noise. See top left figure for legend.

Next, the focus is shifted to the subtracted data. Using equation 0, it is possible to view only the noise added by the roughness elements. A 1dB threshold was applied in the subtraction, so only data that is greater than 1dB over the background level will remain. This is shown in the following Figure 3-12 (a-e).

Note that the range of the vertical axis has been modified from the unsubtracted plots. Many of the same features found in the unsubtracted data are still present here. The single and 2x3 element fetches still show the remnants of the scalloping correction, however all of the low speed scalloping is gone due to the subtraction. The hump seen in the unsubtracted data is still present for the full fetch at frequencies of 10kHz to 20kHz. As the speed increases, so do the overall levels of the roughness noise. For example, from 20 m/s to 60 m/s, at 4000 Hz, the SPL for the full fetch increased by 40dB, from -20 to 20dB. The 6x11 and 11x21 layout, over the same speed range and frequency, both increased by ~45 dB. It should be noted that the difference in the SPL between various layouts seems to decrease slightly as the velocity is increased. This is due to a change in the overall slope of the data from 20 to 60 m/s. There is a slope of -25 for the 20 m/s data, as seen in Figure 3-12 (a), and one of -15.5 at 60 m/s in Figure 3-12 (e).

The subtracted data also shows that a single element of 9mm roughness produces measureable sound levels over that of the background. Beginning in Figure 3-12 (d) and continuing to (e), the single element shows data above 10500Hz, along with an almost 10dB increase from the 50m/s to 60m/s nozzle exit velocity.

As was done with the 6mm gravel data, now will be shown the dB increases for each layout at each speed across the same five frequencies, and is shown in Table 3-6. Much of the same trends seen in the 6mm gravel roughness hold true here as well. There are consistent increases between the deterministic layouts over the range of frequencies and speeds. There is, on average, a 7.8dB increase when going from 6 elements to 28 elements, a 3 dB increase when comparing the 66 element layout to the 28 element, and a 2.9dB increase between the 11x21 layout and the 6x11 layout. Again, these differences cannot be correlated directly to an increase in the number of elements, but also to a change in radius and angle to the microphone. More work will be shown in the normalization section, Section 3.4.

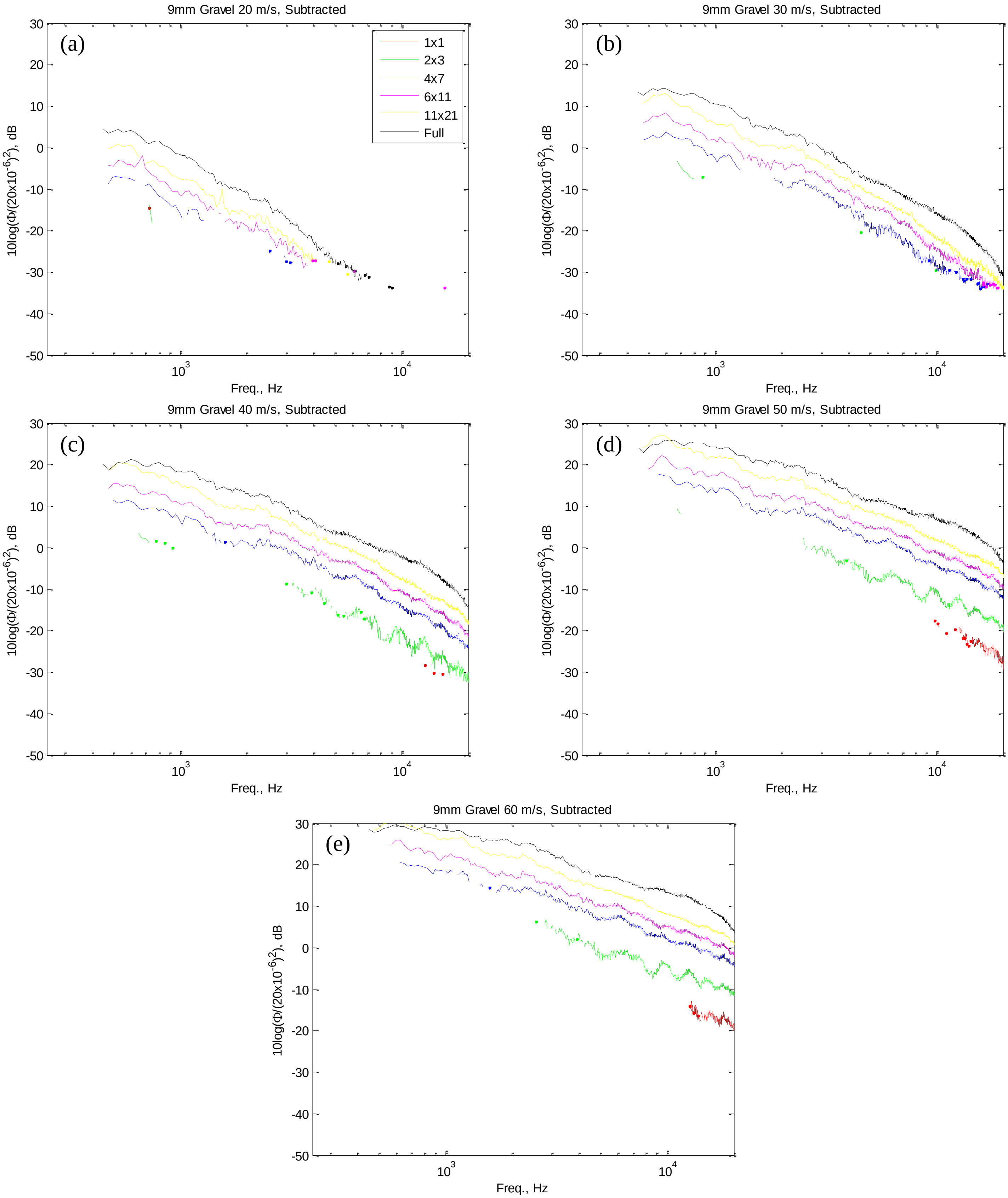

Figure 3-12 (a-e)- Far field sound spectra for the 9mm gravel with facility background noise subtracted, leaving only roughness noise. See top left figure for legend.

9mm gravel, dB							
Edge of Fetch Velocity (m/s)	Frequency (Hz)	1x1	2x3	4x7	6x11	11x21	Full
11.15	6000			-18.8	-15.0	-12.8	-9.3
	9000			-26.3	-23.2	-19.8	-13.9
	12000			-29.6	-26.0	-24.5	-18.3
	15000				-31.7	-29.6	-22.8
	18000				-32.9	-30.7	-26.9
14.76	6000		-16.2	-6.6	-3.4	-0.2	2.6
	9000		-22.6	-13.6	-10.2	-6.1	-0.8
	12000		-22.6	-15.7	-12.1	-9.7	-4.0
	15000		-26.7	-19.5	-15.9	-12.8	-7.5
	18000		-27.6 (f)	-21.0	-18.1	-14.6	-11.0
18.35	6000		-6.3	2.3	4.8	7.8	10.7
	9000		-11.1	-3.9	-1.0	3.0	8.1
	12000		-13.0	-5.3	-2.5	0.0	5.8
	15000		-15.2	-8.1	-5.2	-2.6	2.7
	18000	-23.5	-17.3	-9.5	-6.6	-3.7	-0.3
21.93	6000		-0.8	7.8	10.6	13.2	16.6
	9000		-5.3	2.9	5.2	9.1	14.4
	12000		-6.0	1.2	4.3	6.7	12.5
	15000	-17.1	-8.0	-0.4	1.8	5.0	9.8
	18000	-15.8	-8.8	-2.2	0.7	3.2	7.1

Table 3-6 - SPL from the 9mm gravel roughness elements, tabulated by speed, frequency, and layout

Figure 3-13 (a-f) is the same subtracted data, but plotted holding the layout constant and showing how speed can vary the results. Again, the spectral features remain consistent with before, but now the change in slope over all layouts is readily apparent. The oscillations in the single and 2x3 layouts also show that the peaks and valleys line up. The hump in the full layout is now seen to be growing as speed is increased. The full fetch data shown in Figure 3-13 (f), when compared to the array data of Figure 3-13 (a-e), shows a definite roll off at all velocities at high frequency that is not seen in the array layouts. Using Figure 3-13 (e) as an example, when comparing the overall level increase between velocities, the change in slope is seen. At 2000Hz, from 20 to 30m/s, a 50% increase in velocity, the overall radiated noise level is seen to increase by 20dB. However, between 40 and 60m/s, proportionally the same 50% increase, the levels increase by 15dB. This result is consistent in the other layouts.

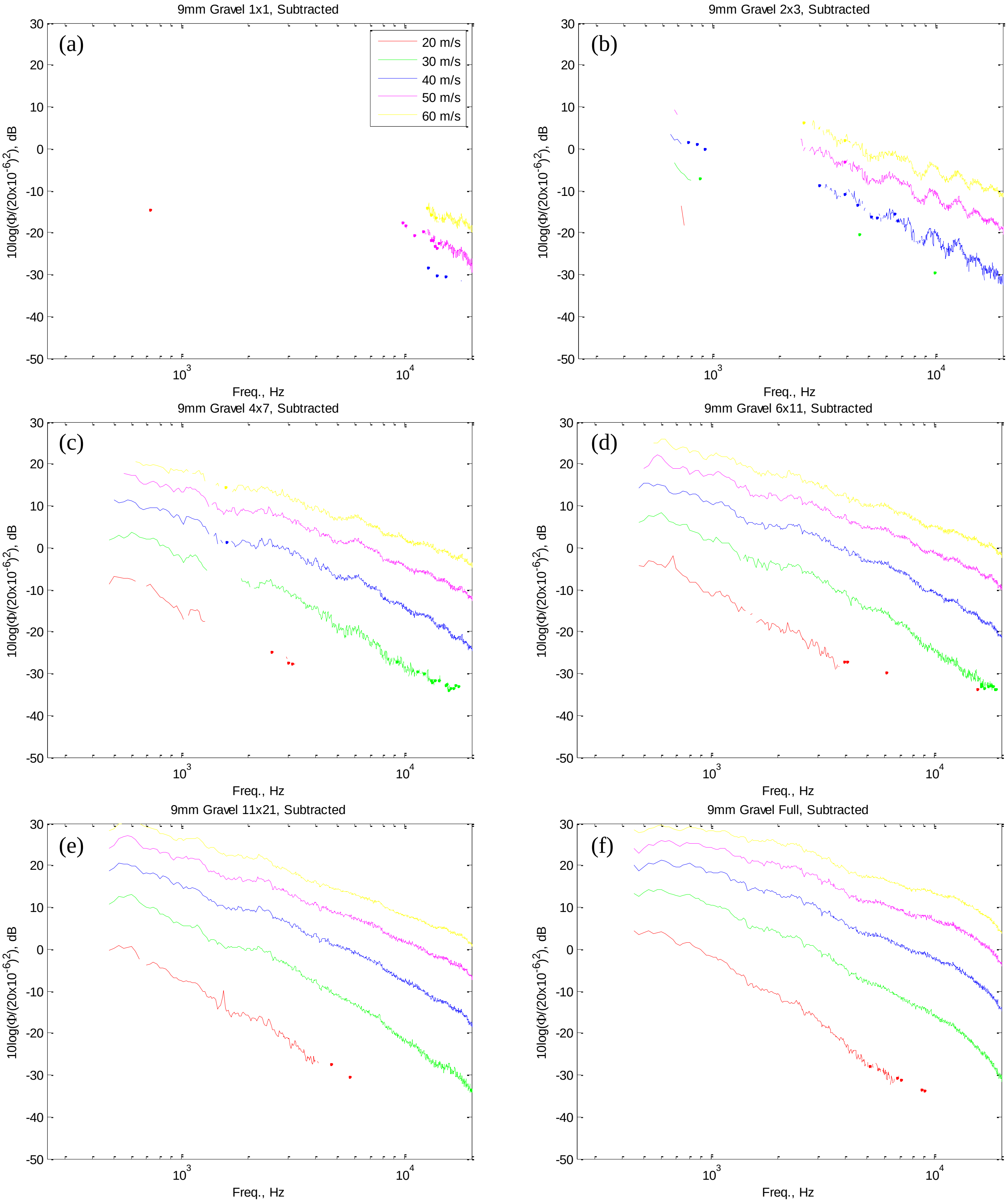

Figure 3-13 (a-f)- Far field sound spectra for the 9mm gravel with facility background noise subtracted, leaving only roughness noise. See top left figure for legend.

Using a Strouhal number of 7.2, where the frequencies and speeds are the same as with the 6mm gravel but the characteristic length is now 9mm, the following trend emerges.

9mm gravel, dB							
Edge of Fetch Velocity (m/s)		7.5	11.15	14.76	18.35	21.93	n (dB $\propto U^n$)
Frequency (Hz)		6000	9000	12000	15000	18000	
Layout	1x1				-23.1	-16.1	7.0
	2x3			-23.3	-14.8	-8.9	6.55
	4x7		-26.8	-15.9	-7.7	-2.0	6.965556
	6x11		-23.5	-12.5	-4.8	0.8	6.783333
	11x21		-19.9	-9.8	-2.0	3.3	6.527778
	Full	-29.3	-14.0	-3.9	2.8	7.0	6.43125

Table 3-7 - Measured SPL of each layout as speed is varied while maintaining constant Strouhal number = 7.2

The data now shows a trend of ~U^6-U^7, which could suggest that the radiated noise is due more to the scattering from the roughness is dominating.

3.3.3 *3mm Cubes*

The 8 layouts of 3mm cubes, as shown in Section 2.4.2, were mounted on the 0.13mm Mylar substrate. In much the same method as the previous gravel layouts, the cube layouts began with a single element with more streamwise and spanwise rows or columns added until the final 6x7 element grid was constructed. There was no full grid as there was with the gravel, however, as this would have resulted in a smooth 3mm tall plate for all intents and purposes.

Much like the gravel data, these are plotted on a semi logarithmic scale from 250 to 20000 Hz on the x axis, and from -30 to 50 dB, as normalized by 20×10^{-6} Pa. There are more layouts for the cubes than there was for the gravel, resulting in a slightly busier looking plot. Also, the element array only goes to 42 total elements, where the gravel arrays went up to 231 elements in the largest grid arrangement. That, combined with the smaller 3mm size of the cubes, results in far less signal to noise ratios.

Once again, the $1/f$ electrical noise floor is reached by all of the layouts at the lowest speeds of 20 and 30 m/s. The small spikes seen in the 30 m/s plot are attributed to electrical noise and are not real phenomena. Because of the acoustically treated microphones and stands, there are no artifacts left from the scalloping correction as there was in the gravel data. Even though the element size is only 3mm, there is still distinguishable noise above that of the facility. At 40m/s, a definite increase of 7dB over the background level is seen for the 6x7 element layout. By 60m/s, in Figure 3-14 (e), this has become a 12dB increase over the clean Mylar levels. This, and the implications, will become more obvious once the background noise is subtracted out, as shown in Figure 3-14 (a-e).

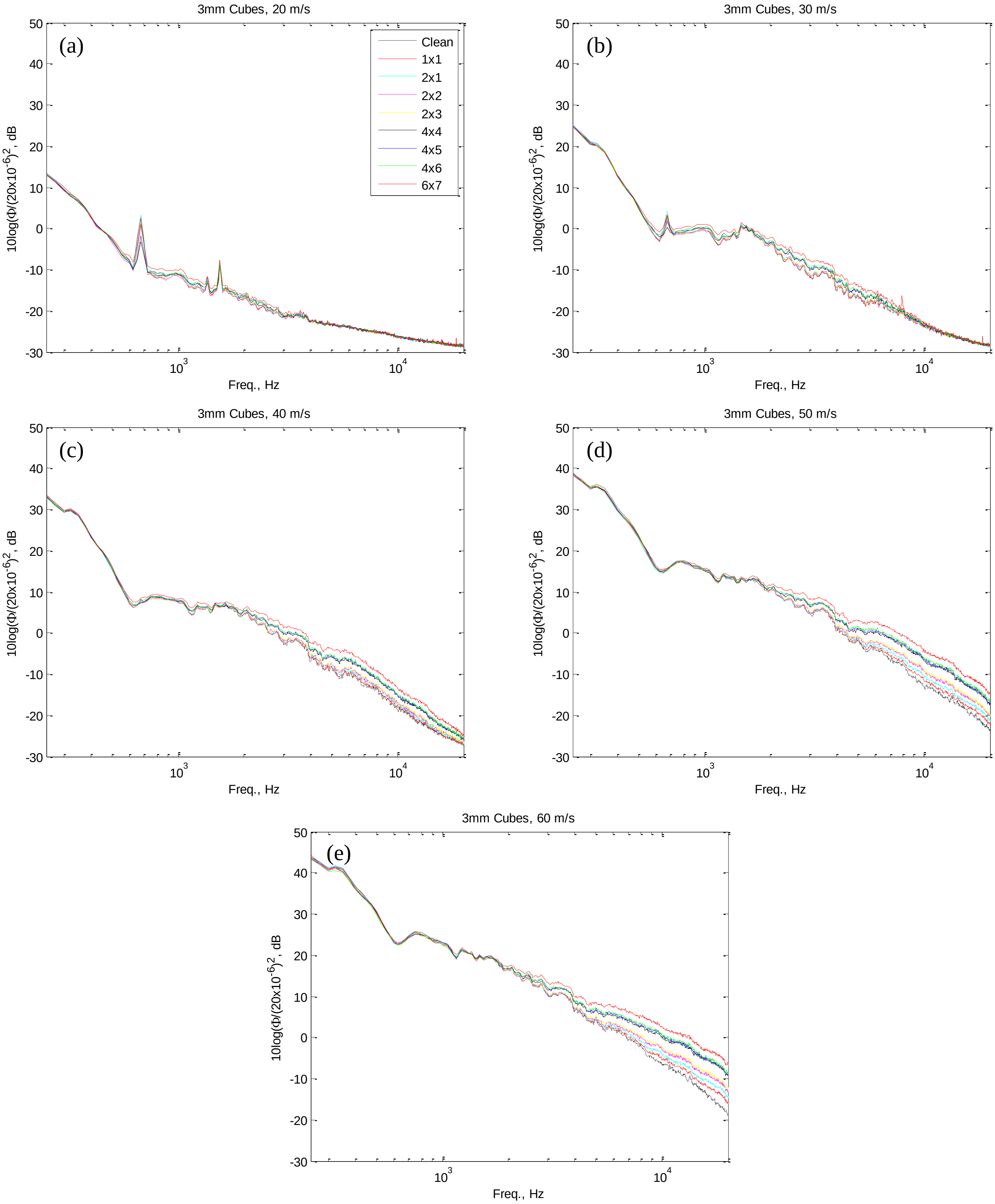

Figure 3-14 (a-e)- Far field sound spectra for the 3mm cubes including facility background noise. See top left figure for legend.

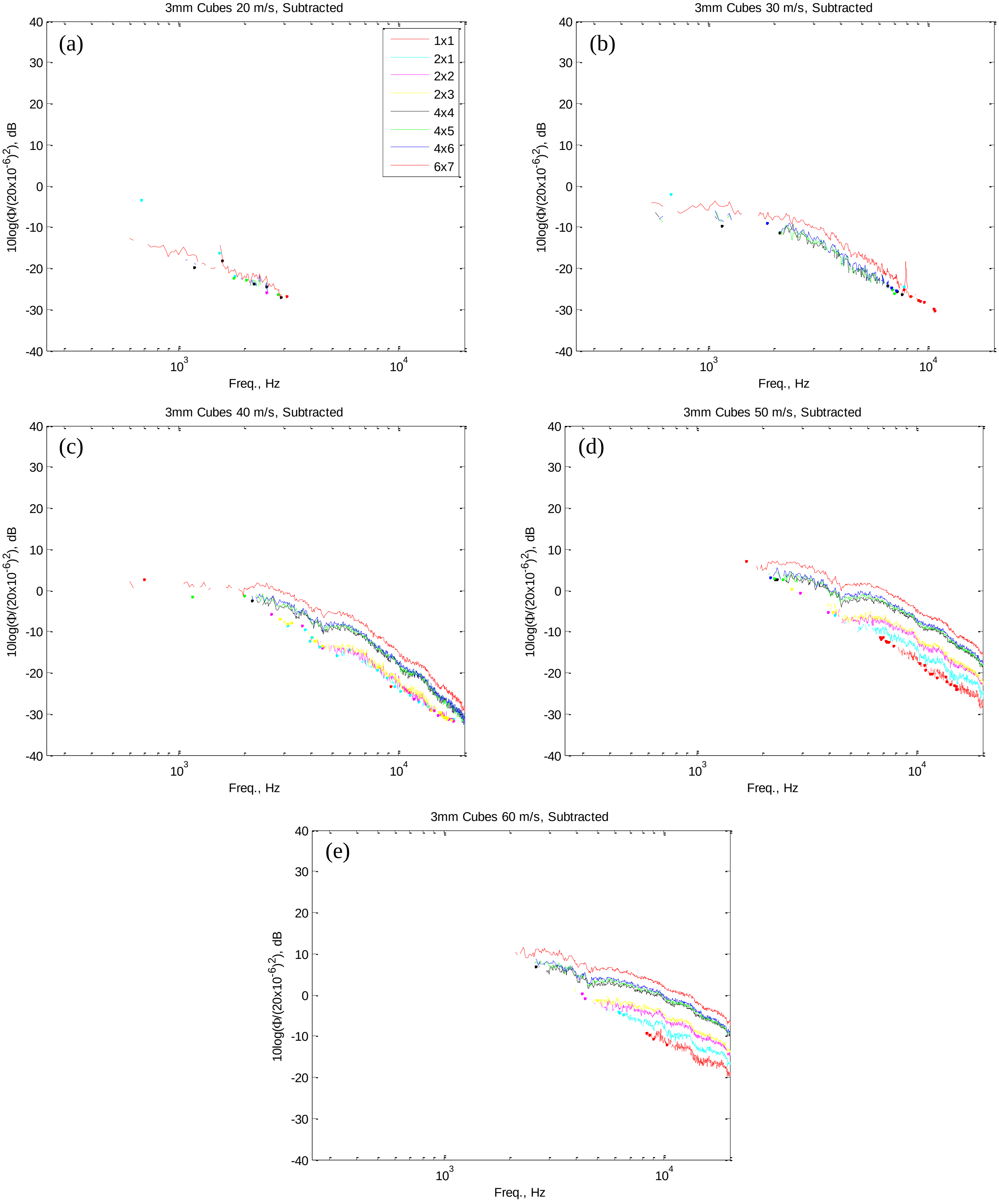

Figure 3-15 (a-e)- Far field sound spectra for the 3mm cubes with facility background noise subtracted, leaving only roughness noise. See top left figure for legend.

From the above, one exciting fact is that the Virginia Tech Anechoic Wall Jet facility is capable of distinguishing a single 3mm cube above the background noise. For the 50 m/s data set, the actual edge velocity at the single element is 18.3 m/s, and the boundary layer height is 17.0mm. It is possible to hear a single cube, less than 20% of the boundary layer thickness in height. And even at the lowest speed of 20m/s at the nozzle in Figure 3-15 (a), resulting in an edge velocity at the beginning of the roughness of 7.5 m/s, where the boundary layer is 20.9mm thick, the 6x7 grid still produces noticeable noise above the background. The element size is roughly 1/7th of the boundary layer in this flow. Not only this, but by increasing from the single element to a gird of 42 elements, there is an increase of 15 dB at 60 m/s. Unlike the gravel measurements, where there was a layout of closely touching elements, there is no noticeable difference between one layout and the next except for the raised noise levels. These elements, spaced 16.5mm center to center, produce little if any interact between elements. Also, notice that the acoustically treated microphones and stands resulted in practically no scalloping, thus showing a marked improvement in tunnel measurement capabilities. Shown below in Table 3-8, the SPL differences when going from one layout to the next are shown.

3mm cube, dB									
Edge of Fetch Velocity (m/s)	Frequency (Hz)	1x1	2x1	2x2	2x3	4x4	4x5	4x6	6x7
11.15	6000					-22.6		-22.7	-19.6
	9000								
	12000								
	15000								
	18000								
14.76	6000			-14.1	-13.4	-9.6	-9.2	-8.4	-6.0
	9000			-22.0	-20.7	-16.6	-16.2	-15.6	-13.4
	12000			-25.2	-24.6	-20.2	-20.4	-19.7	-17.5
	15000					-25.1	-25.9	-25.0	-22.9
	18000					-29.2	-29.0	-28.7	-26.2
18.35	6000			-8.1	-6.6	-2.1	-1.5	-1.0	1.7
	9000		-13.7	-9.9	-10.1	-6.2	-6.1	-5.6	-3.1
	12000		-17.2	-14.2	-13.0	-9.5	-9.1	-8.5	-6.9
	15000		-20.9	-18.4	-17.3	-13.2	-13.3	-12.4	-10.7
	18000	-24.4	-21.7	-19.4	-19.5	-15.6	-15.7	-15.3	-12.9
21.93	6000			-3.1	-2.4	2.6	3.1	3.9	5.8
	9000		-8.0	-4.9	-3.7	-0.2	0.3	0.9	3.1
	12000	-12.1	-10.2	-7.6	-6.3	-2.2	-1.8	-1.6	0.2
	15000	-16.5	-13.4	-10.4	-9.6	-5.8	-5.3	-5.1	-2.8
	18000	-17.5	-14.1	-11.8	-11.4	-7.6	-7.1	-6.9	-4.6

Table 3-8 - SPL from the 3mm cube roughness elements, tabulated by speed, frequency, and layout

Again, there are very consistent increases between layouts throughout all frequencies and speeds. The average of the difference between consecutive layouts (meaning 1x1 to 2x1, or 4x4 to 4x5) at the same velocity and frequency was taken. These averages showed that the increases are very consistent throughout the range of speeds and frequencies as one progresses through the buildup of the layouts. This data also shows very little interaction between elements. When going from one element in the 1x1 layout to two in the 2x1, the average increase in SPL is 2.7dB. With no interaction, one would assume a doubling of SPL, or a 3dB increase, which is very close to what is shown here. Again, going from 2x1 to 2x2 also shows an average increase of 2.8dB. Finally, going from the 4x5 to 6x7 element layouts, which is approximately a doubling, shows an average increase of 2.7dB. This leads to the conclusion that there is very little interaction between the 3mm cubes, less than was seen with the 9mm.

As was done with the gravel data, a comparison of the measured SPL for consistent layouts will be shown in Figure 3-16, followed by Table 3-9 showing the consistent Strouhal numbers for the far field sound.

Again, take notice of the large amount of noise, solely due to roughness, that is able to be discernibly measured above that of the facility. With the gravel data, it was possible to measure the slope and change in slope from the lowest speed to the highest. There is not enough low speed data to do the same for this element size accurately, but it is still possible to show a change from 30 m/s to 60 m/s. At 30 m/s, the slope of the subtracted data for the 6x7 grid is found to be-26.8 dB/decade and -21.5 dB/decade for the 60 m/s case.

The Strouhal chosen number for the cubic elements is 2.4, which is almost twelve times the expected bulk vortex shedding value. This data shows a strong U^6 dependence. One should notice that even though these elements are half the size of the 6mm gravel, they are much more efficient at radiating noise to the far field due to their sharp corners as seen by the measurable sound for a single cubic element along with increased dB levels for comparable element configurations (such as the 2x3 layout).

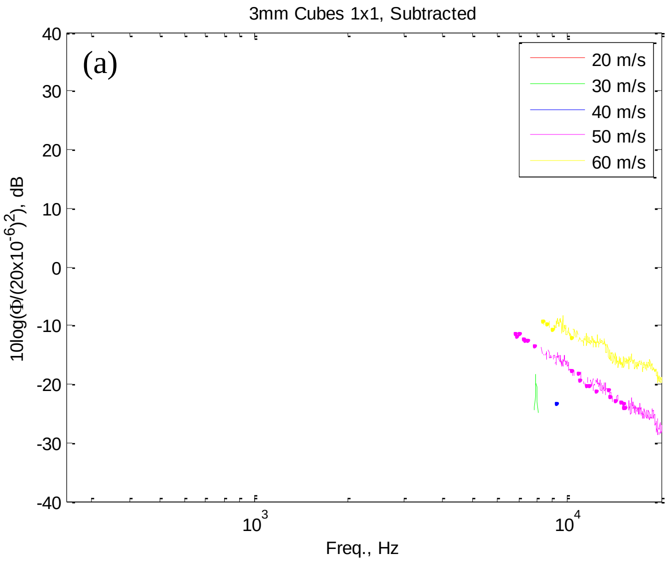
3mm Cubes 1x1, Subtracted

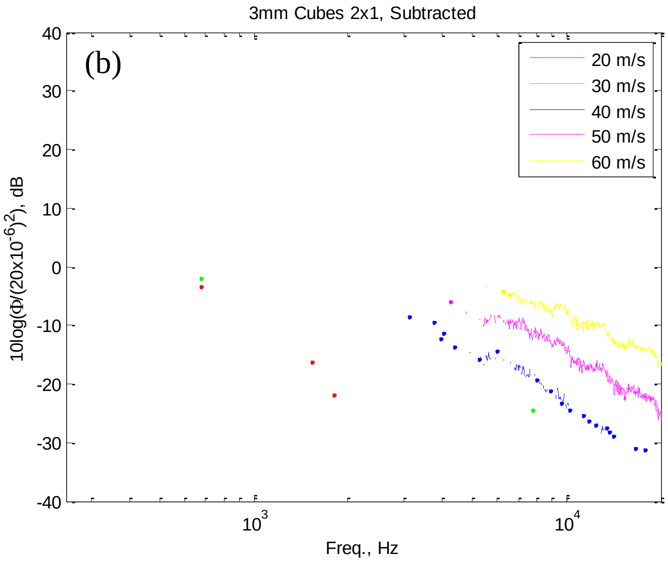
3mm Cubes 2x1, Subtracted

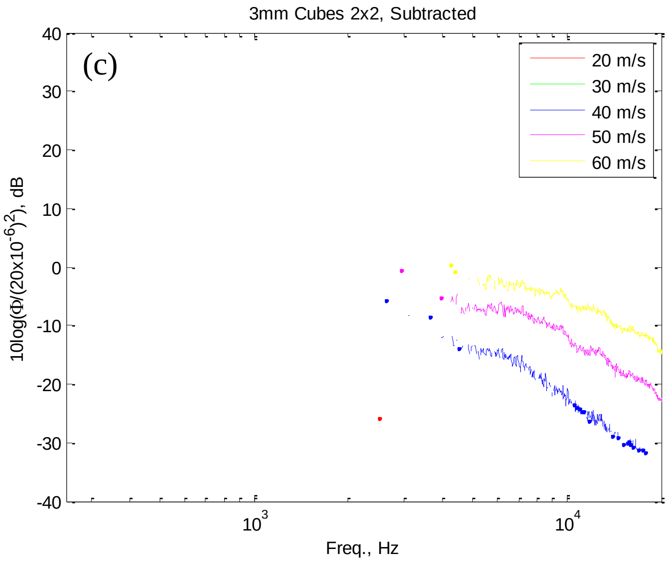
3mm Cubes 2x2, Subtracted

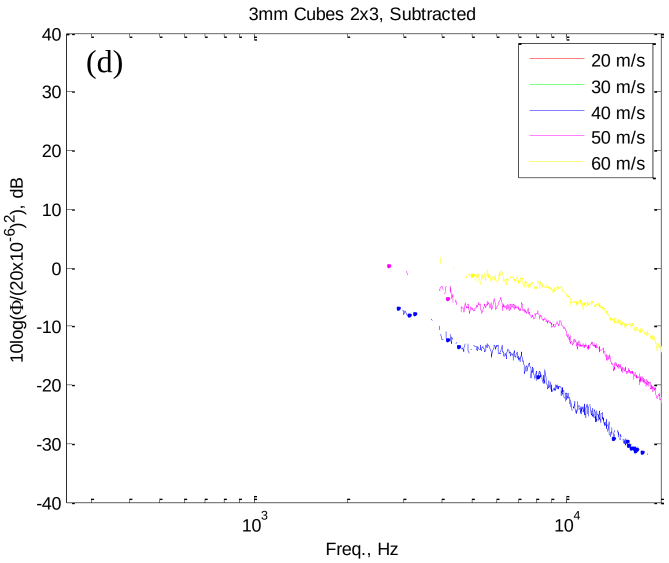
3mm Cubes 2x3, Subtracted

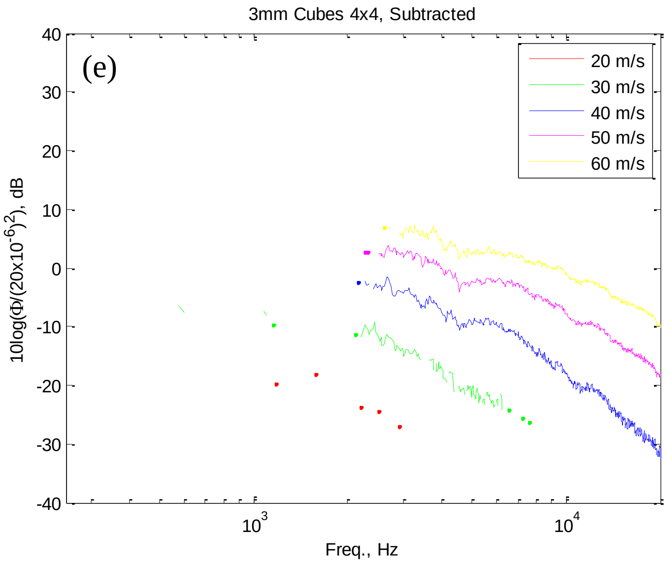
3mm Cubes 4x4, Subtracted

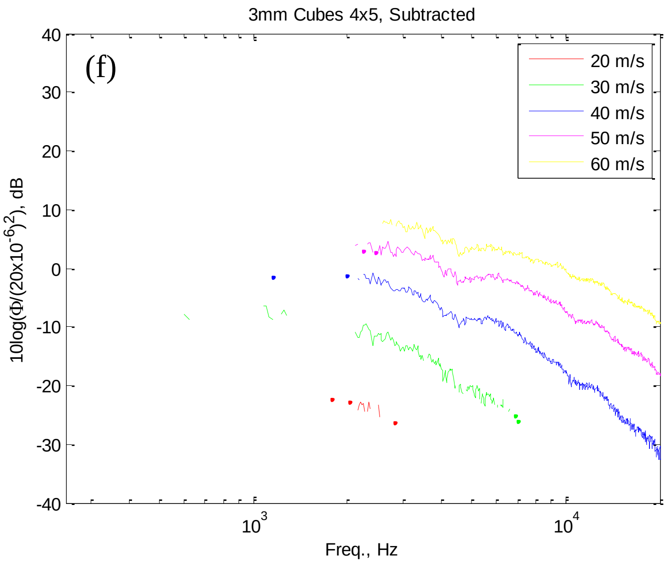
3mm Cubes 4x5, Subtracted

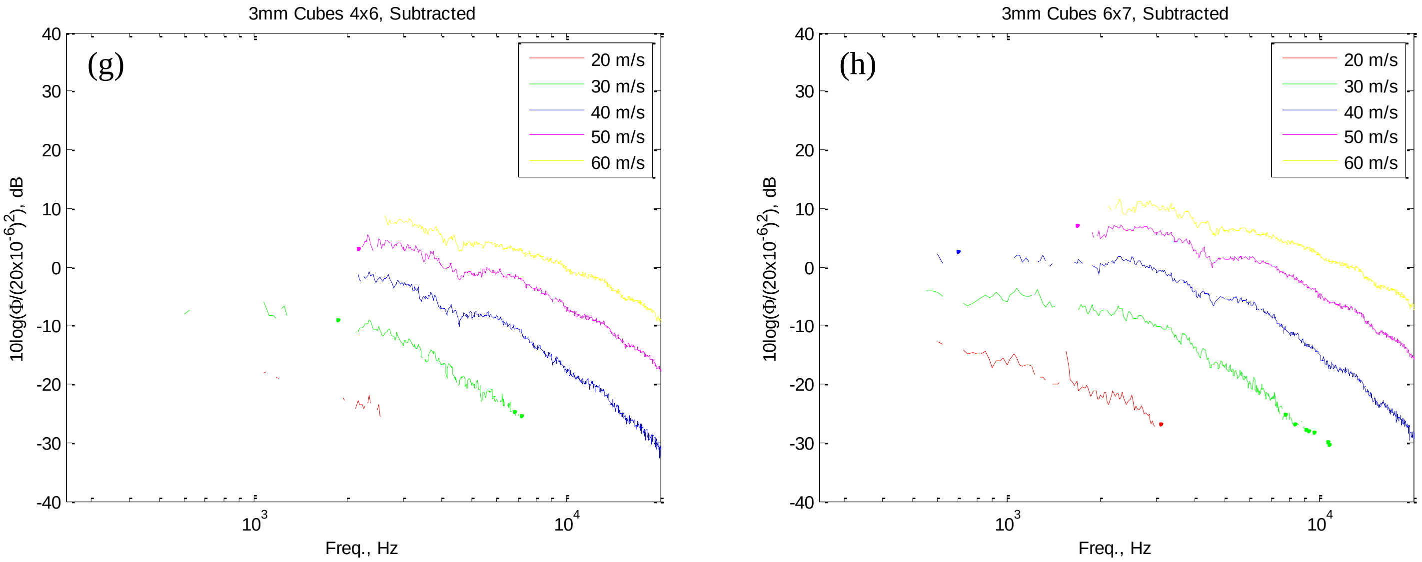

Figure 3-16 (a-h)- Far field sound spectra for the 3mm cubes with facility background noise subtracted, leaving only roughness noise. See top left figure for legend.

3mm cube, dB							
Edge of Fetch Velocity (m/s)		7.5	11.15	14.76	18.35	21.93	n $(\text{dB} \propto U^n)$
Frequency (Hz)		6000	9000	12000	15000	18000	
Layout	1x1					-17	
	2x1				-21.2	-14.3	6.9
	2x2			-25.6	-18.2	-11.8	6.65
	2x3			-24.5	-17.2	-11.3	6.25
	4x4			-20.3	-13.1	-7.4	6.075
	4x5			-20.1	-13.1	-7.2	6.175
	4x6			-20	-12.5	-6.9	6.075
	6x7		-27.5	-17.7	-10.7	-4.5	6.822222

Table 3-9 - Measured SPL of each layout as speed is varied while maintaining constant Strouhal number = 2.4

3.3.4 *Comparison of Similar Layouts for Different Size Roughness Elements*

All of the previous measurements have shown only one type of roughness on a given plot. Without a direct comparison of the data of different element shapes, it is difficult to see what effect, if any, the size and shape of the roughness elements have on the radiated noise. By exploring the sound generated by a consistent layout for each roughness type, it is possible to see how these shapes and sizes play a key role in the generation of roughness noise. For this discussion, data was chosen from the 2x3 arrays of each element type, at speeds of 40, 50, and 60m/s (where all element types generated measureable sound levels). Figure 3-17 (a-c) show the comparison of the cubic and both gravel elements' 2x3 arrays' far field subtracted noise.

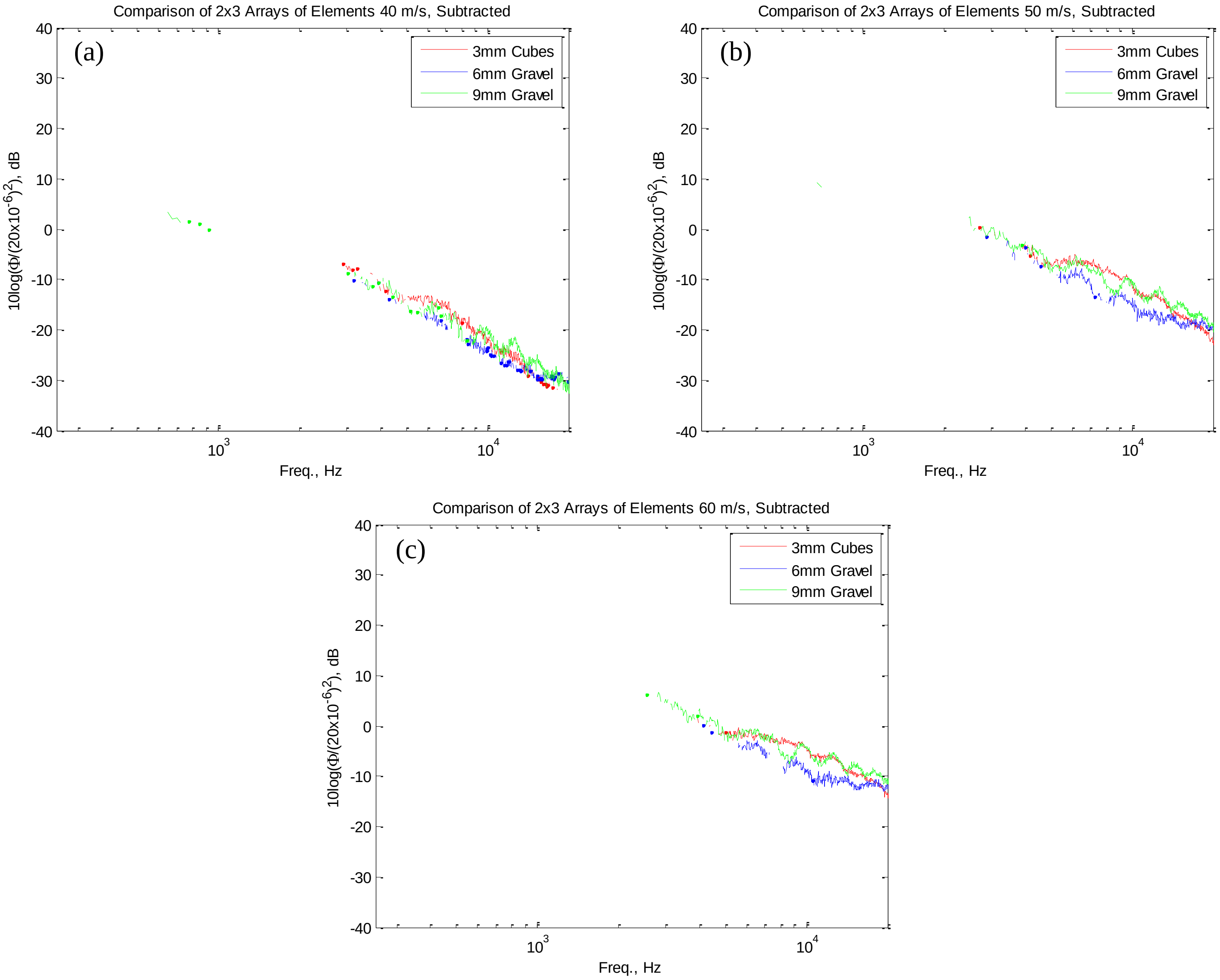

Figure 3-17 (a-c) – Far field sound spectra for the 3mm cube, 6mm and 9mm gravel 2x3 arrays at 40, 50, and 60m/s, respectively.

In the gravel data, there is still scalloping present as mentioned earlier. However, the main concern is the overall level and shape of the radiated noise, so this is not of concern for this discussion. In Figure 3-17 (a), which is the 40m/s case, it is readily seen that the 3mm cubes are radiating 4dB more noise than the larger, 6mm gravel. Interesting to note is that the 9mm gravel sound level lays relatively on top of the 3mm cube's level. The same trend continues in both (b) at 50m/s, and (c) at 60m/s. At all frequencies up to ~15kHz, the cubic element array is well above the 6mm gravel array. At all frequencies, the 9mm gravel and 3mm cubic arrays are lined up well. The spectral shape itself is consistent for all elements, so it is possible that the mechanisms creating the roughness noise are the same and that there is no interaction between elements. The levels are quite different. This shows that shape definitely plays a role in the amount of radiated sound by these large roughness elements. Apart from size, the sharp corners of the cubes are the biggest difference between these roughness types, and hence the increased levels can be partially attributed to them. Another difference is the overall shape of the element. Whereas the gravels are rounded, allowing for the flow to move around the element, the cubes have a blunt face. The following discussion, on the 3mm hemispherical roughness, will show the opposite end of the spectrum. The elements are both low profile and have no face perpendicular to the flow. A comparison of the hemispherical and cubic roughness will follow.

3.3.5 *3mm Hemispheres*

The 3mm radius hemispheres were made on a substrate of Kevlar using a two part epoxy and mold. Only one mold was made, being set up in a 6x7 grid. Because of this, less data was able to be taken. The clean Kevlar sheet, which was shown before, and the 6x7 sheet of hemispheres, as shown in Section 2.4.3, were both measured in the tunnel using microphone position E, as listed in Table 3-3. Because of the process used to make the hemispheres, the elements could not be added like they were for the gravel and cubic roughness. Below is shown the unsubtracted data.

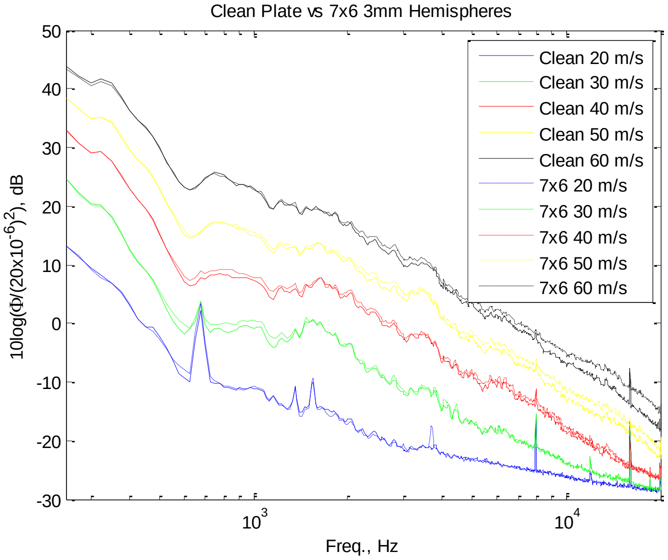

Figure 3-18 - Far field sound spectra for the 3mm hemisphere 6x7 array including facility background noise.

The data is plotted on the same scale as the gravel and cubic elements, from 250 to 20000 Hz on the x axis and dB normalized on $20\text{x}10^{-6}$ on the y axis. The spikes seen at 8000 and 14000 are both due to electrical noise. With the microphone acoustically treated, no scalloping was present. Using the subtraction Equation 14, Figure 3-19 shows the noise due only to the roughness noise of the 3mm hemispheres.

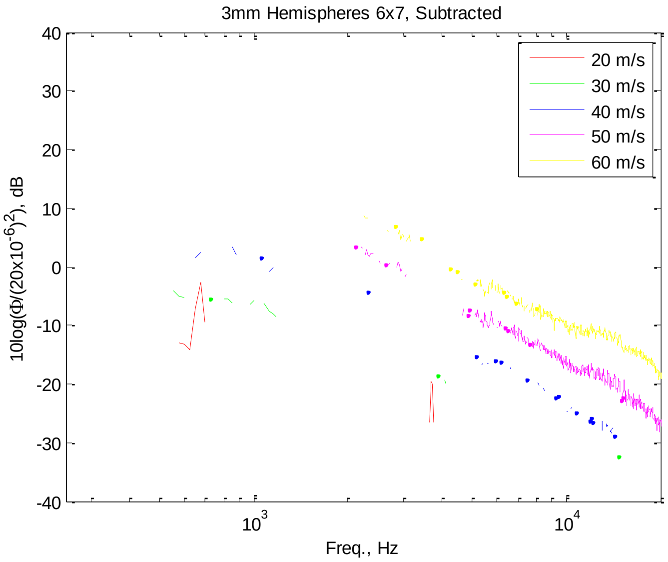

Figure 3-19 - Far field sound spectra for the 3mm hemisphere with facility background noise subtracted, leaving only roughness noise.

The hemispheres produced very small levels of roughness noise as compared to the 6x7 cubic elements. Only data at 50 and 60 m/s provide data, and only at frequencies above 5000 Hz. But it is still interesting to show that something as smooth as a hardened epoxy 3mm hemisphere can produce measureable roughness noise in the Virginia Tech Anechoic Wall Jet facility.

3mm hemisphere, dB						
Edge of Fetch Velocity (m/s)	7.5	11.15	14.76	18.35	21.93	n (dB ∝ U^n)
Frequency (Hz)	6000	9000	12000	15000	18000	
7x6			-26.1	-22.3	-15.6	5.9

Table 3-10 - Measured SPL of each layout as speed is varied while maintaining constant Strouhal number = 0.9

The above table, holding the Strouhal number at 0.9, shows a dependence of U^6. Even with the fairly limited amount of measureable roughness noise, it is seen to scale as would be assumed with a dipole source.

3.3.6 *Comparison of Hemispherical and Cubic Roughness Noise*

As only the 6x7 array of hemispheres was available for measurement, the comparison will be limited to the same 6x7 array of cubic elements. Shown in Figure 3-20 is the subtracted data for the 6x7 array of both roughness types. All measured data is shown.

The subtracted data shows that, as suspected, the hemisphere roughness is much less efficient at generating far field noise than that of the cubic elements, even though the forward projected area of the hemispheres is 1.57 times larger than the cubic elements. The cubic 6x7 array produces measurable noise levels at 20m/s, where the hemispheres don’t until 50m/s. As mentioned previously, the shape of the hemispheres allows for the flow to progress downstream with minor disturbances, much less than with the perpendicular face of the cubic elements. While the levels of the measured spectra are approximately 10-12dB lower for both cases, the shape remains similar. When comparing the 50m/s hemispherical array sound levels to that of the cubic array at 50m/s, the spectral shape of the data is very similar. The same can be said for the 60m/s data. If the overall levels are boosted, the data lines up well on top of each other. This being said, the argument that the mechanism for creating this roughness noise are consistent between roughness types holds true. Building on this basic assumption, a normalization proposed by Glegg *et al.* (2007) is presented is Section 3.4.

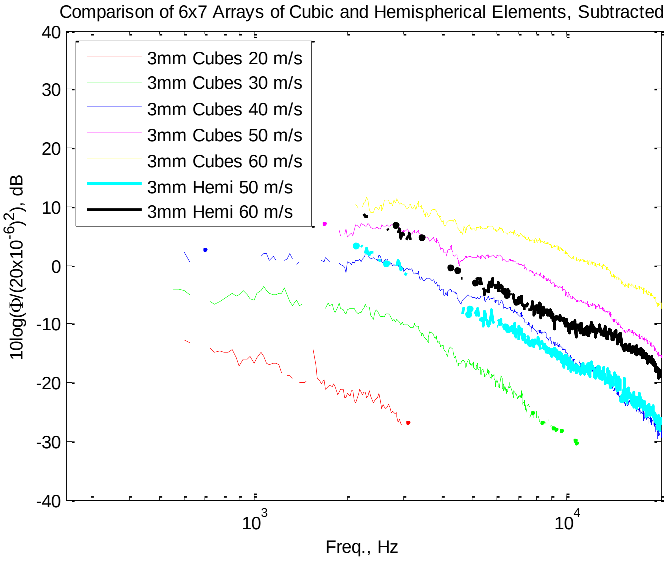

Figure 3-20 - Far field sound spectra for the 3mm cubic and 3mm Hemispherical 6x7 arrays.

3.3.7 *Comparison to Alexander (2009) Small Element Roughness*

Mentioned previous was the work done by Alexander (2009) in collapsing the data from sandpaper type roughnesses based on the wall pressure spectrum. There is a characteristic difference between his type of roughness and the large scale roughness that is a considerable fraction of the boundary layer studied here. A comparison will be shown in Figure 3-21 and Figure 3-22 for the largest grid arrays of large element roughness, 11x21 for both gravel sets and 6x7 for the cubic and hemispherical sets, versus that of Alexander's 305x610mm roughness patches of 20, 40, and 80grit sandpapers. Also shown will be a comparison of the full 6 and 9mm gravel patches, of the same dimension as Alexander's patches. The data in Figure 3-21 and Figure 3-22 has been subtracted using the method shown in Equation 3.3.

The overall spectral shape of the sandpaper roughness is quite different than that of the large element grids in Figure 3-21. The sandpaper roughness increases in SPL with increasing frequency for all three grit sizes, whereas the array data consistently decreases in level with increasing frequency. These large elements in the grid array do not exhibit interaction between the elements, resulting is the steady roll off at high frequencies. The sandpaper roughnesses, however, do interact, leading to higher levels at the higher frequencies before they roll off above 8kHz for the 20 and 40 grit and 11kHz for the 20kHz. In this comparison, only the spectral shape is of concern as a direct comparison of levels would be misleading. The 6x7 arrays are not 1/6th the size of the 11x21 or sandpaper arrays.

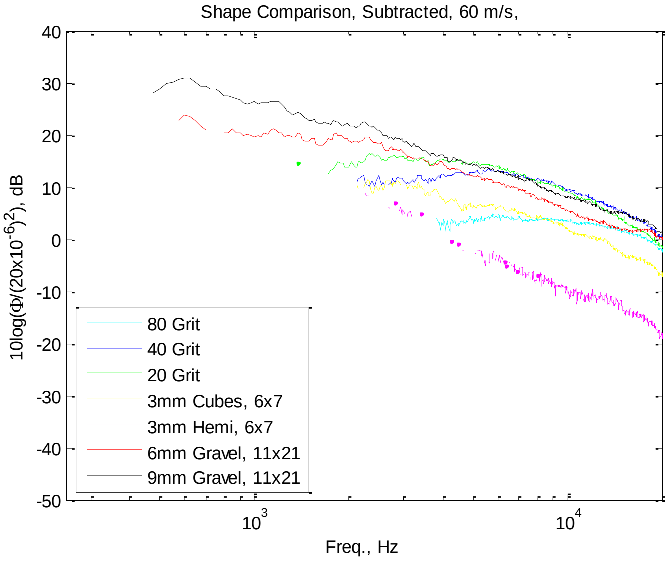

Figure 3-21 - Far field subtracted comparison of 20, 40, and 80 grit sandpaper fetches vs the 6x7 3mm cubic and hemisphere arrays and the 11x21 6 and 9mm gravel arrays

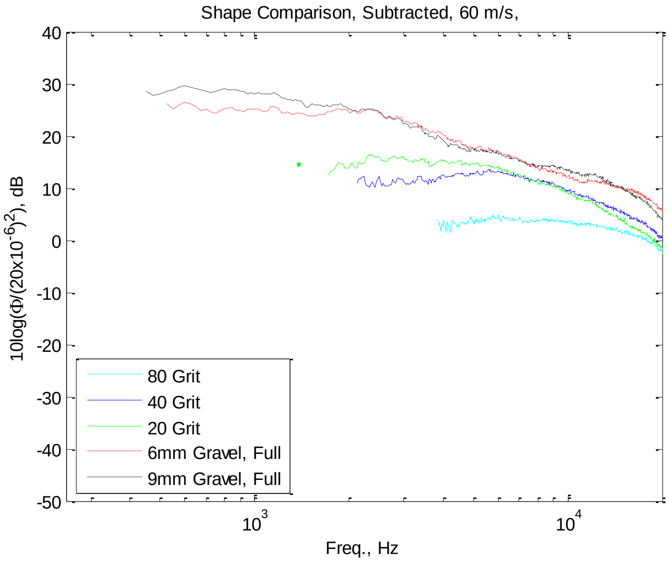

Figure 3-22 - Far field subtracted comparison of 20, 40, and 80 grit sandpaper fetches vs the full fetches of 6 and 9mm gravel

In Figure 3-22, a more direct comparison of both levels and shape can be made. The fetch sizes are both 305x607mm and as the grit size gets lower (i.e. larger element sizes on the sandpaper), it approaches the full layouts of both the 6 and 9mm gravel. When progressing from 80 to 40 to 20grit sandpaper, the increase of SPL with increasing frequency becomes less apparent. While the 20grit sandpaper does increase between 2 and 3kHz slightly, the trend of a smaller increase is present and can be seen to continue into the 6 and 9mm full fetches. Looking back at Sections 3.3.1 and 3.3.2, there was discussion of the slight hump seen in the full fetch layouts. This hump is likely to be cause by the same type of flow and rock interaction as that producing the high frequency increase of the sandpaper roughness. The average particle size of the 80, 40, and 20grit sandpapers are 0.2mm, 0.425mm, and 1mm, respectively. The 6 and 9mm roughness fetches can therefore be thought of as even lower numbered grit sizes.

This gives the most convincing proof that the grid arrays show little to no interaction, while the full fetches do. They act much like the sandpaper roughnesses of Alexander (2009).

3.4 Glegg *et al.* (2007) Normalization

3.4.1 *Formulation*

Glegg *et al.* (2007) introduces a method by which a scattering element increases the shear stress at the wall, thereby changing the unsteady forces on the roughness elements. He assumes that vortex shedding of an individual element will determine the drag on that element, and will radiate as follows.

$$\Phi_{pp}(\vec{x},\omega) = \left(\frac{k\cos(\theta_n)}{4\pi|\overrightarrow{y_n} - \vec{x}|}\right)^2 \Phi_{FF_n}(\omega)$$

Equation 16 – Sound radiated by vortex shedding

Here k is the acoustic wavenumber, $\overrightarrow{y_n}$ is the element position, $\vec{x}$ is the observer position, and θ_n is the angle between the element and observer measured from the axis of the dipole. For an observer located directly upstream, the function $\Phi_{FF_n}(\omega)$ is the unsteady drag spectrum of the individual element calculated as the mean square drag per angular frequency.

As was previously assumed, each individual element has no interaction with any of the other elements. This allows for a summation of Equation 16 to describe a roughness fetch of any arbitrary number of elements.

$$\Phi_{pp}(\vec{x},\omega) = \sum_{n=1}^{N}\left(\frac{k\cos(\theta_n)}{4\pi|\overrightarrow{y_n} - \vec{x}|}\right)^2 \Phi_{FF_n}(\omega)$$

Equation 17 – Radiated sound by multiple individual elements

By normalizing $\Phi_{FF_n}(\omega)$, the unsteady drag spectrum, by the steady drag on each element, D_n, and by introducing the friction frequency defined in Glegg *et al.* (2007), $\omega_\tau = \frac{U_n}{d_n}$, where d_n is the element size and U_n characterizes the mean velocity it experiences, one is left with the non dimensional drag spectrum, $W_{FF}\left(\frac{\omega}{\omega_{\tau n}}\right)$.

$$\frac{\Phi_{FF_n}(\omega)\omega_{\tau_n}}{D_n^2} = W_{FF}\left(\frac{\omega}{\omega_{\tau_n}}\right)$$

Equation 18 – Unsteady drag spectrum

Using this result in Equation 18 and rearranging,

$$\Phi_{pp}(\vec{x},\omega) = \left(\frac{k}{4\pi}\right)^2 \sum_{n=1}^{N} \left(\frac{\cos(\theta_n)}{|\overrightarrow{y_n} - \vec{x}|}\right)^2 W_{FF_n}(D_n^2/\omega_{\tau_n})$$

Equation 19 – Radiated sound of multiple individual elements incorporating the unsteady drag spectrum

Further, assuming that the non dimensional drag spectrum and the friction frequency remain fairly consistent over the area of the fetch,

$$\Phi_{pp}(\vec{x},\omega) = \left(\frac{1}{4\pi c_o}\right)^2 \left(\Omega_\tau^2\omega_\tau\right) W_{FF}(\Omega_\tau) \sum_{n=1}^{N} \left(\frac{\cos(\theta_n)}{|\overrightarrow{y_n} - \vec{x}|}\right)^2 D_n^2$$

Equation 20 – Radiated sound of multiple individual elements incorporating the unsteady drag spectrum

Where Ω_τ is defined as ω/ω_{τ_n}. Glegg *et al.* (1987) assumed an equation for the drag spectrum of a bluff body in a uniform flow. It will be used as a comparison on the normalized plots.

$$W_{FF}(\Omega_\tau) = \left\{\frac{125\left(\frac{5\Omega_\tau}{2\pi}\right)^2}{\left(\frac{1}{4} + \left(\frac{5\Omega_\tau}{2\pi}\right)^2\right)^{\frac{5}{2}}}\right\} * 8.6 * 10^{-7}$$

Equation 21 – Drag spectrum of a bluff body in uniform flow

At this point, Equation 20 can be further rewritten to include $\frac{1}{2}\rho U_n^2 S C_D$ in place of D_n to get around the estimation of the mean steady drag on each element. S, the frontal area of the elements, is needed. For the cubic elements, this is simply 9mm^2. For the gravel elements, the frontal area can be approximated as a circle with the roughness height being the diameter. Introducing this change, Equation 20 can be further manipulated to show

$$C_D^2 W_{FF} = (4\pi c_o)^2 \Phi_{pp} / \left(\Omega_\tau^2 \omega_\tau\right) \sum_{n=1}^{N} \left[\left(\frac{\cos(\theta_n)}{|\overrightarrow{y_n} - \vec{x}|}\right)^2 \left(\frac{1}{2}\rho U_n^2 S\right)^2\right]$$

Equation 22 – Final normalization equation

Using this normalization technique, the results of the 6 and 9mm gravel elements as well as the 3mm cubic and hemispherical element array build ups will be normalized and plotted. The position $\overrightarrow{y_n}$ was taken for each element in the fetch for the grid arrays, and U_n was taken as the maximum edge velocity at a location three rows into the full array to simplify the equations while still giving good results. All of the figures shown are plotted on a semi logarithmic scale, with non dimensionalized frequency $\Omega_\tau = \frac{\omega}{\omega_{\tau_n}}$ on the horizontal axis and non dimensional drag spectra $C_D^2 W_{FF}$ on the vertical axis, from -100 to 0. Also plotted on each figure is the estimated spectrum model for bluff bodies by Glegg *et al.* (1987). This estimate was consistently lower than the normalized spectrum for all of the roughness elements, so a dB addition was made to better show the spectrum shape against the normalized data.

3.4.2 ***6mm Gravel Roughness***

Referring to Figure 3-9, the data can be seen to be spread over a 12dB range between the lowest audible fetch and the largest, 11x21, fetch. There is an even larger gap of 20dB between the lowest audible fetch and the full coverage layout. By applying the normalization Equation 3.11, the following collapse is shown in Figure 3-23.

The most glaring feature of the normalized plots is the collapse of the deterministic roughness layouts. These were originally separated by ~12dB in the subtracted data, and are now separated by <2dB over the whole non dimensional frequency range for all speeds. The normalized data fits the estimated drag spectral shape better with increasing speed. The consistency of the collapse in the grid layouts shows that each element is acting with little to no interference due to the surrounding elements, at least acoustically. This is not the case with the full fetch, as it shows a 10dB decrease in the normalized data. The elements in the full fetch are spaced much closer together and each acts to shadow the downstream elements much more than with the larger grid spacing layouts. This shielding would hide the downstream rocks from the higher velocity, thereby decreasing the drag on each element, resulting in less noise produced per element.

It is apparent that as speed increases from Figure 3-23 (a) at 20m/s to that of Figure 3-23 (e) at 60m/s, the model proposed by Glegg becomes better at predicting the spectral shape of the data. At lower velocities, the measured and normalized sound levels begin to decay much faster than that shown by the model. Glegg's model assumes individual bluff body elements, and the normalization was based on a single velocity near the front of the fetch. It could be that, with the velocity decay as one moves downstream on the plate, the theory is over predicting the drag that will be present on each element, resulting in a more high frequency noise being estimated. However, at 60m/s as seen in Figure 3-23 (e), the data and theory remain closely collapsed to each other, within 5dB.

3.4.3 ***9mm Gravel Roughness***

The same normalization based on non dimensional drag spectra was done for the 9mm gravel arrays and is shown in Figure 3-24.

Again, the normalized drag spectra collapse, within 3dB. There are noticeable oscillations in the smaller sized layouts, such as the 2x3, but this is due to incomplete scalloping correction and is not a real phenomenon. It is impressive that even these larger, 9mm roughness elements do not interact, even weakly, at any of the velocities. Again, the estimated drag spectra fits the shape of the higher velocities well, but is not as steep as the roll off seen in the 20 and 30 m/s data, effectively over estimating the drag present on each element. This can be attributed to the shape of the elements. The drag estimate assumes a bluff body and consistent velocity over the fetch, but many of the rocks have curvature to them that make the drag less than would be expected on a flat faced element and are impinged by a lower velocity than assumed by the model.

The normalized full fetch is lower than the other spectra by 5-10dB for all cases. These elements seem to shield each other, but not as effectively as the 6mm elements which had a consistent 10dB drop in the full fetch. With the larger elements, they were not able to be packed as closely, allowing for a slightly more sparse element density. The flow was able to impinge on more of the roughness elements with higher velocity, resulting in more drag and therefore more produced noise spectra per element.

3.4.4 ***3mm Cubic Roughness***

The same normalization based on non dimensional drag spectra was done for the 3mm cubic arrays, which originally showed a 15dB range in the subtracted data.

The cubic roughness elements collapse is most impressive, and is shown in Figure 3-25 (a-e). At all speeds and layouts, the data collapse to within 3dB, implying very weak to no interaction between elements. The estimated drag spectra was again boosted by 25dB. Even though they are 3 times smaller than the gravel, the sharp corners and blunt face of the 3mm cubes account for a higher drag per element, and is more representative of the bluff body assumption. This is shown by how well the shape of the non dimensional drag spectra fits the measured data at all speeds, something that was not as prevalent in the gravel data. Where there was a 20+dB difference between the theory and the normalized 9mm gravel, in the cubic data this is decreased to a maximum of a 15dB discrepancy. The spectral shape of the 50 and 60m/s normalized data, shown in Figure 3-35 (d) and (e), aligns with theory very well.

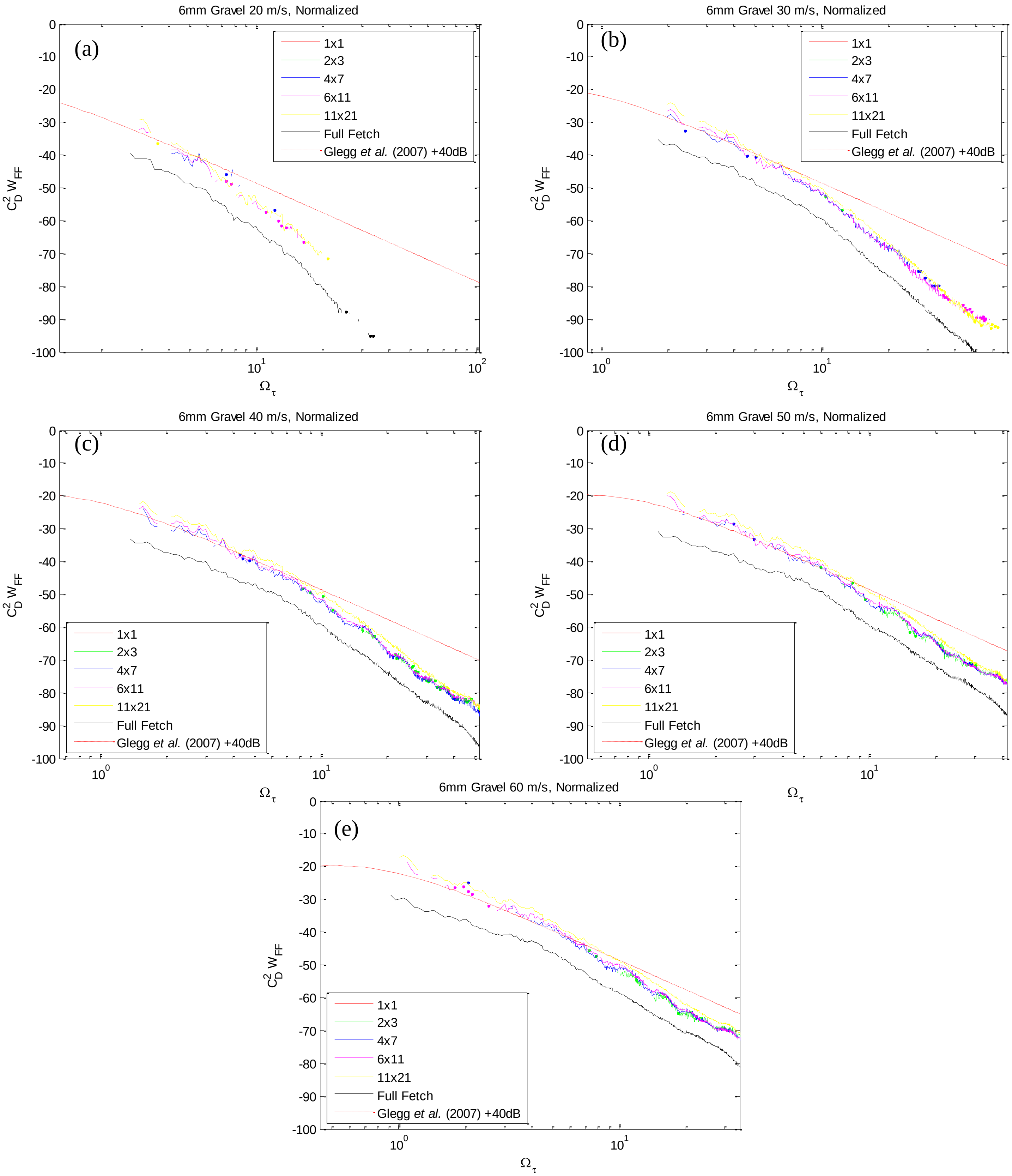

Figure 3-23 (a-e) - Normalized drag spectra of 6mm gravel arrays with listed dB adjustments

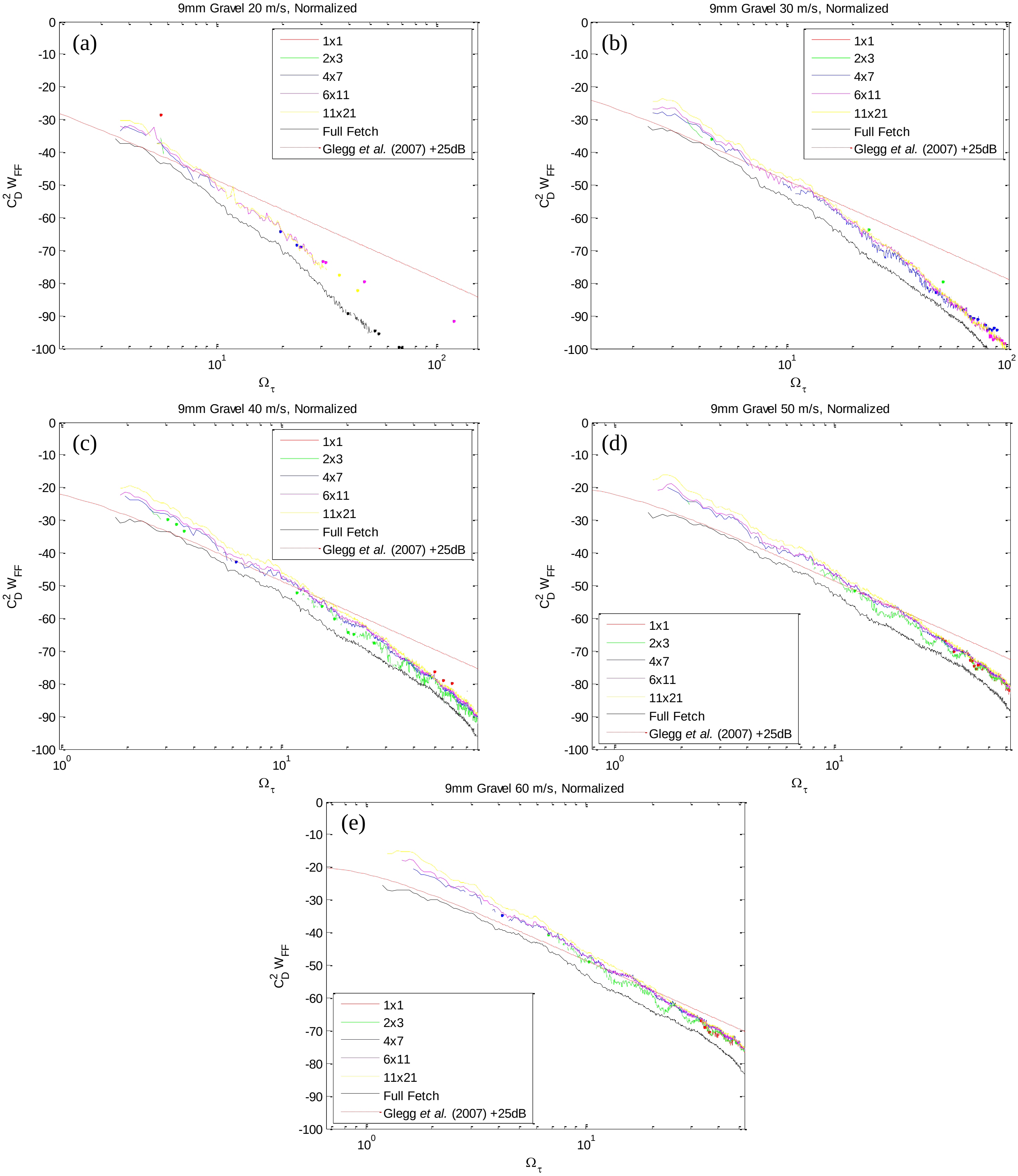

Figure 3-24 (a-e) - Normalized drag spectra of 9mm gravel arrays with listed dB adjustments

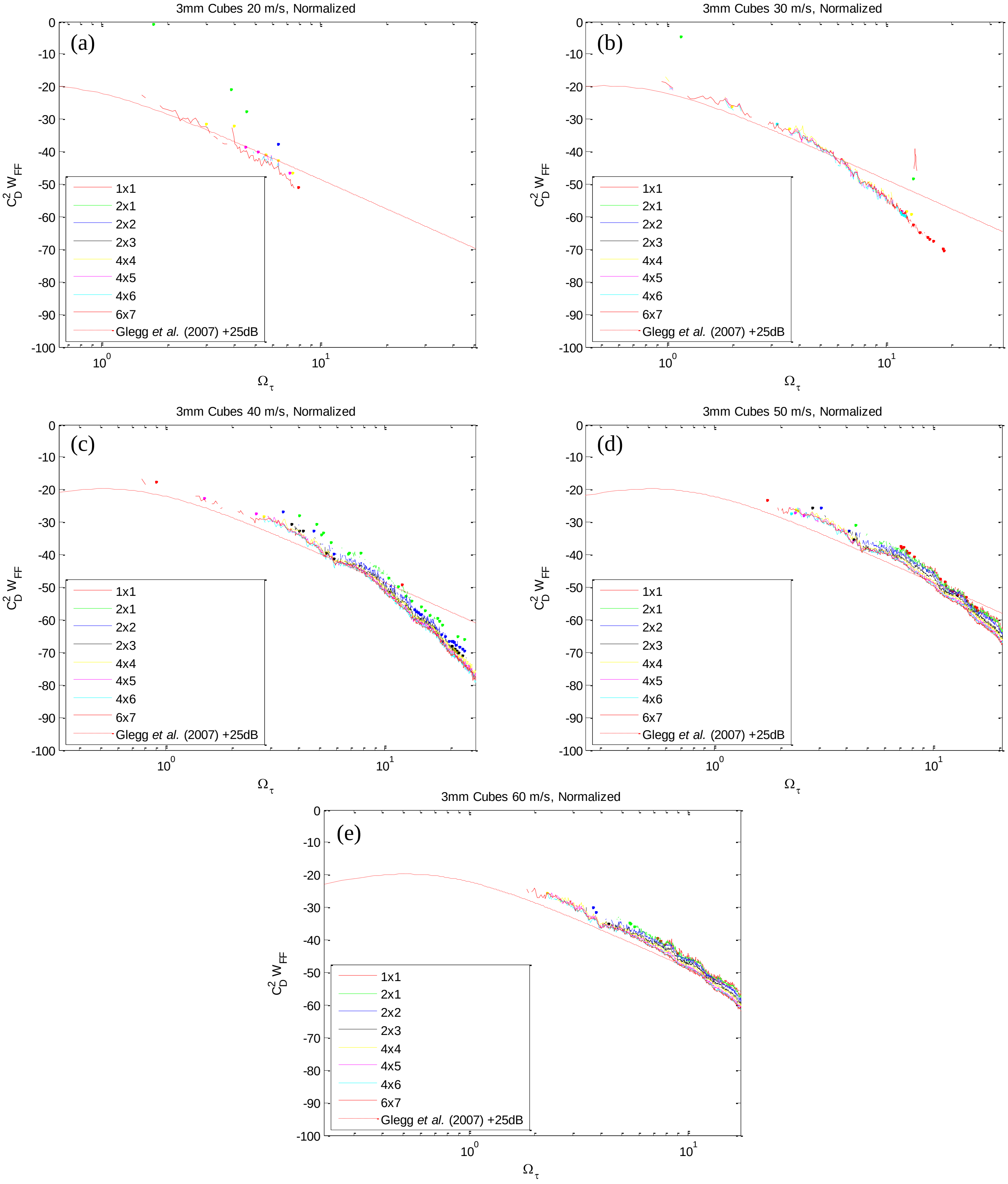

Figure 3-25(a-e) - Normalized drag spectra of 3mm cubic arrays with listed dB adjustments

3.4.5 *3mm Hemispherical Roughness*

Only one layout, the 6x7 element array, was available for the 3mm hemispherical roughness. The subtracted data showed a spread of approximately 15dB between the 40 and 60m/s data. Once normalized, the data collapses to within 5dB, as shown in Figure 3-26. Glegg's model was boosted by 25dB, again to show the true spectral shape against the estimated model. The most glaring result of this normalization is the poor representation of the spectral shape. At 60m/s, where the other types of element arrays were consistently showing agreement with the model, the hemispherical roughness does not match in slope well at all. The bluff body assumption for the model does not fit well with the hemispheres. The hemisphere layout was, by far, the smoothest with the least amount of each element perpendicular to the flow. The flow was able to spill around the edges of the smooth hemispheres without impinging on the faces, resulting in a strong variance from the model.

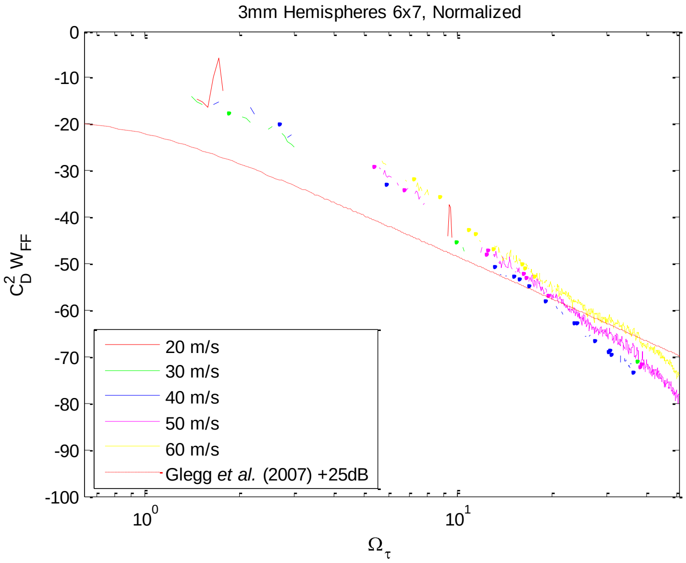

Figure 3-26 - Normalized drag spectra of 3mm hemisphere array with listed dB adjustments

3.4.6 *Unsteady Drag Percentage of Mean Drag*

For the normalized data at 60m/s, there is ample data for the largest layouts to integrate the spectrum to yield an estimation of the RMS drag coefficient on each element.

Roughness Type	Unsteady Drag Percentage of Mean Drag
3mm Cubes (6x7)	5.96
3mm Hemispheres (6x7)	1.86
6mm Gravel (11x21)	9.62
9mm Gravel (11x21)	16.34
6mm Gravel (Full)	2.87
9mm Gravel (Full)	5.09

Table 3-11 - RMS of unsteady drag for each of the element roughness types and layouts at 60m/s

Table 3-11 shows the RMS percentage and will give an insight into how much of the mean drag is unsteady. The assumed drag coefficient for each element was $C_D = 1$. Note that it may be possible to make specific estimates of the mean drag on the roughness elements using a heuristic method of the type presented by Schlichting (1979). However, this is not attempted here.

3.4.7 *Effect of Speed on Collapse*

Thus far, the normalization discussions have focused on how all the layouts collapse at a given speed. There is also conversation to be made about how an individual layout collapses on itself over the full range of velocities. Shown in Figure 3-27 (a-d) are the 6 and 9mm 11x21 element layouts, along with the 3mm cubic and hemispherical 6x7 element layouts across all five nozzle exit velocities.

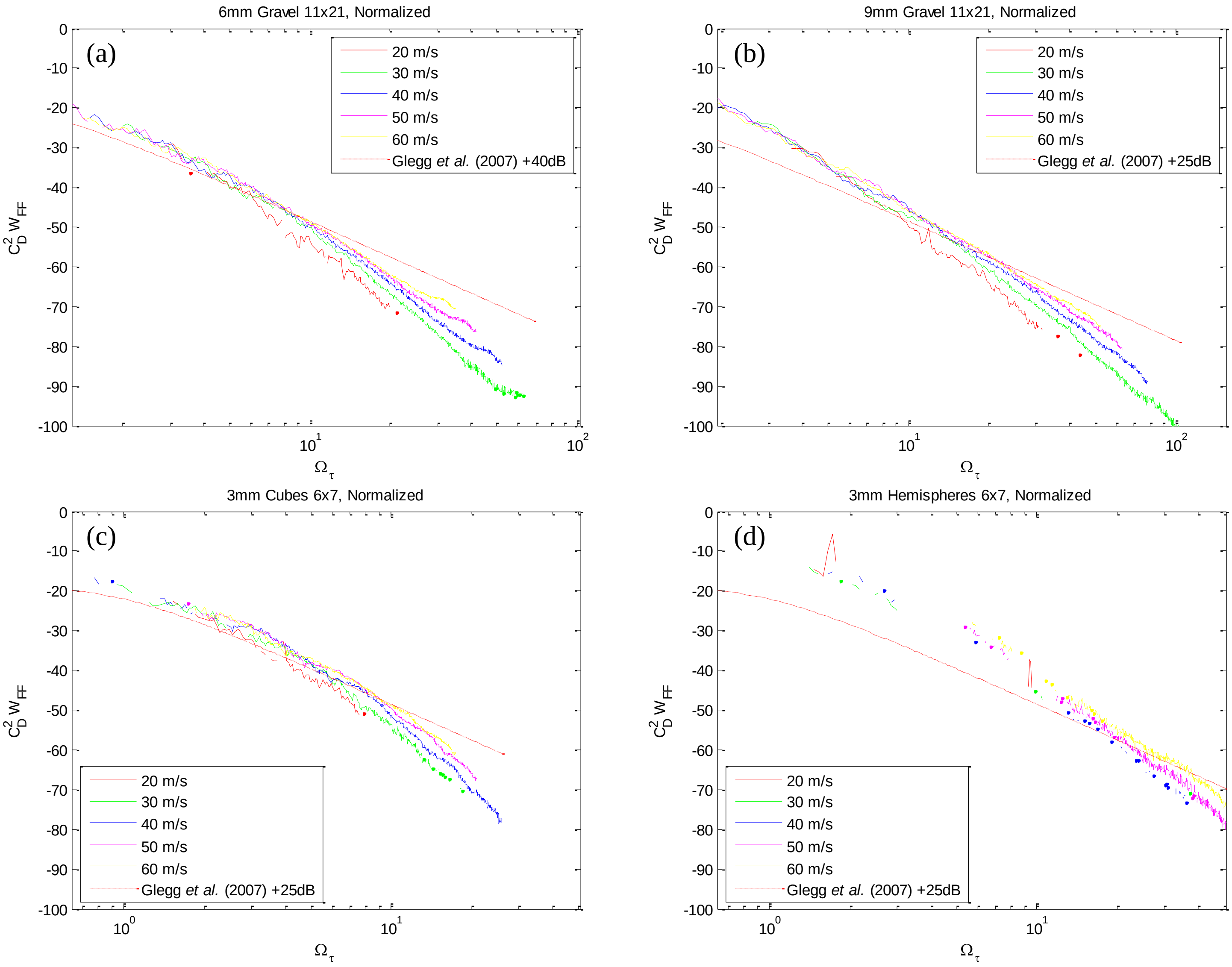

Figure 3-27 (a-d) – Normalized drag spectra of 11x21 element arrays of 6 and 9mm gravel and 6x7 element arrays of 3mm cubes and hemispheres

The most prevalent trend in the normalized data is that for all different element types, as the speed is increased, the normalized data becomes closer in shape to Glegg's model. Another visible trend in Figure 3-27(a), (b), and (c) is that at the lower frequencies, the data collapses to a 3dB range. Not enough information is available for (d), the 6x7 hemisphere layout. As frequency increases, the data becomes less collapsed, but remains much closer than the unnormalized data of previous sections. The 6mm gravel in the 11x21 element layout originally had a 40dB spread, and is now within 10dB across all nondimensional frequencies. For the 9mm gravel, the data collapsed from almost 50dB to less than 10dB again. The collapse of the 3mm cubes was again impressive, from an original 40dB range to again within 10dB.

While the collapses are notable from the unsubtracted data, there is still work to be done to further collapse this data by modifying Glegg's model to include the empirical data shown in the previous sections.

3.4.8 *Effect of Shape on Collapse*

To this point, the normalized data has been shown only for similar roughness types. As was shown in Sections 3.3.4 and 3.3.6, the shape of the elements has an effect on the spectral levels at the same velocity. Figure 3-28 and Figure 3-28 show the subtracted and normalized data for the 6x7 element layouts of the 3mm cubes and hemispheres, along with the 11x21 element layouts of 6 and 9mm gravel for 60m/s.

Figure 3-29 shows that, even with the large discrepancy in the number, size, and shape of the elements, the data is collapsed to within 8dB from the original 20dB. The slope of all the data is shown to be parallel. In looking closer at the normalized data, it is seen that the 3mm cubes and 6mm gravel lay practically on top of each other. Also, the 3mm hemisphere and 9mm gravel are within 3dB. The data set excluding the 3mm hemispheres will all lie within a 5dB range, and this may be the most compelling argument for Glegg's basic model which assumes bluff bodies. It has been mentioned previously that the 3mm hemispheres are the least like a bluff body, with little to no perpendicular face to the flow, while the cubes are the most like a bluff body with the gravel falling somewhere in the middle. Such a great collapse between elements of such different shapes, sizes, and number in the layouts definitely warrants an argument to the applicability of this model.

However, the spectral model levels, which were increased objectively in order to best fit the data, line up one on top of the other. It must be reiterated that each of these spectral fits were placed independently of each other to best fit the data that they were to represent. Once they are all plotted together, they show a fit on each other that is remarkable. They were made with 3, 6, and 9mm roughness heights, accordingly, in the equations, along with different edge velocities for the 6x7 and 11x21 element layouts. Even with the differences, they still show a great collapse.

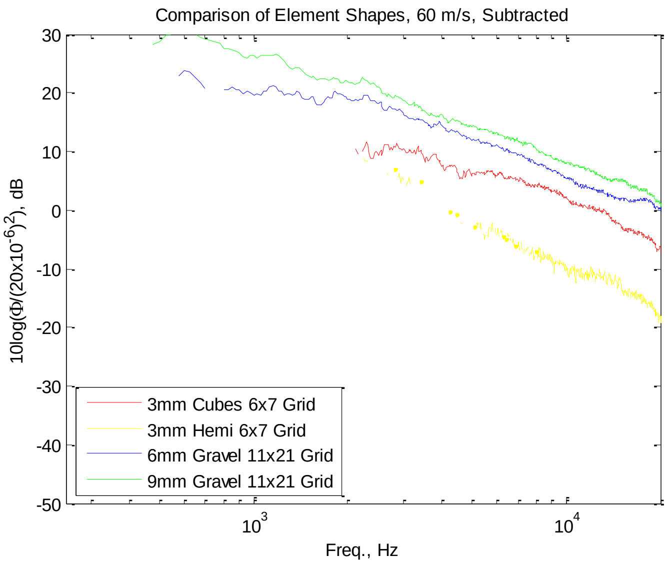

Figure 3-28 - Subtracted spectra of 6x7 element layouts of 3mm cubes and hemispheres along and 11x21 element layouts of 6 and 9mm gravel.

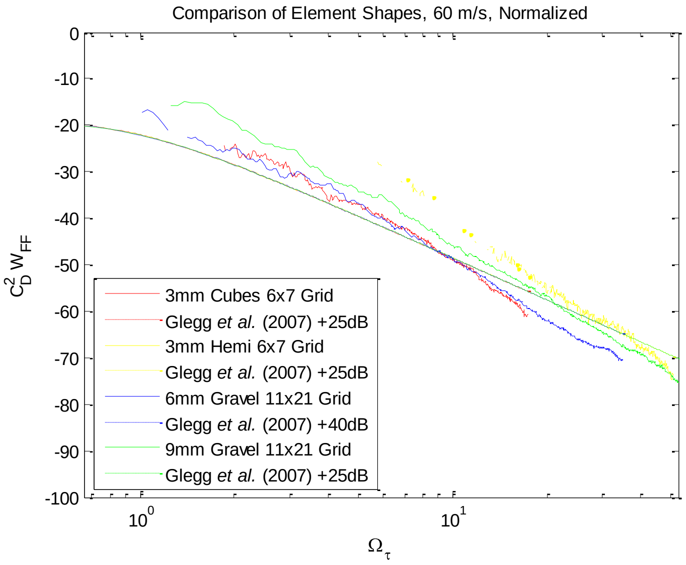

Figure 3-29 – Normalized drag spectra of 6x7 element layouts of 3mm cubes and hemispheres along and 11x21 element layouts of 6 and 9mm gravel.

3.4.9 *Modification of Glegg et al. (1987) Model*

Glegg *et al.* (1987)'s assumed model equation for the drag spectrum of a bluff body in a uniform flow, as shown below for reference in Equation 23, fits the data well at high speeds, but it over predicts much of the high frequency data of the lower velocities. The model assumed inviscid flow, however viscous effects become increasing important as the edge velocity is decreased. A modification of this model is needed to better fit the empirical data presented in this thesis.

$$W_{FF}(\Omega_\tau) = \left\{ \frac{125\left(\frac{5\Omega_\tau}{2\pi}\right)^2}{\left(\frac{1}{4}+\left(\frac{5\Omega_\tau}{2\pi}\right)^2\right)^{\frac{5}{2}}} \right\}\text{(d)} * 8.6 * 10^{-7}$$

Equation 23 – Drag spectrum of a bluff body in uniform flow (As shown in Equation 18)

Note first that with a small value of Ω_τ, which can be rewritten as $\frac{\omega d_n}{U_n}$, the ¼ leading term in the denominator dominates. As Ω_τ increases with increasing frequency, the second term in the denominator rapidly becomes of greater value. Their interaction describes the position of the peak of the unsteady drag spectrum, such as that of Figure 3-25 (e) at the nondimensional frequency $\Omega_\tau \cong 0.5$. The increase in the value of the $\frac{5\Omega_\tau}{2\pi}$ term, along with the same term in the numerator, results in a slope of the drag spectrum asymptotically approaching -3 at high frequencies. The high velocity data exhibits this behavior; however the lower velocities consistently show a rapid roll off at nondimensional frequencies above $\Omega_\tau = 10$. This roll off can be better described by modifying the exponent on denominator, as allowed by the n of Equation 24, thereby changing the slope to empirically match the data. The leading term of 125x8.6x10^{-7} can be altered to best fit the levels of the data, as shown by A of Equation 24. Therefore, the data will no longer need to be boosted. The resulting equation for manipulation is shown in Equation 24, along with **Error! Reference source not found.** showing the results of changing A and n.

$$W_{FF}(\Omega_\tau) = A\left\{ \frac{\left(\frac{5\Omega_\tau}{2\pi}\right)^2}{\left(\frac{1}{4}+\left(\frac{5\Omega_\tau}{2\pi}\right)^2\right)^{n}} \right\}$$

Equation 24 – Drag spectrum of a bluff body in uniform flow allowing for modification

From **Error! Reference source not found.**, it is shown to be relatively simple to djust the model shown in Equation 18 and Equation 23 to best fit the data. Figure 3-30 will show the modified best fit for Figure 3-29, which was the largest grid type layout for each roughness type at 60m/s nozzle exit velocity, followed by Figure 3-32 (a-d) showing the modified best fit for each type of roughness individually. Table 3-12 shows the values of A and n used in each. As mentioned previously, the roll off of the lower velocities can be attributed to a Reynolds number effect not taken into account in this model. Therefore, the best fit for this model will be on the 60m/s data, with future work possible in matching the lower speeds. The lower velocity data will be shown, but note that the fit will not be as accurate at high frequencies for this data.

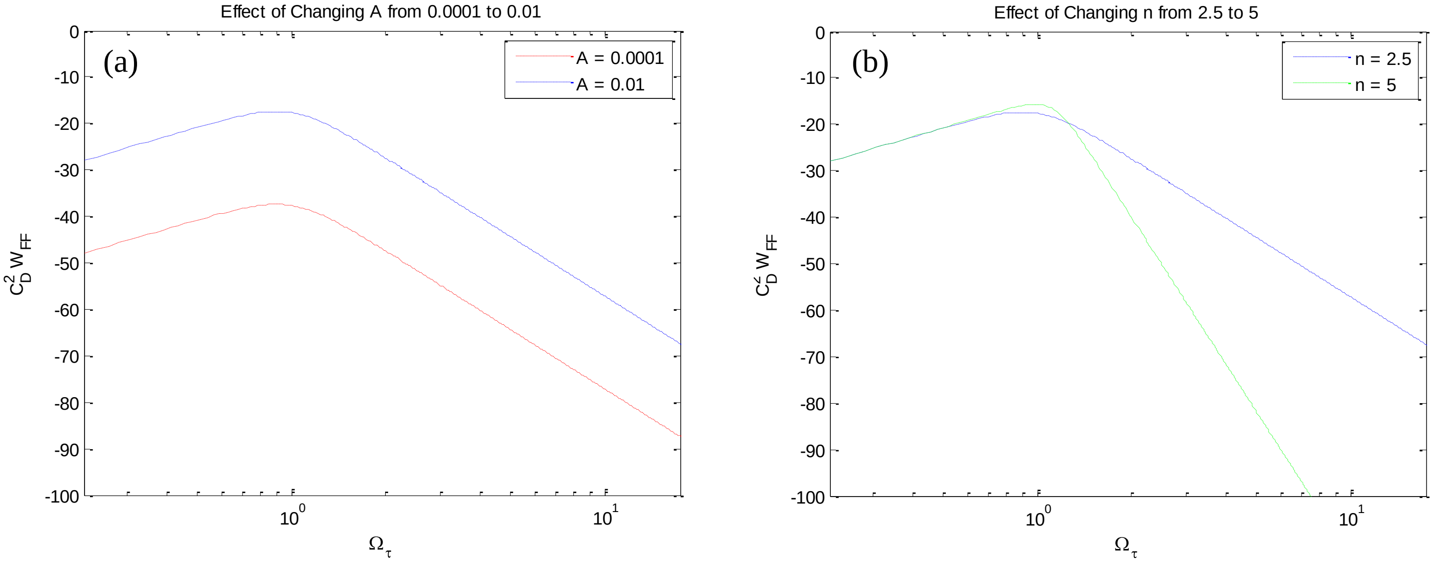

Figure 3-31 (a and b)– Effects of modifying A and n in the Glegg *et al.* (1987) drag spectra model

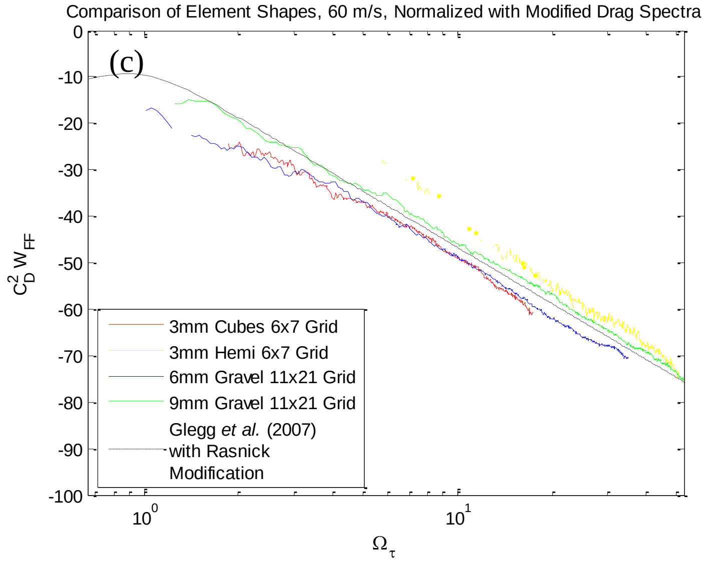

Figure 3-30 (a-c) - Normalized roughness noise of 6x7 element layouts of 3mm cubes and hemispheres along and 11x21 element layouts of 6 and 9mm gravel with modified drag spectrum to best fit data

As was mentioned previous in the discussion of Figure 3-29, the normalized data is parallel and collapsed to within 8dB. The original slope of the drag spectra was too flat, resulting in inaccuracies at both the low and high frequencies, along with a level that was 40dB too low. The new slope and level is shown to best match all the data, being with 4dB at all non dimensional frequencies above 10. Next will be shown all the roughness types individually at 60m/s with the modified drag spectrum for each.

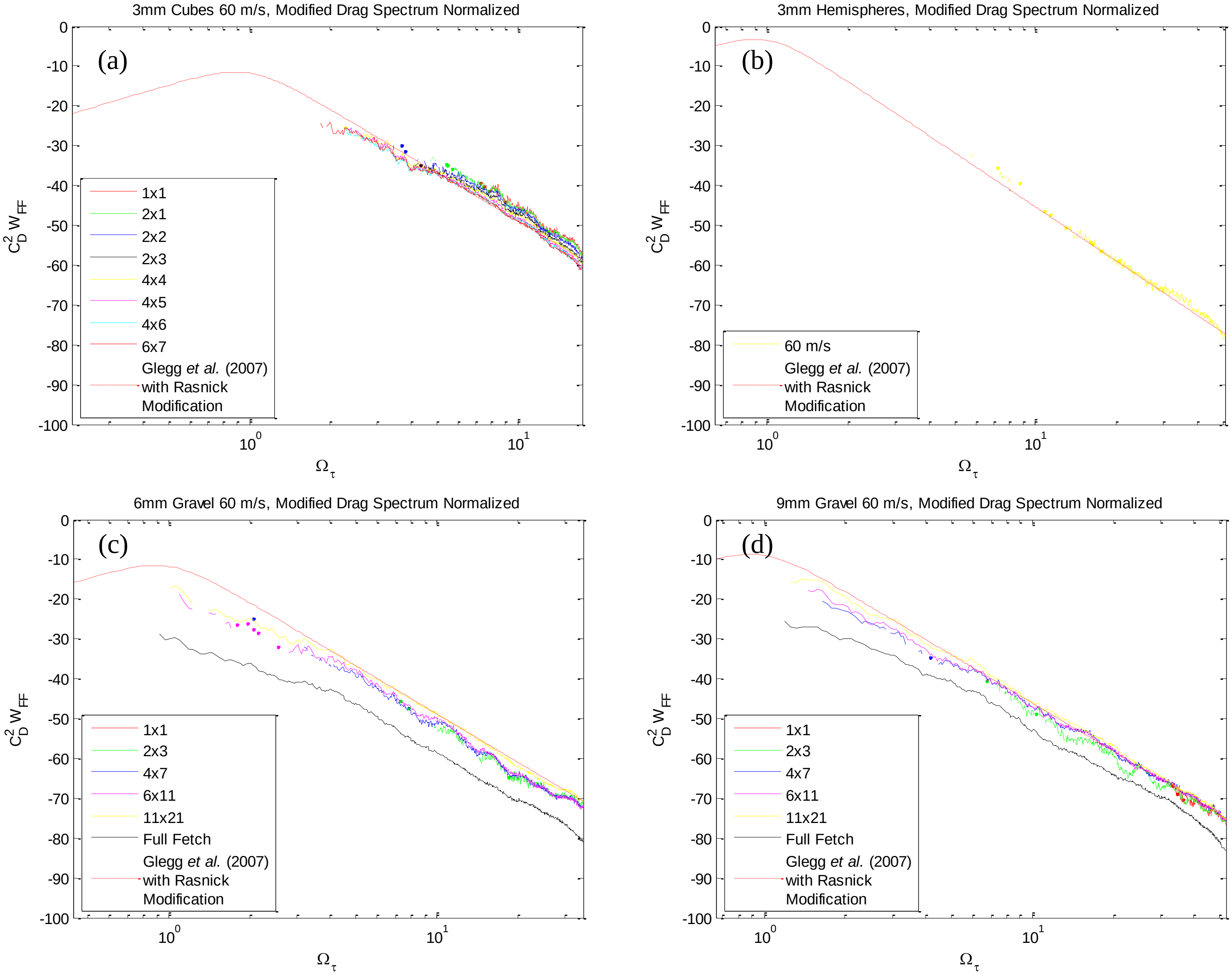

Figure 3-32 (a-d) – Normalized roughness noise for the 3mm cubes, 3mm hemispheres, 6mm and 9mm gravel showing the modified drag spectra

Compared with Figure 3-23(e), Figure 3-24(e), Figure 3-25(e), and Figure 3-26, the slope of the line matches the entirety of the data much better. All previous figures exhibited the shape of the drag spectra as rolling off too slow as compared to the data. The increased n exponent fixes this problem, allowing all of the data up to high frequencies to be well represented by the theory. Table 3-12 further explains the modifications.

Case	A	n
Glegg et al. (1987)	1.08E-04	2.5
3mm Cubes	0.04	3
3mm Hemispheres	0.25	3.25
6mm Gravel	0.04	3
9mm Gravel	0.075	3
All Roughness	0.065	3

Table 3-12 - Modification factors to Glegg *et al.* (1987)

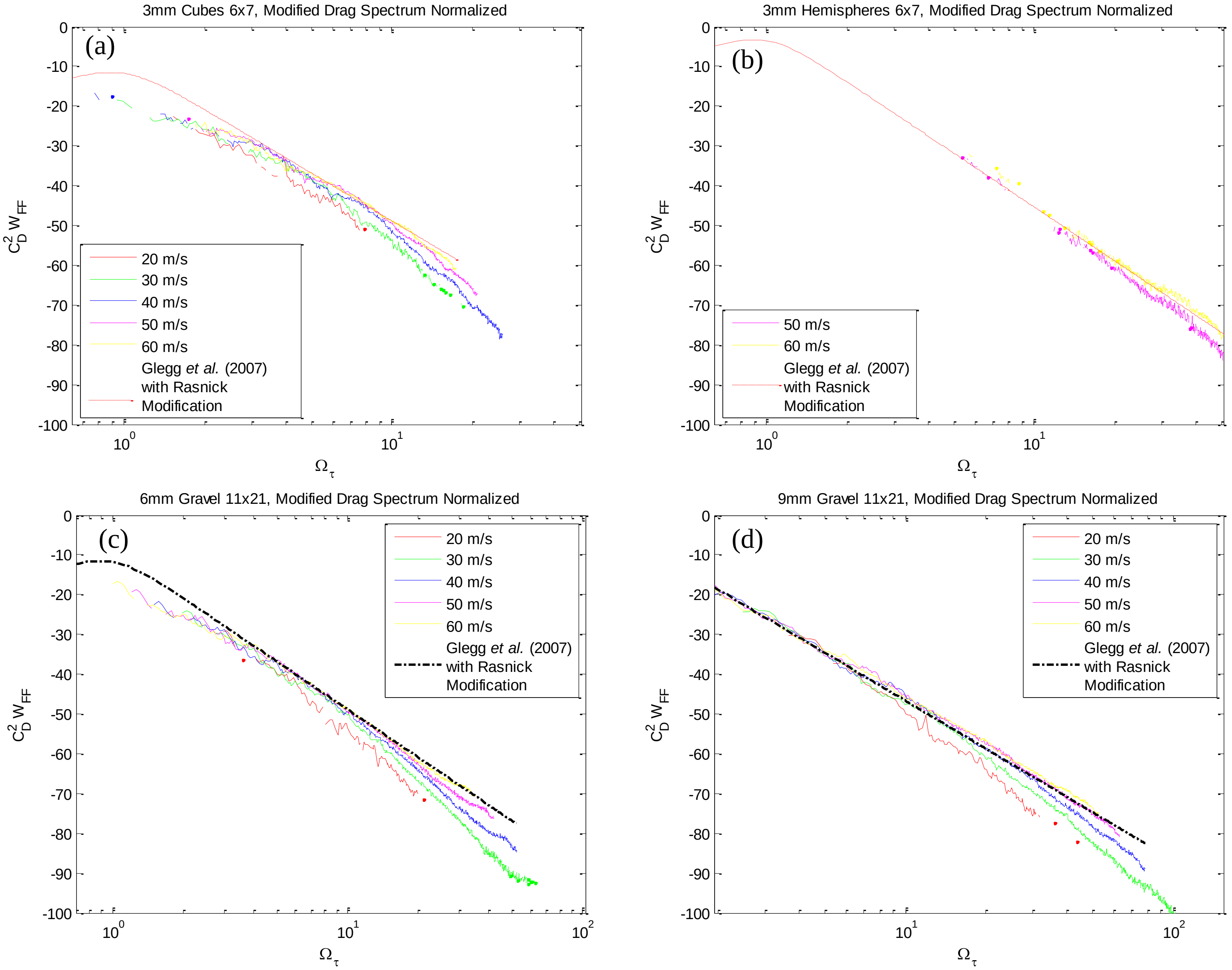

Figure 3-33 (a-d) - Normalized drag spectra of 11x21 element arrays of 6 and 9mm gravel and 6x7 element arrays of 3mm cubes and hemispheres showing the modified drag spectrum

The multiplier, A, had to be greatly increased to represent the actual levels seen in the data. Before, this was achieved by a boost in the dB levels. Of more concern is the change in the exponent n. This value needed only minor modifications to greatly improve the fit with the data. Increasing the exponent from 2.5 to 3 in most cases showed vast improvement. The only outlier was the hemispherical case, where the exponent was increased to 3.25, exhibiting the differences in the slope of hemispherical normalized data to that of the other element types.

Figure 3-33 (a-d) shows the modified drag spectrum for each roughness type that was found for the 60m/s case against the largest grid layout of said element type at all speeds. In all cases, the modified drag spectra over predicts at high frequencies for the lower velocities. However, in the middle range of frequencies, there is good agreement between the theoretical slope and the normalized slope of the data. At higher frequencies, viscous effects become more important and are not accounted for in the model. Again, future work in this area would be to modify the model further to include these Reynolds number effects.

4 Conclusion

Using the Virginia Tech Anechoic Wall Jet Facility, roughness noise was measured in the far field for various stochastic and deterministic roughnesses, using multiple layouts of 3mm cubic elements, 6 and 9mm gravel elements, and a single layout of 3mm hemispherical elements. Overall tunnel and measurement improvements were made during the testing, resulting in a new microphone traverse capable of offering repeatable microphone positioning and ability to be placed in many configurations not possible before. Also, new microphone mounts were made that were acoustically transparent, eliminating the scalloping problem seen in earlier measurements.

- Analysis of far field sound for the deterministic array and stochastic surfaces
    - Roughness noise increases with increasing speed and array size in all cases, and that this roughness noise scales on U^6-U^7.
    - Measureable roughness noise, more than 1 dB above background levels, have been measured for single elements as small as 3mm in height, a mere 1/7th of the boundary layer thickness.
    - There is no interaction between the grid type arrays. Elements as large as 9mm with a spacing of 28mm center to center are shown to act as individual roughness elements. These grid type arrays will not have a homogeneous wall pressure spectrum.
    - There is an interaction between elements in the full fetches. This concludes that the full fetches can be assumed to have a more uniform wall pressure spectrum than the grid arrays.
    - Elements with sharp edges, such as those of the cube, result in a 15dB increase in roughness noise over similarly sized hemispherical roughness elements.
- Normalizations
    - Far field roughness noise was normalized based on the technique theorized by Glegg *et al.* (2007), showing that a scattering element increases the shear stress at the wall changing the unsteady drag forces on the roughness elements.
    - Arrays of 1 to 231 elements of 6 and 9mm gravel, and of 1 to 42 elements of 3mm cubes at a spacing as small as 3 diameters center to center produce sound that collapse to a single curve, implying the same non dimensional drag spectrum.
    - The application of Glegg *et al.* (2007)'s theory shows that the roughness noise produced by the elements is dipole in nature, and can be used to predict the unsteady drag spectral shape.
    - Glegg *et al.* (2007) unsteady drag spectrum under predicts the normalized data by 25-40dB, though there is good agreement in the shape. The shape of the theory shows a less rapid roll off at high frequencies due to a Reynolds number effect.

- Empirical modifications to Glegg *et al.* (1987)’s model were shown to fit the data, producing a new model for use with gravel and spherical type elements, a model for cubic elements, and a model for hemispherical elements.

References

Alexander, W. N., 2009, "Normalization of Roughness Noise on the Near-Field Wall Pressure Spectrum", MS Thesis, Aerospace and Ocean Engineering Dept., Virginia Tech, Blacksburg, VA.

Alexander, W. N., Rasnick, M. R., Catlett, M. R., Devenport, W. J., and Glegg, S., 2009, "Boundary Layer Noise from Discrete Roughness Elements", 15th AIAA/CEAS Aeroacoustics Conference, Miami, FL, May 11-13, 2009, AIAA-2009-3310.

Chanaud, R. C., 1969, "Experimental Study of Aerodynamic Sound from a Rotating Disk", Journal of the Acoustical Society of America, Vol. 45, pp. 392-397

Cole , L. D., 1980, "Measurements of Sound Generated by Boundary Layer Turbulence Over Smooth and Rough Surfaces", DTNSRDC Report SAD-288E-1942.

Curle, N., 1955, "The Influence of Solid Boundaries Upon Aerodynamic Sound", Proc. R. Soc., London, Vol. A231, pp. 505-514.

Farabee, T. M., and Geib, F. E., 1991, "Measurements of Boundary Layer Pressure Fluctuations at Low Wavenumbers on Smooth and Rough Walls", Flow Noise Modeling Measurements and Control, ASME NCA-Vol. 11, pp. 55-68.

Glegg, S., and Devenport, W. J., 2009, "Far-Field Sound from Rough-Wall Boundary Layers", Proc. R. Soc., London, Vol. A465, pp. 1717-1734.

Glegg, S., Devenport, W. J., Grissom, D. L., and Smith, B., 2007, "Rough Wall Boundary Layer Noise: Theoretical Predictions", 13th AIAA/CEAS Aeroacoustics Conference, Rome, Italy, May 21-23, 2007, AIAA-2007-3417.

Grissom, D. L., 2007, "A Study of Sound Generated by a Turbulent Wall Jet Flow Over Rough Surfaces", Ph.D. Dissertation, Aerospace and Ocean Engineering Dept., Virginia Tech, Blacksburg, VA.

Grissom, D., Smith, B., Devenport, W. J., and Glegg, S., 2006, "Rough Wall Boundary Layer Noise", 12th AIAA/CEAS Aeroacoustics Conference, Cambridge, Massachusetts, May 8-10, 2006, AIAA 2006-2409.

Hersh, A. S., 1983, "Surface Roughness Generated Flow Noise", 8th AIAA Aeroacoustics Conference, Atlanta, GA, April 11-13, 1983, AIAA-83-0786.

Howe, M. S., 1979, "The Role of Surface Shear Stress Fluctuations in the Generation of Boundary Layer Noise", Journal of Sound and Vibration, Vol. 65, No. 2, pp. 159-164.

Howe, M. S., 1984, "On the Generation of Sound by Turbulent Boundary Layer Flow Over a Rough Wall", Proc. R. Soc., Vol. A395, pp. 247-263.

Lighthill, M. J., 1952, "On Sound Generated Aerodynamically. Part 1. General Theory", Proc. R. Soc., London, Bol. A211, pp. 564-587.

Liu, Y., Dowling, A., and Shin, H.-C., 2008, "Measurements and Simulation of Surface Roughness to Airframe Noise", AIAA Journal, Vol. 45, No. 4, pp. 855-869.

Liu, Y., and Dowling A., 2007, "Assessment of the Contribution of Surface Roughness Noise using Phased Microphone Arrays", Journal of Sound and Vibration, Vol. 314, pp. 95-112

Schlichting, H., 1979, "Boundary Layer Theory, 7th ed.", New York, NY: McGraw-Hill

Skudrzyk, E., and Haddle, G., 1960, "Noise Production in a Turbulent Boundary Layer by Smooth and Rough Surfaces", Journal of the Acoustical Society of America, Vol. 32, pp. 19-34.

Smith, B. S., 2008, "Wall Jet Boundary Layer Flows Over Smooth and Rough Surfaces", Ph.D. Dissertation, Aerospace and Ocean Engineering Dept., Virginia Tech, Blacksburg, VA.

Smol'yakov, A. V., and Tkachenko, V. M., 1991, "Model of a Field of Pseudosonic Turbulent Wall Pressures and Experimental Data", Soviet Physics Acoustics, Vol. 37, No. 6, pp. 627-631.

Yang, Q., and Wang, M., 2008, "Computation Study of Boundary-Layer Noise Due to Surface Roughness", 14th AIAA/CEAS Aeroacoustics Conference, Vancouver, B. C., May 5-7, 2008, AIAA-2008-2905.